Invisible Threads: How Jet Stream Shifts are Amplifying Clear Air Turbulence in U.S. Aviation (1980 - 2023)

Idamis E. Rodríguez Nazario

Master of Science

(Atmospheric and Oceanic Sciences)

at the

University of Wisconsin-Madison

July 2025

Thesis Declaration and Approval

I, Idamis E. Rodríguez Nazario, declare that this Thesis titled 'Invisible Threads: How Jet Stream Shifts are Amplifying Clear Air Turbulence in U.S. Aviation (1980 - 2023)' and the work presented in it are my own.

Idamis E. Rodríguez Nazario		
Author	Signature	Date

I hereby approve and recommend for acceptance this work in partial fulfillment of the requirements for the degree of Master of Science:

Mayra Oyola-Merced		
Assistant Professor	Signature	Date

Ángel F. Adames Corraliza		
Associate Professor	Signature	Date

Tristan L'Ecuyer		
Professor	Signature	Date

Abstract

Invisible Threads: How Jet Stream Shifts are Amplifying Clear Air Turbulence in U.S. Aviation (1980 - 2023)

by Idamis E. Rodríguez Nazario

Over the last 10 years, there has been a noticeable increase in Clear Air Turbulence (CAT) incidents reported by commercial airlines, including several recent accidents that have resulted in passenger injuries. This trend is alarming, as CAT poses significant risks to aviation safety and comfort due to its unpredictable nature and lack of visual warning for pilots. One possible explanation for this increase is the impact of changing atmospheric conditions, particularly on the jet stream. Atmospheric reanalysis data were used to analyze jet stream changes over a 43-year period, with a specific focus on deviations from climatological norms in the last decade (2014-2023). Operational Pilot Reports (PIREPs) were implemented to validate the robustness of the turbulence analysis. The study focuses on parameters relevant to commercial aviation and major airline routes over CONUS, including wind speed ($|\mathbf{v}|$), vertical wind shear (VWS), omega (ω), specific humidity (q), temperature (T), ertel potential vorticity (PV), among others. An increase in zonal wind speeds within the jet stream was found, contributing to a poleward shift during winter and fall months in recent years. Additionally, increases in vertical wind shear at critical flight levels correspond to regions where CAT is more likely to occur. Moreover, rising mean $|\omega|$ throughout the year indicate more pronounced regions of upward and downward air movement that may interact with the jet stream to produce CAT. Regional

hotspots were identified over the Northeast and Midwest, emphasizing areas of increased aviation risk in recent years. These findings suggest that conditions conducive to CAT are becoming more prevalent, particularly along major airline routes. Thus, CAT can lead to increased fuel consumption and delays as pilots are forced to circumvent affected areas, further impacting the efficiency of flight operations. In general, this study emphasizes the importance of integrating reanalysis and observational data to understand turbulence-relevant parameters from the perspective of changing atmospheric conditions at upper levels.

Sigo caminando en la dirección
Que está diciéndome el corazón
Llevo como brújula mi intuición
Cada vez tengo más clara mi misión
A veces visita la confusión
Pero no falta la motivación
De querer lograrlo

Cada día más fuerte la conexión
Con el que me manda la bendición
Prendo una velita hago una oración
Pido por mi vida y por los que son
Que tenga salud que me cuide dios

- Karol G

Acknowledgements

I would like to begin by thanking God for providing me with the opportunity and the courage to continue my studies outside of Puerto Rico. Thank you to those who prepared my recommendation letter for my graduate school application: Ada Monzón, Victor Chavez Mayta, and Jonathan Muños Barreto. Thank you for believing in me and for mentoring me throughout my undergraduate studies. Thank you to my advisor, Mayra Oyola-Merced, for opening the doors of her research group, for guiding me over the past two years, for her valuable advice, for providing me opportunities in internships and conferences, for being a friend when I needed it, and for showing me the incredible world of aviation. Thank you for always challenging me to go the extra mile. Thank you to my friends, Ally, Shane, and Sofia, for always being there for me during the most challenging moments of graduate school, for the coffee dates, and the moments of laughter. Thanks to my research group, SOARS, Katie, Stefanie, Paige, Niwdé, Molly, Ruby, and Matt, for always supporting and motivating me. Thanks to my GAC committee, Ángel and Tristan, for their time and advice while writing this thesis.

Thanks to my family in Puerto Rico, whose love I feel every day, despite the distance. Thanks to my beautiful mother, Nilsa, for being my best friend, for checking in with me every day to see how I'm doing, and for always being excited about my projects. Thanks to my father, Javier, for always believing in me, and telling me "tu puedes". Thanks to my siblings, Stephanie and Christian, for always being there when I need them the most. Thanks to my boyfriend, Juan Iván, for always believing in me, for supporting me in my projects, for being present in my life every day despite the distance, and for always getting excited about my achievements. Thanks to my grandmothers, Awilda and Mery, for always having my cup of coffee ready when I visited them and did a little work on the side. Thanks to my aunts, Jackie and Taina, for always celebrating my achievements as if they were her own. Thanks to my two grandparents, Mirna and Luis. Their words and experiences will always be with me and I know that if they were here, they would be

incredibly proud of me. Thanks to me for the lonely nights, for the moments of doubt, for the discipline, for never giving up and for choosing to go for what I deserve. Cheers.

Contents

List of Figures

List of Tables

Abbreviations

CAT	**C**lear **A**ir **T**urbulence
CIMSS	**C**ooperative **I**nstitute for **M**eteorological **S**atellite **S**tudies
EDR	**E**ddy **D**issipation **R**ate
FAA	**F**ederal **A**viation **A**dministration
FL	**F**light **L**evel
GTG	**G**raphical **T**urbulence **G**uidance
ICAO	**I**nternational **C**ivil **A**viation **O**rganization
MERRA-2	**M**odern-**E**ra **R**etrospective **A**nalysis for **R**esearch and **A**pplications, Version **2**
MOG	**M**oderate or **G**reater
NOAA	**N**ational **O**ceanic **A**tmospheric **A**dministration
NWP	**N**umerical **W**eather **P**rediction
PIREPs	**P**ilot **REP**orts
PV	**P**otential **V**orticity
TKE	**T**urbulence **K**inetic **E**nergy
UTLS	**U**pper **T**roposphere **L**ower **S**tratosphere
VWS	**V**ertical **W**ind **S**hear

Physical Constants

Turbulence length L = 100 or 200 meters for CAT

Symbols

ω	vertical velocity	Pa $(s)^{-1}$
$\|\mathbf{v}\|$	wind speed	m $(s)^{-1}$
VWS	vertical wind shear	m $(s)^{-1}$ over 1 km
EDR	eddy dissipation rate	m^2/s^3
q	specific humidity	g/kg
T	Temperature	°C
PV	ertel potential vorticity	10^6 m^2 $(kg)^{-1}$ $(s)^{-1}$

Chapter 1

Introduction

1.1 What is Turbulence in Aviation?

In fluid dynamics, turbulence is the irregular air motion resulting from a complex interaction between wind speed ($\mathbf{v}$), density (ρ), distance (L), and viscosity (μ) of a fluid (Sharman (2016)). According to the International Civil Aviation Organization (ICAO), turbulence in aviation is defined as rapid changes in the atmosphere. In the upper troposphere and lower stratosphere (UTLS), these changes in the vertical wind shear (VWS) are most prevalent (ICAO (2023)). These variations can impact aviation safety by causing abrupt changes in an aircraft's airspeed and altitude. In addition, turbulence can be classified by its intensity as light, moderate, severe, and extreme. Generally, turbulence that affects aircraft is generated by various large-scale forcing mechanisms, which

are categorized according to their source: convection, low-level turbulence, and mountain waves, and clear air turbulence (CAT; Sharman (2016)).

1.2 What is Clear Air Turbulence (CAT)?

CAT is a type of turbulence that occurs in clear skies (Ellrod (2003)). It is one of the most challenging types of turbulence to detect because it occurs without visual or radar cues (FAA (1968)), primarily due to VWS. Thus, CAT can be critical for aviation operations because it can happen without visual warnings for pilots (FAA (1968)), making it difficult to detect with conventional radar systems. While aviators provide key information about weather conditions encountered by an aircraft in flight (FAA (2017)), they come with several limitations, which will be discussed in detail in Chapter 2.

Typically, CAT can be found at flight levels (FL) between 20,000 ft (FL200) and 45,000 ft (FL450), within the UTLS where most aircraft fly (FAA (2016)). Usually, at those flight levels, CAT may be influenced by a variety of mechanisms (Fig. 1.1) such as jet-induced, mountain-induced, convective influence, and thermal influence. No matter the mechanism, CAT poses a serious threat to commercial aircraft.

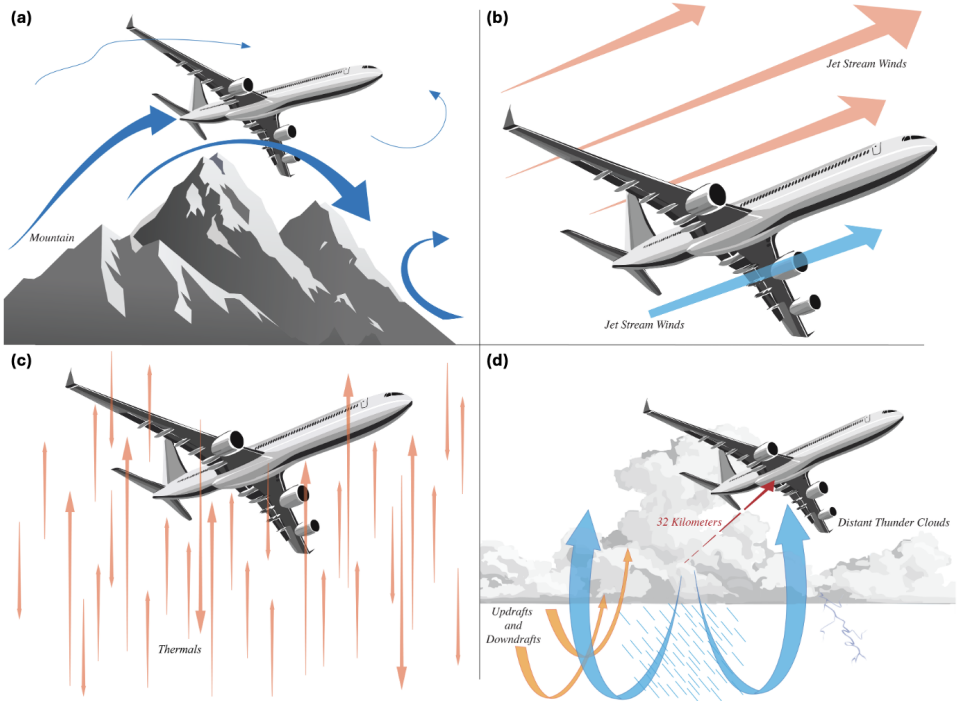

FIGURE 1.1: Mechanisms that generate CAT at flight levels: (a) Mountain Waves, (b) Jet Stream, (c) Thermals, and (d) updraft/downdraft from convective systems. (Acknowledgement: Stefanie Nichole Kluge, UW-Madison SOARS)

1.3 Research Objectives

The detection of CAT using models remains challenging due to insufficient spatial and temporal resolution, which are necessary to capture small-scale atmospheric processes that lead to CAT. This, in turn, can have an impact on passenger safety and comfort during commercial flights. Despite improvements in data availability over recent years, measurements at higher altitudes remain limited, which limits our understanding and modeling capabilities to detect CAT.

This study aims to examine the impact of key aviation parameters on the occurrence and

intensity of CAT over the past decade (2014–2023) relative to the last three decades (1980-2013) within the contiguous United States (CONUS). The primary parameters considered include wind speed, wind shear, temperature gradients, EDR, vertical velocity, potential vorticity, and specific humidity.

By integrating MERRA-2 reanalysis data and PIREPs, this study provides a comprehensive understanding of CAT trends and the atmospheric mechanisms that contribute to these trends. The findings of this work can improve CAT forecasting and aviation safety. In doing so, the following research questions are explored:

1. How have the turbulence parameters associated with the jet stream evolved over the past decade?

2. What are the regional hotspots for CAT over CONUS, and what atmospheric trends contribute to its occurrence?

3. How well do MERRA-2 reanalysis data and PIREPs represent turbulence-relevant parameters over CONUS, and what factors contribute to their subjectivity?

The layout of this study is as follows. Chapter 2 contains a review of the mechanisms, environments, statistics, duration, incidents, dimensions, and forecasting tools of CAT. Chapter 3 outlines the methodology for addressing the research questions. Chapter 4 presents the results of the 20-year climatology of CAT PIREPs, the 43-year climatology

of aviation parameters, and changes of aviation parameters in the past decade (2014-2023). Chapter 5 presents the discussion. Chapter 6 concludes with answers to the research questions and details for future work.

Chapter 2

Review of CAT

2.1 CAT Mechanisms and Environments

2.1.1 Jet Stream

A jet stream is a rapidly moving west-to-east air current across the Earth (Martin (2006)), located near the tropopause. The formation of the jet stream can be described by the thermal wind relationship, which states that horizontal temperature gradient enhance horizontal pressure differences, leading to the development of geostrophic winds. In the midlatitudes, the geostrophic wind increases with height to maintain thermal wind balance, resulting in stronger winds at higher altitudes. As shown in Figure 2.1, two strong jet streams occur near the tropopause: the polar and the subtropical.

The polar jet stream typically lies between 50°N and 60°N, spanning altitudes from around 350 hPa (∼8 km) at the polar tropopause to approximately 250 hPa (∼10 km) at the subtropical tropopause (Winters et al. (2020)). The subtropical jet stream is generally located near 30°N, extending from 250 hPa (∼10 km) at the subtropical tropopause to about 100 hPa (∼16 km) at the tropical tropopause (Winters et al. (2020)). In this work, the term *jet stream* will refer to the combination of both subtropical and polar jet streams.

Within the jet stream, abrupt shifts in wind speed can lead to increased wind shear and reduced stability in those regions, which is typically where CAT occurs. The jet stream sometimes contains a localized zone of strong winds along its axis, known as the jet streak (Stendel et al. (2021)), which is a characteristic of the variability of the jet stream.

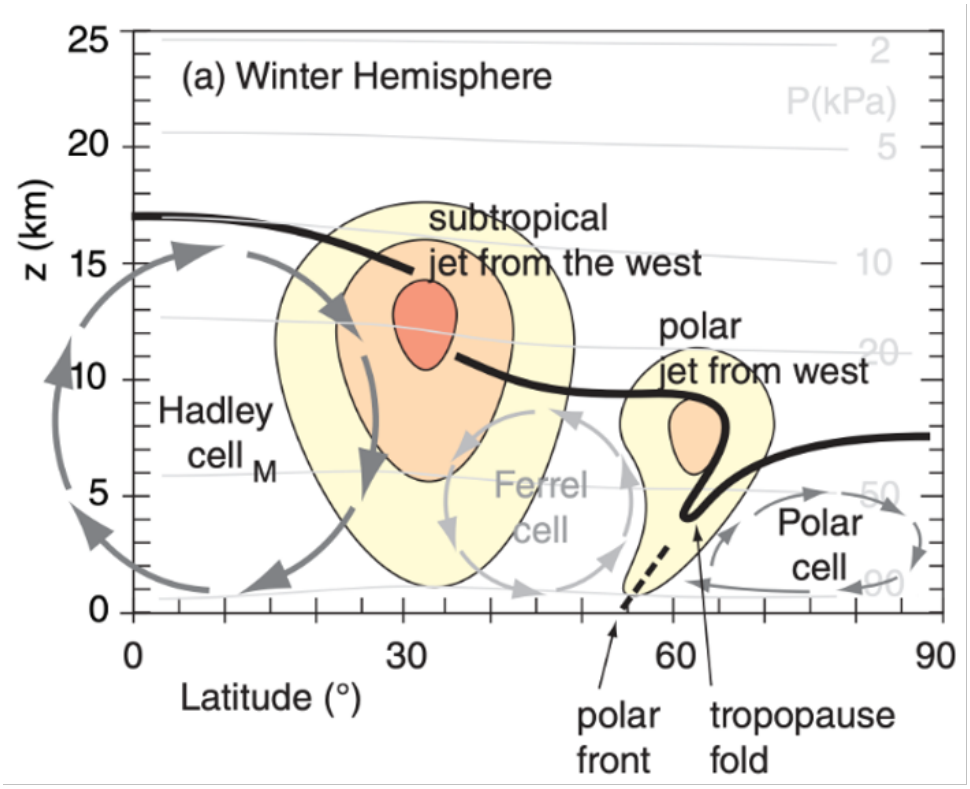

FIGURE 2.1: Vertical cross-section of atmospheric circulation in the northern hemisphere, highlighting the positions of the (1) subtropical jet (30°N) formed at the poleward edge of the Hadley cell and, (2) polar jet (60° N) formed when cold polar air meets warm midlatitude air, creating a strong baroclinic zone. Both jets are westerly by the thermal wind relationship that states if a temperature gradient is present, the wind must be increasing with height (Stull (2017)).

2.1.1.1 Jet Streak

Figure 2.2 represents the two key areas of the jet streak: the entrance and exit regions. The entrance region is associated with upper-level convergence (on the left entrance) and upper-level divergence (on the right entrance), which influences direct thermal circulation and adiabatic cooling (reducing horizontal temperature gradient). This region also facilitates the exchange of air between the troposphere and stratosphere, a process called

tropopause folding. During this process, high concentrations of potential vorticity (PV) from the stratosphere intrude downward into the troposphere due to the ageostrophic circulation around the entrance of a jet streak. On the other hand, the exit region is characterized by upper-level divergence (on the left exit) and upper-level convergence (on the right exit), which drive indirect thermal circulation and adiabatic warming (enhancing horizontal temperature gradient). In particular, the upper-level divergence at the left exit is responsible for the development of low-level cyclones or thunderstorms.

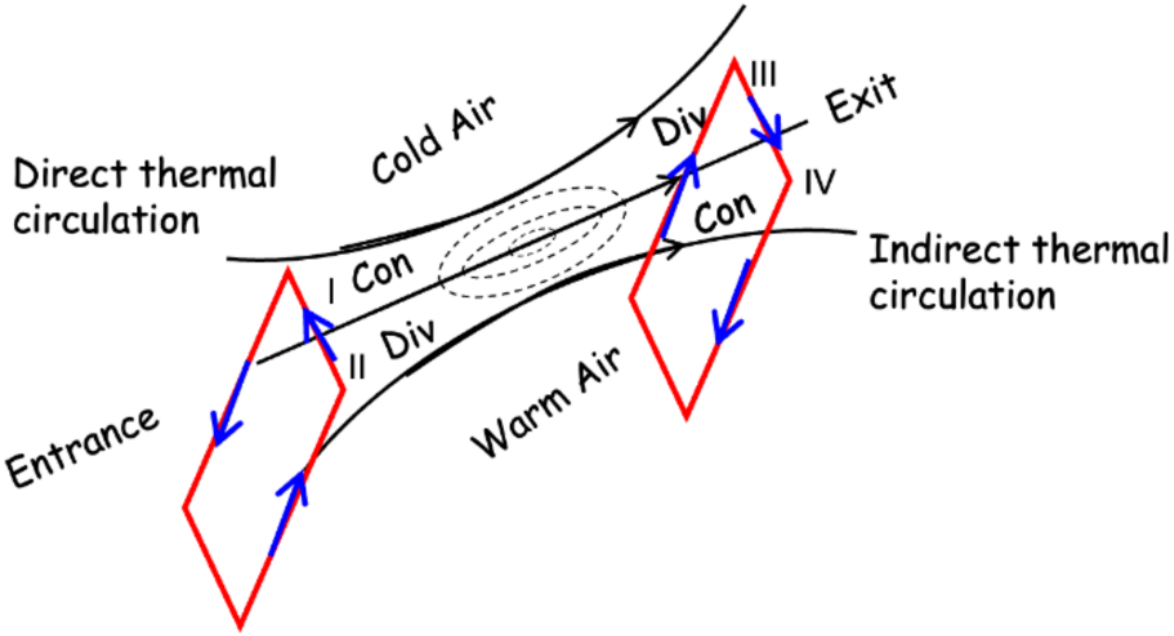

FIGURE 2.2: Schematic of the entrance and exit regions of a jet streak (dark dashed lines). The right entrance and left exit region, upper-level divergence promotes upward motion. The left entrance and right exit regions promote downward motion or subsidence (from Chen (2014).

Additionally, the strong wind speeds along the center of the jet streak develops a maximum vorticity on the cyclonic side of the jet (left side of the jet axis) and a minimum

vorticity at the anticyclonic side of the jet (right side of the jet axis). The jet axis represents the area of strongest winds at a specific jet stream level, typically between 300 hPa and 150 hPa. Specifically, if an aircraft is flying at FL250 (∼8 km) and crosses from the anticyclonic to the cyclonic side of the jet, it will experience a decrease in wind speed along the jet axis (Fig. 2.3). This rapid change in wind speed can create wind shear. The transition from one side of the jet to the other is referred to as a jet stream front. Although jet stream fronts are difficult to identify directly on jet stream charts at levels between 300 hPa and 150 hPa, the transitional zone can be observed as narrow bands of significant temperature gradients and strong vertical and horizontal wind shear, particularly on the cyclonic side of the jet stream (Lester (1994)). Figure 2.3 shows a vertical cross-section of the jet stream revealing the jet front's vertical extent. In this vertical view, the jet front is marked by a downward slope from the tropopause break, situated below the jet core, and located between air masses with strong temperature gradients in the upper troposphere. Two key features, highlighted in blue, are located near the jet stream front and in the downward sloping region above the tropopause. These areas are characterized by strong shear, making them regions of CAT.

Early observational studies were instrumental in establishing the foundational understanding of CAT. For instance, Bannon (1951) observed that CAT frequently occurs on the cyclonic side of the jet stream, both above and below its core. Similarly, Machta (1955), one of the pioneers in CAT research, linked CAT occurrences to large-scale jet stream dynamics, emphasizing the importance of upper-level wind shear. Theoretical

developments later explored the role of Kelvin–Helmholtz instability (KHI) in CAT formation. Dutton and Panofsky (1970) highlighted that specific atmospheric conditions conducive to KHI, such as strong VWS and stable stratification can lead to turbulence in the vicinity of the jet. Beyond shear-driven instabilities, wave-induced mechanisms have also been recognized as significant contributors to turbulence in the upper troposphere and lower stratosphere (UTLS). Studies by Lane et al. (2004), Koch et al. (2005), and Sharman et al. (2012) demonstrated that gravity wave and inertia-gravity wave breaking can generate significant CAT, particularly in regions downstream of mountains or near strong jet streaks. Recent work by Williams and Joshi (2016) highlights the impact of climate change on CAT, suggesting that observed increases in CAT incidents may be linked to changes in jet stream patterns, which could be further intensified by climate change.

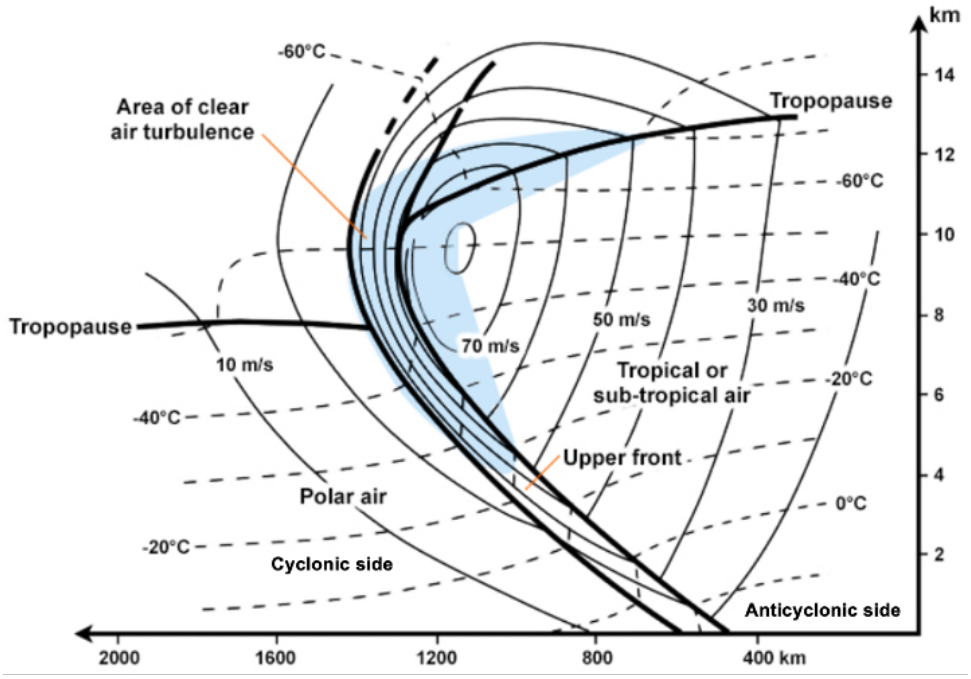

FIGURE 2.3: Vertical cross section of the jet stream, illustrating the cyclonic side (left) and the cyclonic side (right) of the jet stream. The jet streak, located between 8 km and 12 km, is represented by strong wind speeds (solid black lines) near the tropopause. The jet stream frontal zone slopes downward from the tropopause break, extending below the jet core and separating the warm and cold air in the upper troposphere. Two key features associated with regions of possible CAT (light blue shading) are: (1) strong shear above the tropopause that slopes downward over the jet streak, and (2) a region of strong horizontal and VWS within the jet stream front (Lester (1994))

.

2.1.1.2 Tropopause

As discussed in Section 2.1.1, the tropopause is closely associated with the position of the jet stream. Is important to distinguish between the dynamical and thermodynamic definitions of the tropopause. The thermodynamic definition focuses on the boundary between upper troposphere and lower stratosphere (Fig. 2.4), where the lapse rate decreases to 2 K/km or less (for example, see Mélanie et al. (2021)). The dynamical definition defines

the tropopause as the boundary between the high PV values in the stratosphere and the low PV values of the upper troposphere (e.g., Georgiev et al. (2016)), typically at altitudes where most aircraft fly. Thus, variations in the height of the dynamical tropopause are associated with interaction between the polar and subtropical jet stream.

The height of the tropopause is modulated by the presence of macroscale (Rossby) waves, which appear as troughs and ridges in upper-level charts. In these large-scale wave patterns, the tropopause tends to rise above upper-level ridges (regions of high pressure and warmer air) and decrease height over upper-level troughs (regions of low pressure and colder air). These undulations are a direct result of the large-scale wave motions propagating from west to east, causing the tropopause height to vary spatially and temporally across a region. This means that an aircraft flying near the tropopause may be flying between the troposphere and stratosphere, depending on the location of the flight relative to the macroscale (Rossby) wave.

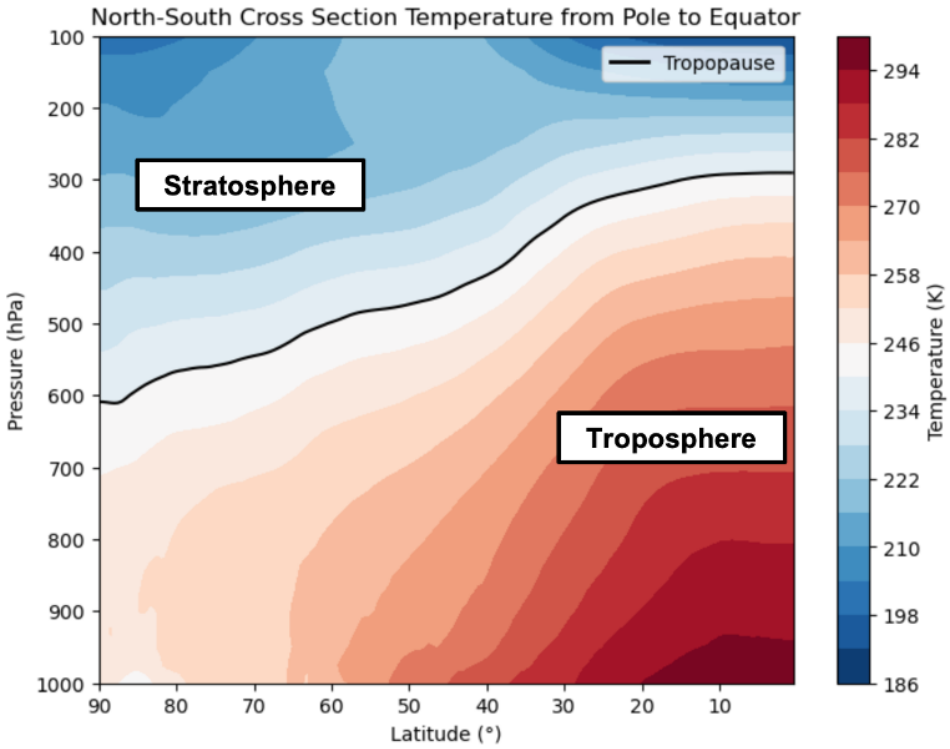

FIGURE 2.4: North-south cross section of temperature from pole (left) to equator (right) for 01 January 1986. The upper troposphere (red shading), tropopause (black line) approximation and lower stratosphere (blue shading) are shown. (Generated using MERRA-2 reanalysis data)

2.1.2 Mountain Waves

Mountain waves are not considered CAT and is reported as conventional turbulence. However, mountain waves are a significant large-scale forcing mechanism that contributes to the formation of CAT through a process known as mountain-wave breaking (e.g., Kim et al. (2019)). Figure 2.5 illustrates how this process occurs when stably stratified airflow passes over mountainous terrain, forcing the air to ascend and descend. This interaction generates gravity waves that can propagate vertically through the upper troposphere and into the lower stratosphere. When conditions favor vertical propagation, these waves can

amplify with height due to decreasing air density. If the wave reaches a critical amplitude, it becomes unstable and breaks, producing turbulence. This wave breaking at upper levels can significantly enhance the occurrence of CAT (Sharman (2016)), particularly near jet streams and frontal zones, making these regions prone to turbulence Lee and Chun (2018).

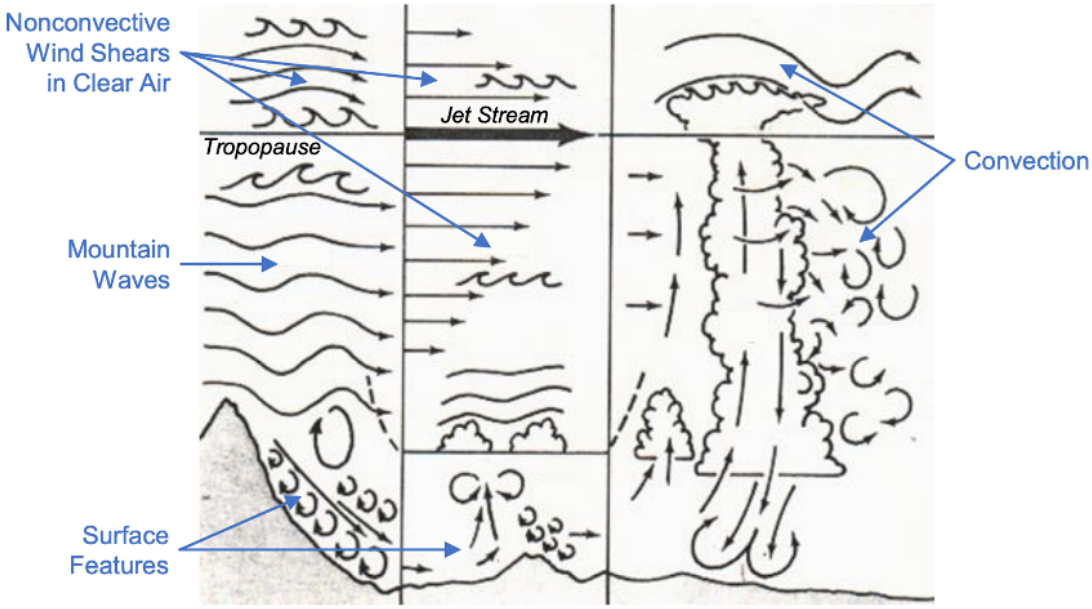

FIGURE 2.5: Large-scale forcing mechanisms that form CAT: mountain waves (left), thermals (center), jet streams (center), updraft and downdraft from convective systems (right) from Lester (1994).

2.1.3 Updraft and Downdraft from convective systems

The updrafts and downdrafts from convective systems play a crucial role in the formation of CAT. CAT can occur in the vicinity of clouds, especially within a horizontal distance of about 32 km from the convective core. As shown in Figure 2.5 (right), convective systems generate strong updrafts and downdrafts that enhance turbulent conditions. These vertical air movements trigger gravity waves as the atmosphere tries to adjust towards

the geostrophic balance. In this process to reach stability, strong wind shear can be intensified in the UTLS.

2.1.4 Thermals

As shown in Figure 1.1, thermals are characterized by surface-driven vertical mixing (ICAO (2023)), driven by the ascent of a warm air parcel or updraft from the lower troposphere (Fig. 2.5). When there is a weak capping inversion or low static stability, this updraft can reach the tropopause (Lester (1994)), intensifying VWS. This enhanced VWS can cause to shear instabilities that break down into turbulence in the UTLS (Sharman (2016)).

2.2 The Nature of Clear Air Turbulence

Although CAT is not visible via conventional meteorological observations, its occurrence exhibits statistical and dynamical patterns. In the next few paragraphs, average CAT characteristics including the frequency of incidents, the size and the duration of turbulent conditions are described. These CAT characteristics will be illustrated with a few descriptions of the incidents.

2.2.1 Statistics

Figure 2.6, shows the increasing percentage of turbulence-related accidents among Part 121 carriers (commercial and cargo) between 2009 and 2018 (NTSB (2021)). Turbulence-related accidents accounted for 86.5% of all such incidents (96 out of 111). The most

commonly reported levels of turbulence intensity (Fig. 2.7) were severe (44.1%, 46 out of 111) and moderate (41.4%, 49 out of 111). During this period, turbulence-related accidents resulted in 123 serious injuries (Fig. 2.8), with flight attendants making up 78.9% of the injured and passengers comprising 21.1% (NTSB (2021)). In total, there were 111 turbulence-related accidents involving major airlines and regional carriers, which included various types of turbulence, such as convective, CAT, mountain wave, and wake turbulence (Fig. 2.9). As reported by the NTSB, the 64 turbulence-related accidents classified as convective turbulence were depicted by the radar, which showed strong radar reflectivities. These incidents accounted for 57.7 % of the total. The number of CAT-related accidents in the U.S. has risen by approximately 28.8%. This percentage represents 32 incidents out of 111 total turbulence-related accidents. Reports suggest that these 32 CAT incidents were linked to jet streams, with the aircraft involved being near the tropopause (NTSB (2021)).

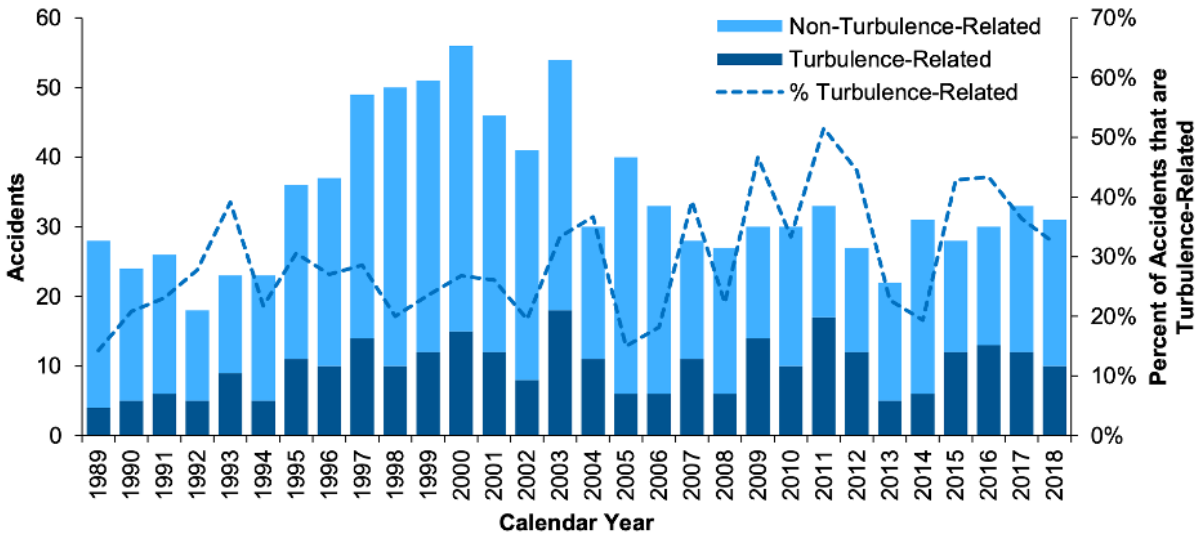

FIGURE 2.6: Turbulence-related and Non-turbulence related accidents from 1989 to 2018 (from NTSB (2021)).

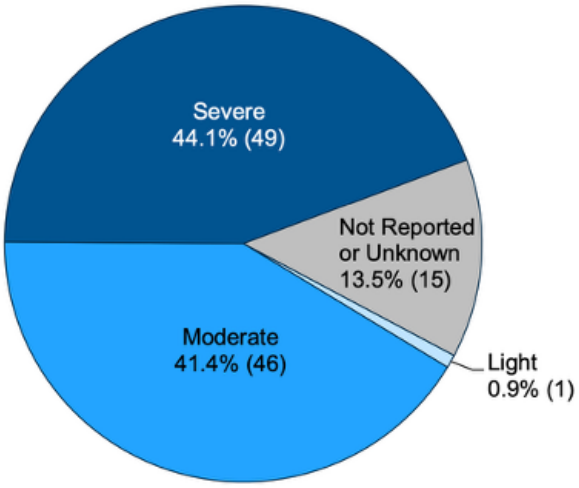

FIGURE 2.7: Turbulence-related accidents by reported turbulence intensity: light, moderate, severe and not reported or unknown (from NTSB (2021)).

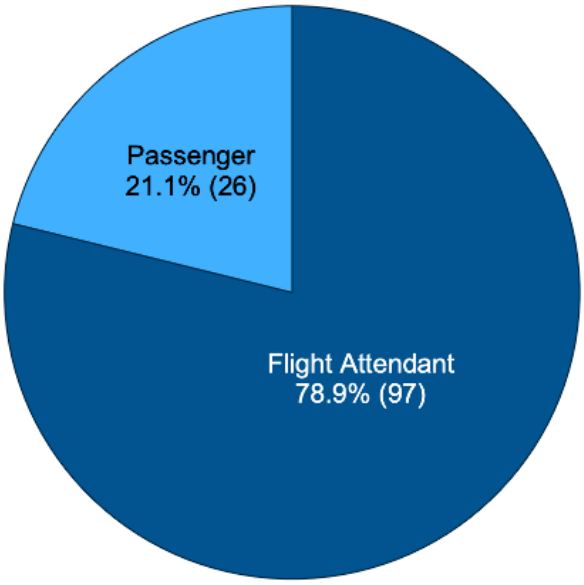

FIGURE 2.8: Percentage of flight attendants and passengers injured in turbulence-related Part 121 accidents between 2009 and 2018 (from: NTSB (2021)).

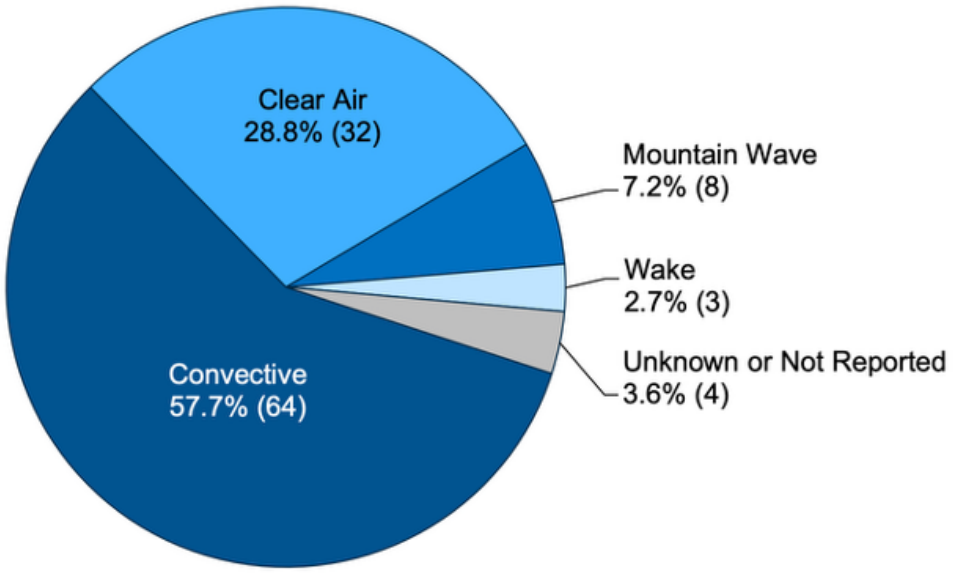

FIGURE 2.9: Percentages and number of turbulence-related accidents Part 121 reported by turbulence intensity between 2009 and 2018. (from NTSB (2021)).

2.2.2 Dimensions or Size

CAT typically forms in narrow layers that extend along the wind direction, often giving them a flattened appearance. This characteristic has led some earlier Russian researchers to describe these CAT layers as resembling pancakes (Lester (1994)). According to FAA (2016), the intensity of CAT can fluctuate along a flight path. Typically, turbulent regions linked to the jet stream measure between 80 km to 500 km (100 to 300 miles) in length, aligned with the wind direction, 20 to 100 km across the wind direction, and about 500 to 1000 m in depth (Overeem (2002)). These turbulent zones can last anywhere from 30 minutes to a full day (Overeem (2002)). These values are average extents of turbulent zones, not discrete events.

2.2.3 Duration

These patches of CAT can be classified based on its duration as occasional, intermittent or continuous along the flight route. It is classified as occasional when it occurs for less than one-third of the time, intermittent when it spans approximately one-third to two-thirds of the time, and lastly continuous when it persists for more than two-thirds of the time (NTSB (2021)). The duration of CAT encountered by an aircraft can vary greatly, ranging from just a few seconds to several minutes, and this depends on the size and speed of the aircraft. Similarly, the intensity of CAT may differ between aircraft sizes. Larger commercial aircraft, such as the Boeing 747 or Airbus A380, tend to experience lower acceleration responses to the same turbulence intensity due to their size. Therefore, when a larger aircraft encounters moderate CAT, a smaller aircraft like the Canadian Regional Jet (CRJ-700 and CRJ-900) may experience the same turbulence as severe.

2.2.4 Incidents

Over the last decade, there has been a noticeable increase in CAT incidents reported by commercial airlines. One recent incident occurred on April 3, 2024, involving Delta Flight 2763, which experienced moderate CAT at around 14,000 feet during its descent into Asheville Regional Airport (AVL). This turbulence led to a serious injury to a flight attendant, possibly a broken leg (NTSB (2024)).

In 2023, Envoy Air Flight 3788 experienced severe CAT at around 26,650 feet while

descending into Chicago O'Hare International Airport (ORD), which caused a flight attendant to fracture an ankle (NTSB (2023b)). Additionally, in 2023, Lufthansa Flight 469 experienced severe CAT at 37,000 feet over Tennessee while en route from Austin to Frankfurt, leading to injuries among passengers and an emergency diversion to Washington Dulles International Airport (NTSB (2023a)).

On December 18, 2019, American Airlines Flight 2247 encountered CAT while en route to Raleigh-Durham International Airport in Morrisville, North Carolina. The turbulence occurred at FL180, despite clear skies and no previous PIREPs indicating turbulence in the area. The aircraft experienced light to moderate turbulence that lasted for 20 seconds. During this time, one flight attendant was injured while conducting drink service in the cabin. The attendant was thrown to the floor, injuring her foot. After landing, she was taken to a local hospital, where she was diagnosed with a fractured foot. Weather data confirmed that the turbulence was likely CAT, as the aircraft was passing through the lower boundary of a strong jet stream with significant shear (NTSB (2021)). All these CAT incidents can lead to increased fuel consumption and delays as pilots are forced to circumvent affected areas, further impacting the efficiency of flight operations.

2.3 Forecasting and Reporting Clear Air Turbulence

2.3.1 CAT Reporting Methods

CAT can be reported by two methods: PIREPs and automated measurements of the Eddy Dissipation Rate (EDR). PIREPs are en route observations reports from the perspective

of pilots that describe the actual weather conditions encountered by an aircraft while in flight (FAA, 1993). PIREPs have two goals: 1) to warn other pilots of in-flight weather conditions or turbulence, and 2) to inform both the Flight Service Stations (FSS) and Air Route Traffic Control Center (ARTCC) of the en route flying conditions (Schwartz (1996)). Each PIREP includes qualitative and subjective data such as: time, the report type (Routine (F) or Urgent PIREP (T)), aircraft type, flight level, weather conditions, turbulence type, ARTCC, and location (latitude and longitude).

Despite their operational value, PIREPs can have several limitations. First, PIREPs are subjective and may reflect individual pilot experiences. Second, the frequency of reports can vary depending on air traffic and there may be delays in reporting, sometimes up to 10-15 minutes after the event occurs Gálvez, J. (2023). Lastly, PIREPs can also lack consistency, particularly when reporting the severity or type of the observed weather phenomena. Also, PIREPs are not mandatory only when requested or if severe weather is present.

In contrast to subjective PIREPs, the EDR provides an objective and quantitative measure of turbulence. EDR can be described as the cubic root of the energy or eddy dissipation rate based on the vertical wind velocity or the vertical acceleration of the aircraft(Hord (2018)). In other words, EDR is the standard measurement of turbulence intensity, regardless of the type of aircraft (Bechtold (2021)). More importantly, EDR has become the standard measure for CAT (Bechtold (2021)). Table 2.1 shows the EDR index-metric for categorizing turbulence intensity. This measure of turbulence intensity

can also be calculated from the turbulence kinetic energy (TKE), which will be discussed in Chapter 3.

Turbulence Category	cube root of EDR value
Severe	< 0.7
Moderate	0.4 - 0.7
Light	0.4 - 0.1

TABLE 2.1: The EDR values given above describe the severity levels for a medium-sized transport aircraft under typical en route conditions, including standard altitude, airspeed, and weight (Hord (2018)).

2.3.2 Numerical Weather Prediction

The Numerical Weather Prediction (NWP) model recreates the dynamics of the atmosphere by solving nonlinear equations of the motion and continuity for mass, heat, and water vapor (Castorrini et al. (2021)). NWP tools enable the simulation of wind direction and speed over extended forecasting periods but at a coarser resolution. Despite this, turbulence indices such as: Absolute vorticity (Knox (1997)), Ri (Endlich (1964)), Divergence Tendency (McCann, Donald W (2001)), Ellrod (Ellrod and Knapp (1992)) and Ellrod-Knox (Ellrod and Knox (2010)) are used to represent synoptic patterns that produce CAT. However, these turbulence indices are typically used together with NWP model products to forecast the probability of turbulence (Ko et al. (2024)).

CAT can be diagnosed using the regional NWP model, under the assumption that the origin of turbulence originates from macro-scale phenomena, even though CAT is a micro-scale phenomenon (Overeem (2002)). In other words, the NWP model has limitations to capture fine scale turbulence that causes CAT because it is based on large scale resolution and not on localized phenomenon (Williams and Joshi (2013)). Hence, NWP models don't ensure CAT warnings to pilots, which increases turbulence related accidents across the U.S.

2.3.3 Graphical Turbulence Guidance (GTG) system

The Graphical Turbulence Guidance (GTG) is a product by the National Oceanic and Atmospheric Administration (NOAA) and the National Center for Atmospheric Research (NCAR) to forecast aviation turbulence. The GTG tool provides turbulence forecast by calibrating turbulence indices (Ri, absolute vorticity and more indices derived from NWP) to actual turbulence observations (Sharman et al. (2006); Kim et al. (2011); McCann et al. (2012); Kim et al. (2015)). A great turbulence observation for this calibration is obtained from in-situ aircraft measurements like the EDR because it measures the atmospheric turbulence intensity (Sharman (2016)). As a result, a group of turbulence diagnostics, including EDR, turbulence kinetic energy (TKE), Ri and more are computed and weighted to provide turbulence forecasts. Most importantly, the resolution of GTG systems comes from the NWP model, thus inheriting the limited spatial and temporal resolution. This limitation makes it challenging to detect the fine scale turbulence responsible for CAT, which ultimately affects commercial aircraft.

Forecasting turbulence is challenging not only because of its limitation in resolution but also when the properties of CAT change rapidly over time (Overeem (2002)). Sharman (2016), suggests that the turbulence forecast should be probabilistic because it takes into consideration the predictive role of turbulence in aviation operations and uncertainties from the NWP model and the diagnostic algorithms used to identify turbulent regions. Thus, by implementing this probability there is a better representation of possible turbulent intensities and regions. Following this approach the GTG system creates probability based turbulence forecasts. Although NWP based tools like GTG provide turbulence forecasts, satellite observations offer valuable real-time insights into atmospheric conditions that could lead to CAT, particularly in regions with limited conventional data.

2.3.4 Satellite Tools

From satellite imagery it is possible to carefully infer proxy features that cause CAT by using the visible, infrared, and water vapor channels. However, the horizontal and temporal resolution of satellite imagery is not sufficient to capture fine scale turbulence that causes CAT (Sharman (2016)). Since satellites cannot directly measure turbulence, they can identify synoptic atmospheric patterns associated with turbulence indicators. These patterns include moisture boundaries along the jet stream, transverse cirrus bands on the anticyclonic side of the jet stream axis, and billow clouds can be identified through satellite observations (Ellrod (1989)).

The visible channel can show visual features of transverse banding cirrus (located on the anticyclonic side of the jet stream axis), which is an indicator of turbulence near the

jet stream. Transverse bands typically occur when the maximum wind speed of the jet stream exceeds 110 knots (Lester (1994)). Thus, these bands are associated with strong vertical wind shear and possibly with turbulence. However, the visible channel has its limitations to only showing these features only during daytime.

In contrast, the water vapor channel is more sensitive to thin cirrus and provides continuous coverage for both daytime and nighttime. The water vapor channel provides additional clues about where CAT might occur. Dark regions in the imagery, which represents dry regions and also areas of descending air, is often linked to moderate to severe CAT. Additionally, darker areas behind an elongated area of low pressure in the atmosphere (trough) can indicate: (1) downward movement of cooler, direr air (subsidence), (2) tropopause folding (which increases wind shear) (Wimmers and Feltz (2007)), (3) advection of cold and drier air and (4) sharp gradients indicate density discontinuity. These factors contribute to strong wind shear and atmospheric instability, both of which can trigger CAT.

Satellite observations are a valuable tool to identify existing and developing turbulence patterns in the atmosphere. However, there are limitations to these patterns or indicators to detect CAT that can be identified by using satellite imagery:

1. Require manual interpretation by forecasters which can be time consuming, and

2. Challenging to estimate the altitude and intensity of CAT (Sharman (2016)).

Despite the limitations of satellite data, combining satellite products with PIREPs allows us to determine if the observed patterns in the imagery align with actual turbulence encounters. This integration helps validate reported turbulence by comparing the PIREPs with the patterns seen in satellite data.

2.3.5 Machine Leaning Tools

The Cooperative Institute for Meteorological Satellite Studies (CIMSS) at the University of Wisconsin-Madison has developed a turbulence probability nowcasting tool designed to identify Moderate or Greater (MOG) turbulence within 30 kft and 41 kft (Fig. 2.10) over a 10-minute period. This product integrates machine learning techniques on geostationary imagery, including water vapor and infrared channels, to estimate the probability of MOG turbulence affecting commercial aviation operations (NOAA (2021)). However, a notable limitation of the MOG turbulence probability product is its reduced efficiency to forecast CAT.

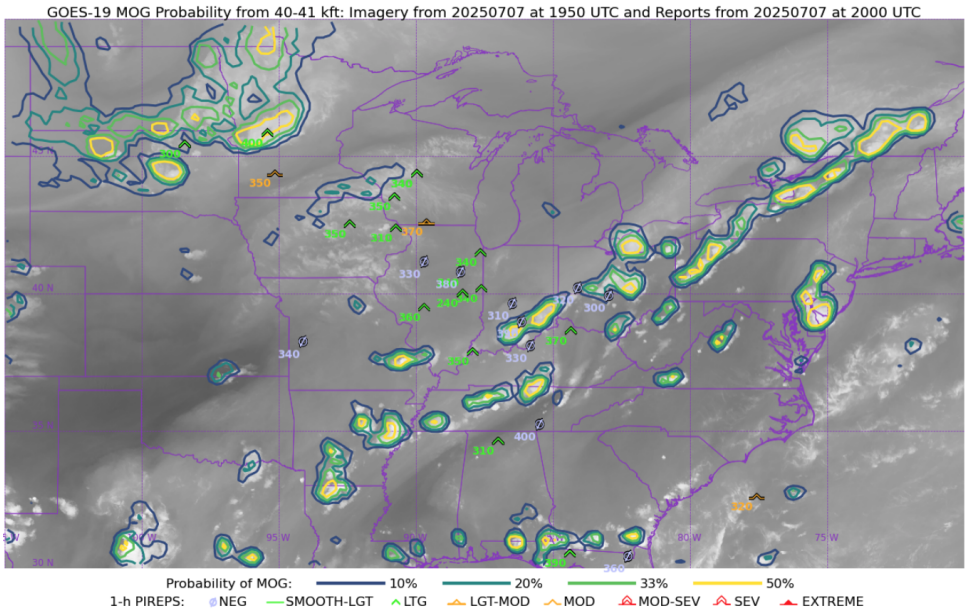

FIGURE 2.10: MOG Turbulence Probability for the 40-41 kft layer, 1950 UTC on July 7, 2025, along with PIREPs (from: CIMSS).

Chapter 3

Data and Methods

NASA's Modern-Era Retrospective Analysis for Research and Applications, Version 2 (MERRA-2) reanalysis data and PIREPs will be used to examine how atmospheric conditions have evolved over the past decade (2014-2023). PIREPs will be used to identify regional hotspots for CAT over CONUS and the atmospheric trends that contribute to its occurrence. Lastly, discuss the performance of both reanalysis data and PIREPs to represent turbulence-relevant parameters and what factors contribute to their subjectivity.

3.1 MERRA-2 reanalysis data

The NASA's MERRA-2 reanalysis provides observations of atmospheric patterns such as temperature (T), specific humidity (q), omega (ω), potential vorticity (PV), zonal (U)

and meridional (V) wind components. These parameters are obtained from a comprehensive assimilation of satellite observations, in-situ measurements, and weather balloon data to ensure a high-quality and consistent dataset. This dataset provides global coverage from 1980 to the present, with a spatial resolution of 0.5° latitude by 0.625° longitude Gelaro et al. (2017).

The averaged three-dimensional (3D) hourly Analyzed Meteorological Fields dataset was used in this analysis($inst3\_3d\_asm\_Np$, earthdata.nasa.gov), which covers 42 vertical pressure levels to analyze key atmospheric variables for aviation weather. First, calculations were made of the monthly average of U and V wind components, ω, T, PV and q at pressure levels from 300 hPa to 150 hPa or at critical flight levels from FL300 ($30,000$ ft) to FL440 ($44,000$ ft). However, the main focus will be on changes in atmospheric variables between 250 hPa and 200 hPa, because this section corresponds to the jet stream's core. At the same time, the VWS and EDR will focus between 700 hPa and 250 hPa. The geographic domain expands between 20°N - 70°N latitude and 140°W - 60°W longitude across the contiguous United States (CONUS).

From the daily 3-hourly dataset, monthly averages were computed to construct a 43-year climatology (1980 - 2023). The decision to aggregate the data from daily 3-hourly to monthly means was made to meet the vertical monthly resolution requirements of this study, which exceed those available in MERRA-2 reanalysis datasets. Most importantly, these specific fields at the mentioned atmospheric levels are not available in the pre-existing monthly reanalysis data.

For this study, the parameters relevant to commercial aviation and major airline routes over CONUS are classified between fixed and derived parameters. The fixed parameters are a collection of assimilations of meteorological parameters such as: U, V, ω, T, q, and EPV. The Ertel's Potential Vorticity (EPV) is evaluated from MERRA-2 reanalysis data air temperature fields, eastward and northward winds. EPV or simply, the PV is considered a quantity that is conserved for air parcels that follow an adiabatic frictionless flow. In other words, the initial PV of a parcel will remain the same throughout its horizontal and vertical movement. In this study, the PV is used to identify stratospheric and tropospheric mass exchange. The upward and downward motions are the principal components for the development or weakening of synoptic-scale weather systems. More specifically, the updraft and downdraft from these low-pressure systems play a crucial role in the formation of CAT.

A few fixed parameters or indices were used to derive turbulence-specific metrics, such as:

The Mean Wind Speed ($\mathbf{v}$) was calculated as:

$$|\mathbf{v}| = \sqrt{U^2 + V^2} \tag{3.1}$$

Vertical Wind Shear (VWS) was calculated as:

$$\text{VWS} = \sqrt{(U_{\text{upper}} - U_{\text{lower}})^2 + (V_{\text{upper}} - V_{\text{lower}})^2} \tag{3.2}$$

Turbulence Kinetic Energy (TKE) per unit mass of the turbulent velocity components was calculated from VWS:

$$\text{TKE} = \frac{1}{2}\left(\text{VWS}\right)^2 \tag{3.3}$$

As discussed in Chapter 2, the EDR is considered the standard measure for CAT. In this analysis, the EDR is obtained from the TKE:

$$\text{EDR} \sim \frac{\text{TKE}^{3/2}}{L} \tag{3.4}$$

Where: L is the turbulence length scale (typically around 100-200 meters for CAT).

After analyzing these parameters and atmospheric variables, we can capture temporal trends at critical flight levels between 250 hPa (FL340) and 200 hPa (FL390). The changes were calculated by the difference between reference years (1980-2013), and comparison years (2014-2023) to understand how turbulence parameters associated with the jet stream evolved over the past decade. In the same way, identify the atmospheric trends that contribute to the occurrence of CAT.

3.2 Pilot Reports (PIREPs)

PIREPs were obtained from the National Oceanic and Atmospheric Administration (NOAA) and are available for public download (Mesonet, I. E. (2024), mesonet.agron.iastate.edu). Figure 3.1 shows how PIREPs classify turbulence into qualitative categories: None, Light (LGT), Moderate (MOD), Severe (SEV), or Extreme (EXT), with occasional reports that contain combinations of these categories.

Using feature engineering techniques, these qualitative categories were converted into numerical values (1, 2, 3, and 4) to facilitate structured analysis. Figure 3.2 describes how this process was made. First, cleaning and filtering the word `CAT` in the column **TURBULENCE**. Applying Python datetime in the column **VALID** to extract calendar months for seasonal analysis. A grid paired with MERRA-2 resolution (0.5° x 0.625°) was created to average CAT reports within each grid cell and for each calendar month. Additionally, quality control measures were applied to eliminate incomplete or anomalous reports before aggregating the data into uniform grids. Later, a heatmap of CAT reports was created to represent the climatology within the geographic region between 20°N - 70°N latitude and 140°W - 60°W longitude.

In addition, to represent the position of the jet stream, MERRA-2 mean wind speeds were calculated at 250 hPa. This direct integration of PIREPs and reanalysis data allows for the representation of long-term trends in CAT frequency over the study period (2003

- 2023). These 20 years were selected based on the viability of PIREP data, which has been archived from December 2000 to the present (Mesonet, I. E. (2024)).

Chapter 4 will discuss the results of the 20-year climatology of CAT PIREPs, the 43-year climatology of aviation parameters, and changes in aviation parameters in the past decade (2014-2023).

VALID	URGENT	AIRCRAFT	REPORT	ICING	TURBULENCE	ATRCC	PRODUCT_ID	FL	LAT	LON
202404010145	F	A21N	PHX UA /OV PXR125050/TM 0145/FL190/TP A21N/TB MOD CAT 195-160/RM DURD PINNG ARR - ZAB/FDCS	None	MOD CAT 195-160	ZAB	None	19000	32.95198091992600	-111.15198524870300
202404010145	F	PC12	SMF UA /OV LIN240026/TM 0145/FL155/TP PC12/TB MOD/RM DURC 155-180	None	MOD	ZOA	None	15500	37.853315783315800	-121.47672818274000
202404010146	F	PC12	ALS UA /OV ALS140030/TM 0146/FL200/TP PC12/SK TOP 190-210/TB LGT CHOP/RM ZDVFD	None	LGT CHOP	ZDV	None	20000	37.05583675360950	-105.45658023061600
202404010147	F	E75L	CYS UA /OV CYS256019/TM 0147/FL330/TP E75L/TB MOD/RM ZDVFD	None	MOD	ZDV	None	33000	41.07902519442390	-105.21859211112800
202404010147	F	CRJ2	GSH UA /OV GSH360020/TM 0147/FL230/TP CRJ2/TB NEG	None	NEG	ZAU	None	23000	41.86058033336030	-85.79222
202404010147	F	B39M	LKV UA /OV LKV155070/TM 0147/FL360/TP B39M/TB CONS LGT /RM ZSE	None	CONS LGT	ZSE	None	36000	41.10366526895240	-119.73386895993200
202404010148	F	BCS1	DHT UA /OV DHT130020/TM 0148/FL300/TP BCS1/TB CONS LGT CAT/RM ZAB/FDCS	None	CONS LGT CAT	ZAB	None	30000	35.808310108155000	-102.23153629510600

FIGURE 3.1: Example of a PIREP for 01 April 2024 (from: Mesonet, I. E. (2024))

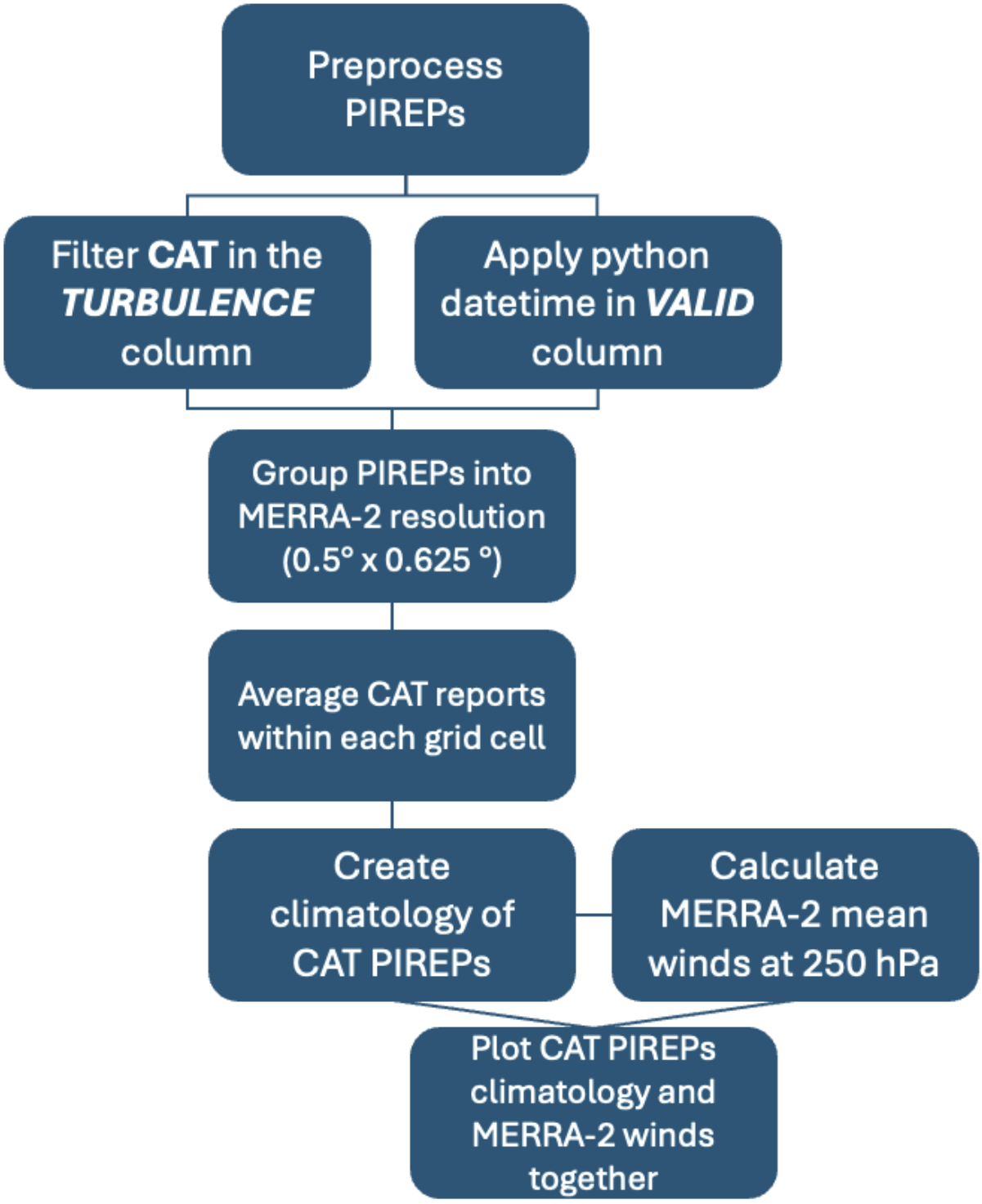

FIGURE 3.2: Overview of the workflow to visualize the climatology of CAT reports over the U.S. (2003 - 2023).

Chapter 4

Results

4.1 Climatology of CAT reports

This study combines PIREPs and MERRA-2 reanalysis data to identify mean CAT patterns. The MERRA-2 reanalysis data spans from 1980 to 2023, and the PIREPs are only available from 2000 onward. Therefore, Figure 4.1 illustrates the monthly climatology of gridded CAT reports across all flight levels for over 20 years (2003-2023). This climatology includes CAT reports of all intensities, such as light, moderate, severe, and extreme. The contour lines in Figure 4.1 represent the average jet stream position at 250 hPa calculated from MERRA-2 reanalysis data from 2003 to 2023.

Between March and May, CAT reports are concentrated across the South, East, and Midwest of the U.S. However, CAT hotspots (greater than 6 reports per grid cell) are

only concentrated over the Northeast and Midwest. At the beginning of summer, CAT reports continue along the south of U.S., but now between July and August, CAT is concentrated along the Southeast U.S. instead. For the whole summer, CAT is still concentrated along the East and Midwest of the U.S.

During Fall, contour lines begin to move over the Mid-latitude as the jet stream starts to get stronger due to the strong temperature gradient between the polar air and the tropical air. As the jet stream moves, CAT reports extend across the South, East, and Midwest of the U.S. Most importantly, CAT hotspots are across the Northeast and Midwest, representing the areas of increased aviation risk.

During winter, turbulence reports indicate that over the last 20 years, CAT is distributed across the South, East, Northeast, and Midwest of U.S. However, notable CAT hotspots are concentrated over the Midwest and Northeast of the U.S. and are closely aligned with the 250 hPa jet stream contour lines. It is certain that at 250 hPa, CAT may be influenced by the jet stream. More specific, in the region of strong winds along the jet stream. One possible explanation, illustrated in Figure 2.3, is that these CAT occurrences coincide with areas of enhanced VWS within the jet stream.

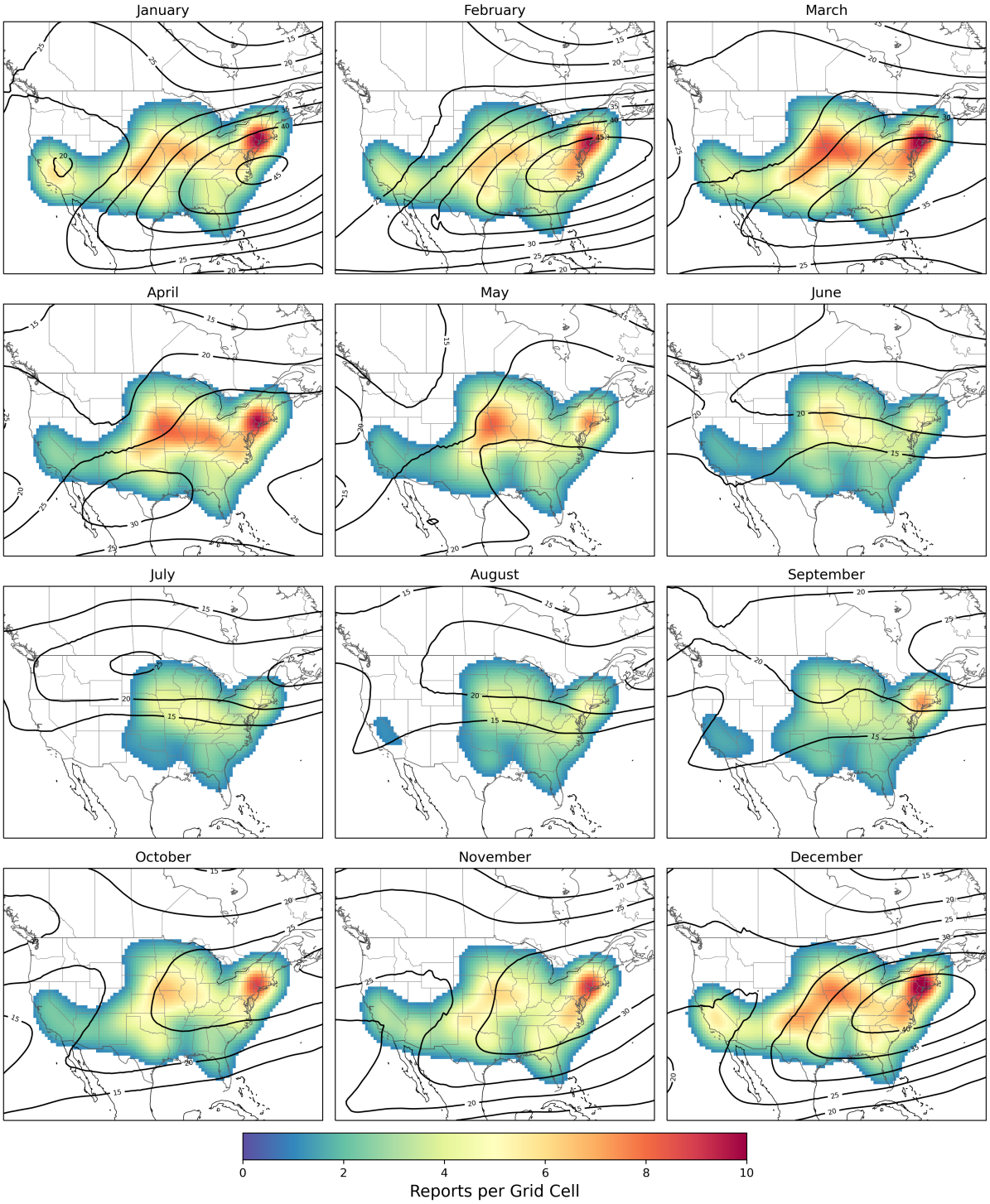

FIGURE 4.1: Monthly climatology of PIREPs for each month from 2003 to 2023, illustrating seasonal variations in CAT reports across North America.

4.2 Climatology of Aviation Parameters

This section expands the analysis to additional atmospheric variables to investigate the trends potentially responsible for the CAT hotspots identified in Figure 4.1. It presents a comprehensive 43-year climatology (1980-2023) for aviation parameters, including upper-level wind speeds, VWS, EDR, ω, T, PV, and q.

4.2.1 Upper Level Wind Speeds

During winter (December-January-February), the polar and subtropical jet streams become stronger as they move over North America. They overlap with each other at atmospheric levels between 250 hPa and 200 hPa (Fig. 4.2 and 4.3). More specifically, the jet stream is located between 30°N and 50°N latitude in the northern hemisphere. The jet core (Fig. 4.2 and 4.3) is located along the southeast and east coast of U.S and extends along a small section of the Atlantic Ocean.

During March, the jet core starts to move along the south coast and weakens with maximum wind speeds of 42 m/s. At the same time, the jet stream also weakens as it starts to move equatorward. In April, the wind speeds at upper levels keep decreasing between 15 m/s and 40 m/s. This weakening persists during May.

During summer (June-July-August), the jet stream is weaker with mean wind speed values ranging between 15 m/s and 25 m/s. This weakening is associated to the temperature gradient shifting poleward.

During September, the jet stream undergoes a transition because the mean wind speeds begin to increase again from 15 m/s to 30 m/s. This behavior continues between October and November as the jet stream migrate over North America.

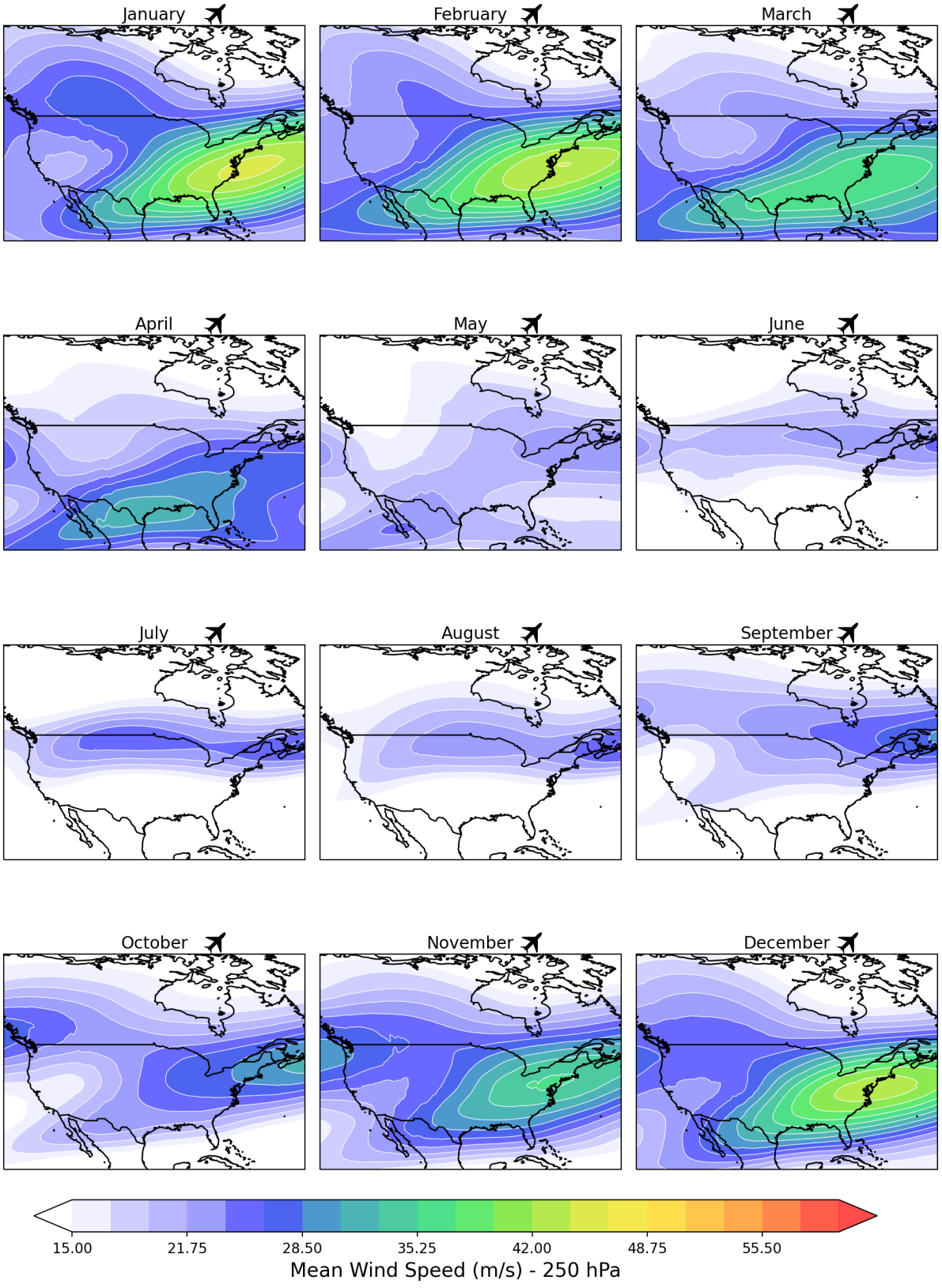

FIGURE 4.2: Mean climatology of the jet stream at 250 hPa from 1980 to 2023. Showing the seasonal changes in wind speed across CONUS for each month.

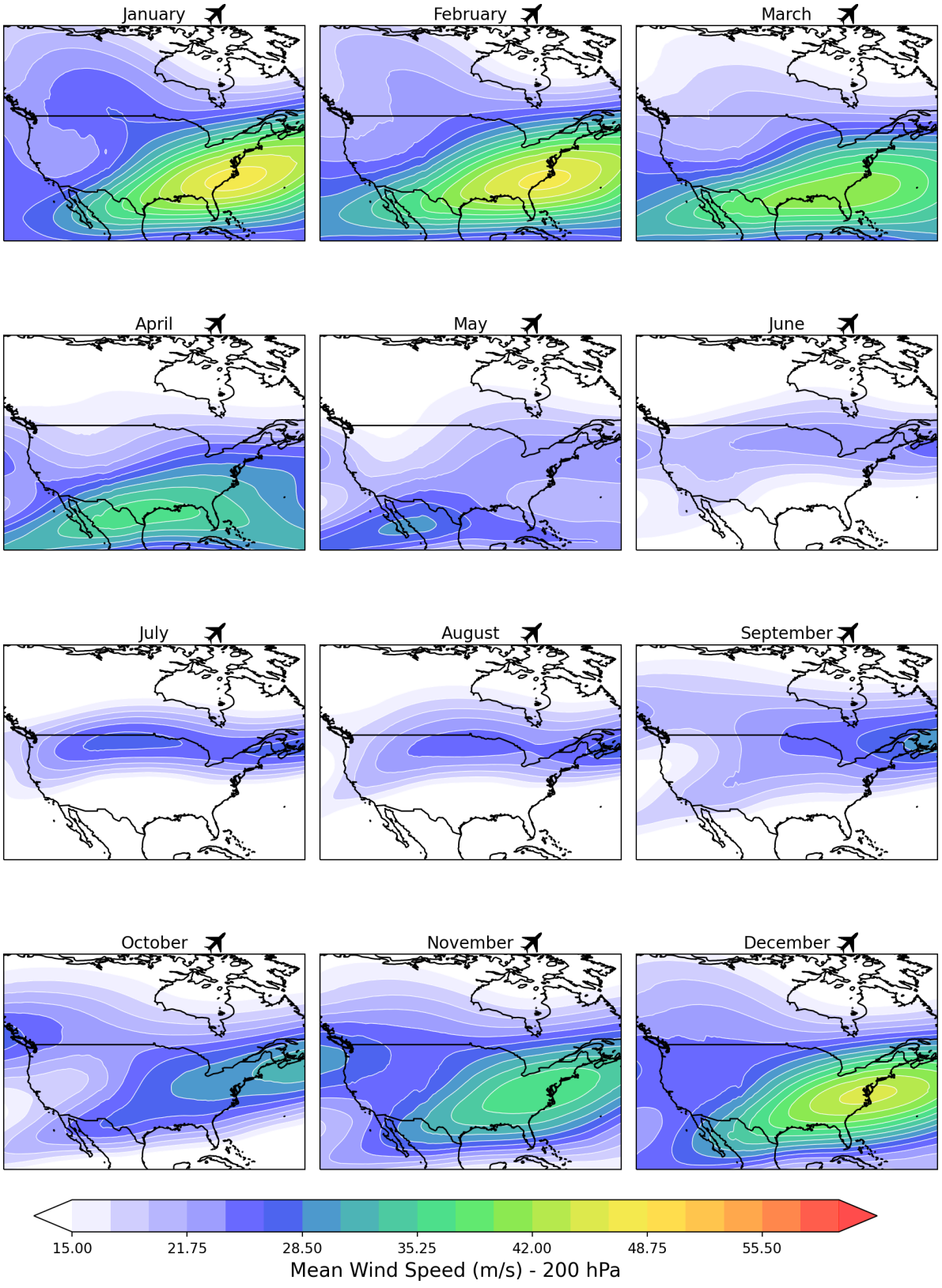

FIGURE 4.3: Mean climatology of the jet stream at 200 hPa from 1980 to 2023. Showing the seasonal changes in wind speed across CONUS for each month.

4.2.2 Vertical Wind Shear (VWS)

Figure 4.4 shows the 43-year climatology of VWS (m/s per 1 km) between 700 and 250 hPa in CONUS. VWS is normally calculated between 700 hPa and 250 hPa, since this range captures important motions between the planetary boundary layer and the tropopause.

The VWS climatology (1980 - 2023) is consistent with the jet stream's seasonal variability (Fig. 4.2 - 4.3). For winter and spring, VWS is stronger with values greater than 0.039 m/s over 1 km (red shading) along the Atlantic, South and East of the U.S. For summer, the jet stream shifts poleward (Fig. 4.2 - 4.3), thus the VWS is stronger over Southern Canada and Northern U.S. During Fall (September-October-November), the jet stream starts to get stronger as it moves over North America, and the VWS gets stronger along the South coast of the U.S.

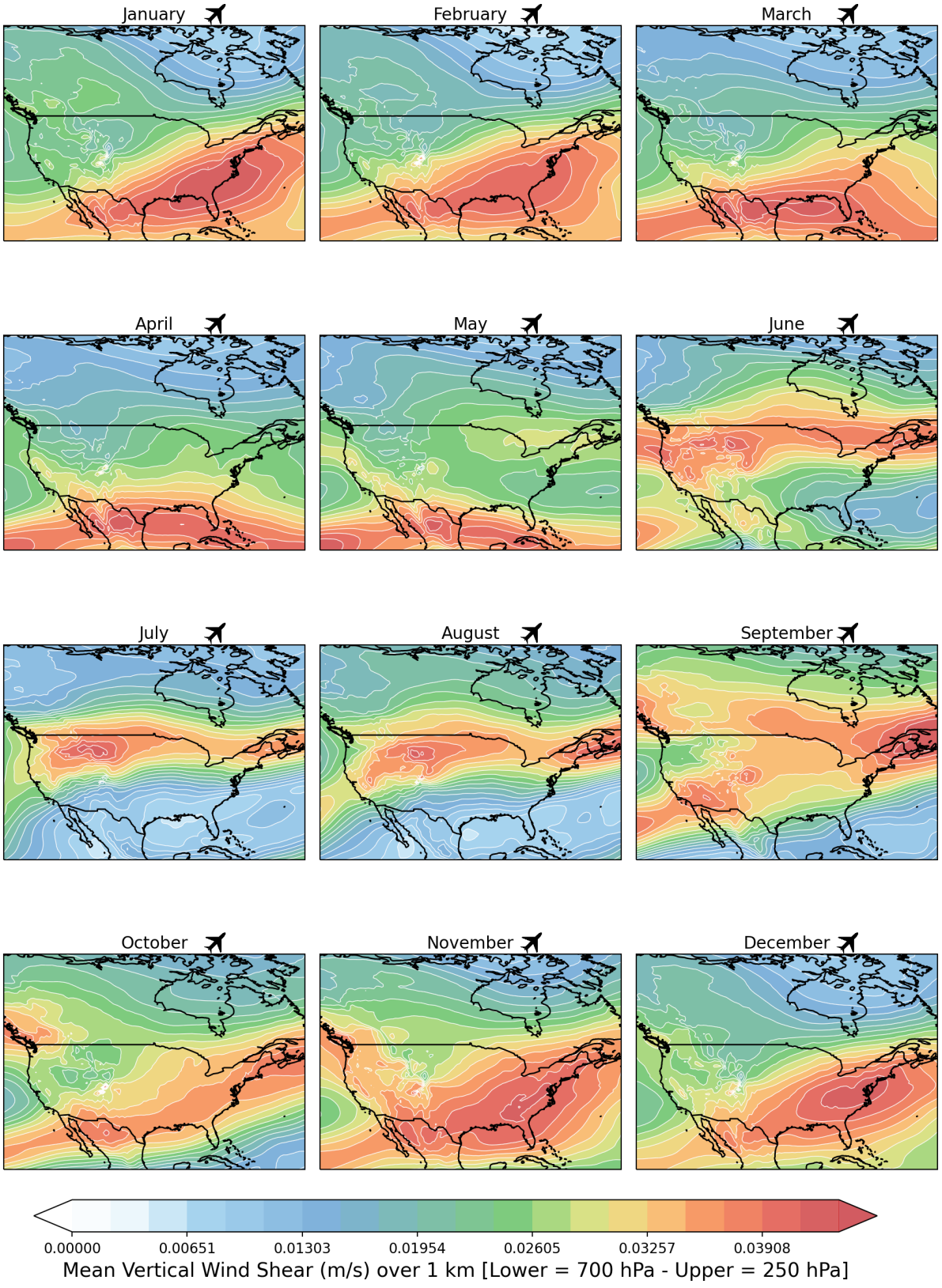

FIGURE 4.4: Mean climatology of the VWS between 700 hPa and 250 hPa from 1980 to 2023. Showing seasonal deviations across CONUS for each month.

4.2.3 Eddy Dissipation Rate (EDR)

Figure 4.5 illustrates the climatology of the EDR between 700 hPa and 250 hPa over CONUS from 1980 to 2023. The EDR climatology coincides with the location of the jet stream (Figs. 4.2 and 4.3) and pronounced VWS (Fig. 4.4). During the winter season, higher values of EDR that are greater than 1.140 x 10^{-17} m^2/s^3 persist over the Atlantic Ocean, South and East of the U.S. During spring, higher EDR (orange-red shaded areas) values persist in the Gulf and North of Mexico. EDR values ranging from 0.684 to 0.912 x 10^{-17} m^2/s^3 (green-yellow shaded areas) persist in the South of the U.S., and lower EDR values (blue-green shaded areas) ranging from 0.228 to 0.456 x 10^{-17} m^2/s^3 across the midlatitudes. During summer, the EDR values migrate north as the jet stream weakens. Higher EDR values persist in the Rockies and lower EDR values across the northern U.S. and southern Canada. During fall, as the jet stream strengthens, the EDR also increases in localized areas. Between September and November, higher EDR values persist over the Northwest, Northeast of the U.S. and North of Mexico.

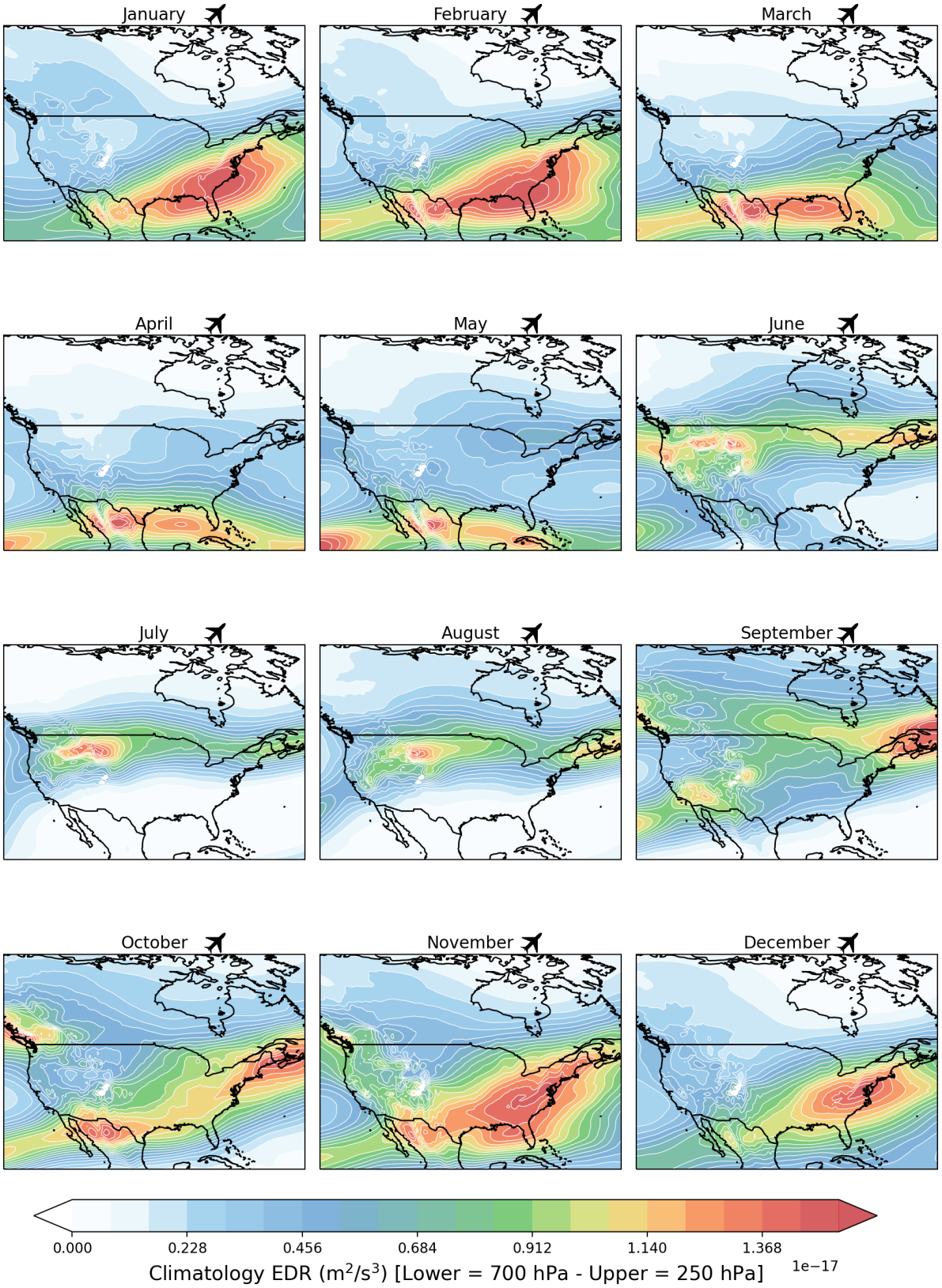

FIGURE 4.5: Mean climatology of the eddy dissipation rate (EDR) between 250 hPa and 200 hPa from 1980 to 2023. Showing seasonal changes across CONUS for each month.

4.2.4 Synoptic-scale vertical motion or Omega (ω)

Figures 4.6 and 4.7 illustrates the climatology of the synoptic-scale vertical motion of air in units of Pascal per seconds (Pa/s). Seasonal changes of ω across CONUS are observed each calendar month between 250 hPa and 200 hPa.

During winter, negative ω (upward motion) persist across the Northeast, Midwest, and Atlantic. A combination of downward motion (positive ω) and upward motion (negative ω) concentrates along the West, specifically along the Rocky Mountains, suggesting mountain waves. Also, positive ω across the Eastern Pacific and West coast of U.S. is indicative of atmospheric rivers. These patterns persist also for spring season over CONUS.

For summer, negative ω is across the central, West of U.S., Atlantic, West and Southeast of Canada, and West of Mexico. While, positive ω persists over the East coast, Southeast, the Northern U.S., Northeast of Mexico, central Canada, and the Eastern Pacific. These regions patches of positive w continues for September and October. However, starting October through November, both the positive ω and negative ω are present over the West of U.S. The cycle begins again at the end of the Fall season where for November, the Midwest and Northeast region of U.S. have negative ω, suggesting mid-latitude weather systems.

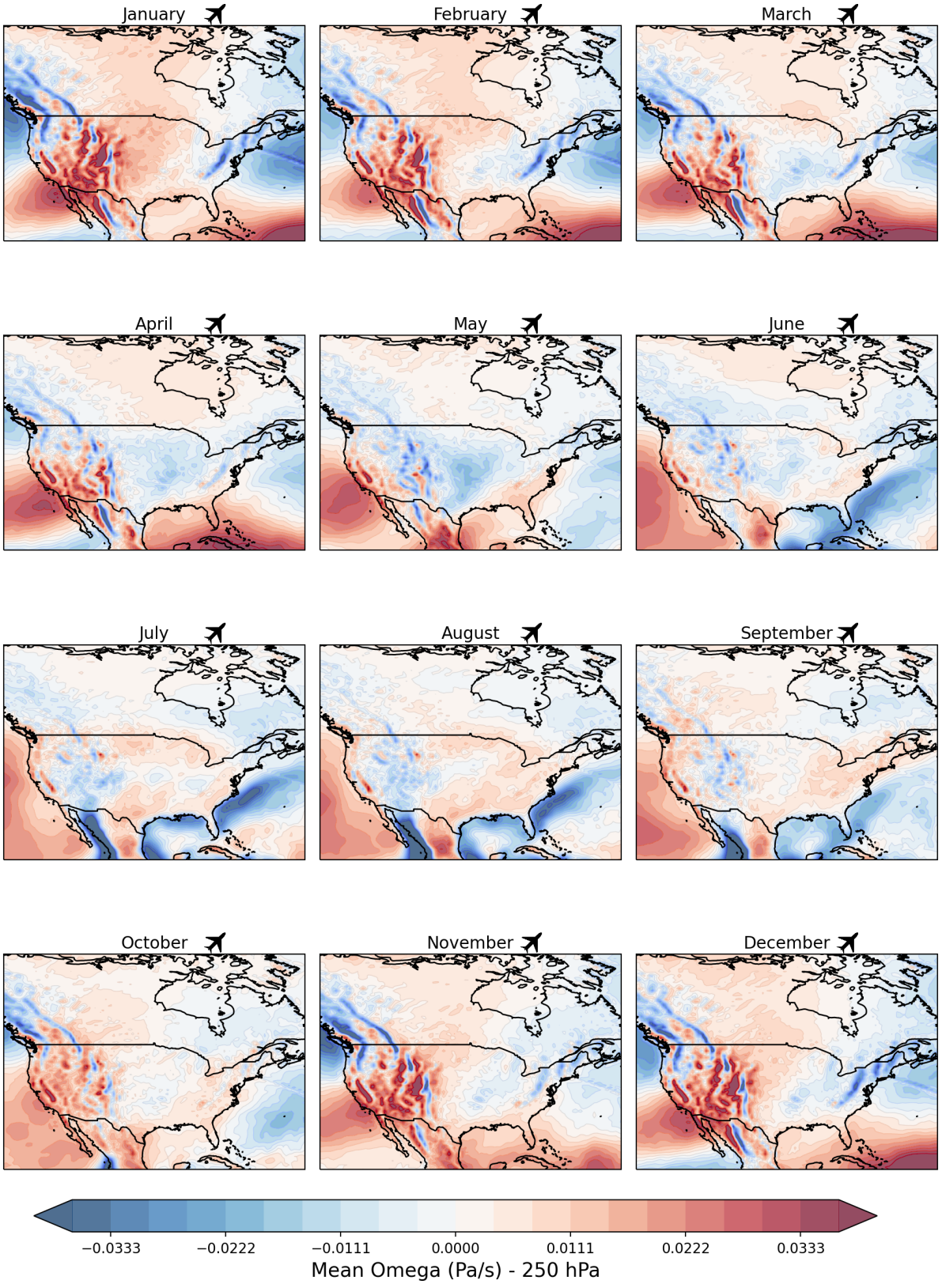

FIGURE 4.6: Mean climatology of the vertical motion of the air (w) at 250 hPa from 1980 to 2023. Showing seasonal changes across CONUS for each month were positive values (red) represents downward motion (subsidence), while negative values indicate upward motion.

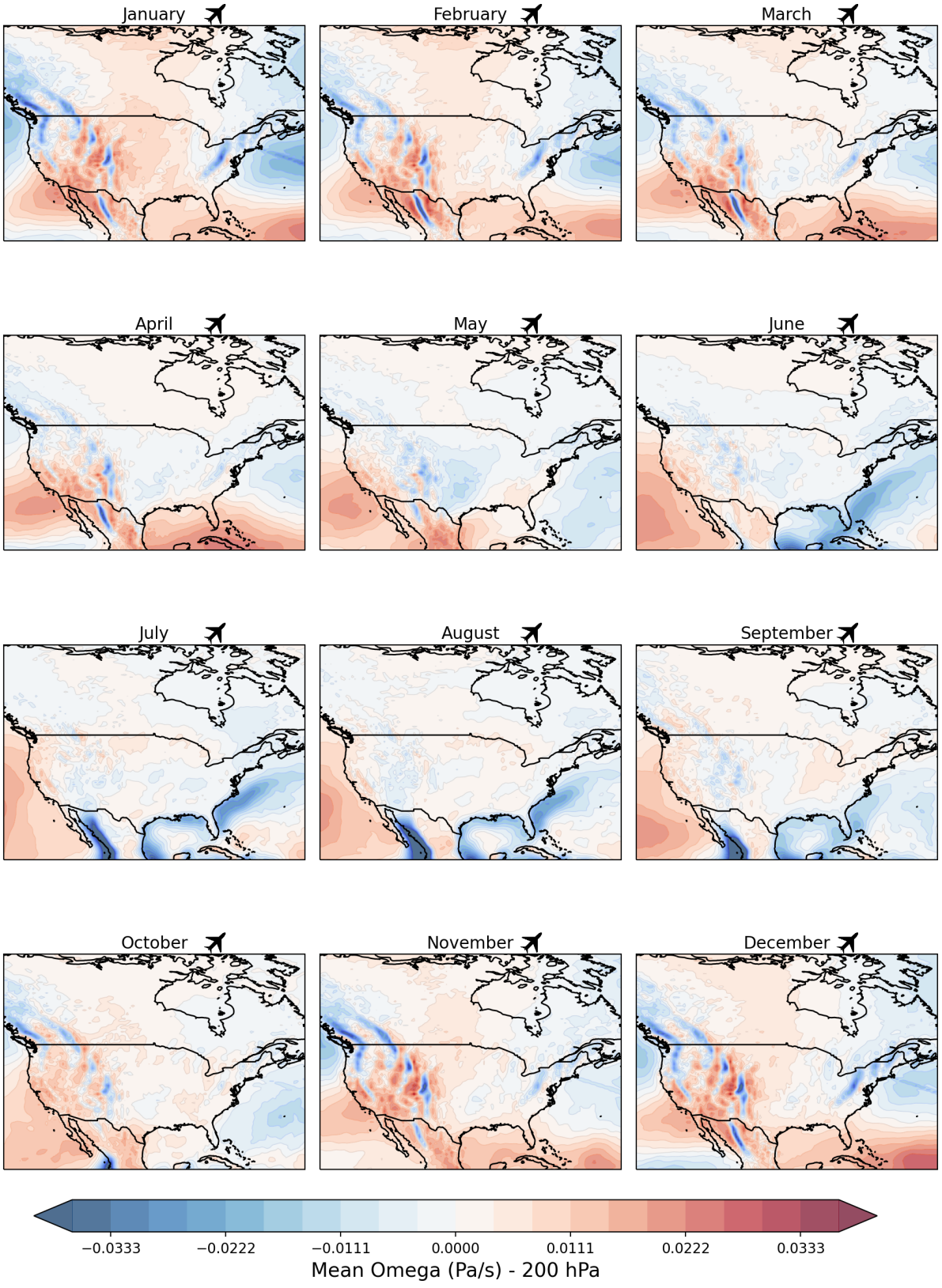

FIGURE 4.7: Mean climatology of the vertical motion of the air (w) at 200 hPa from 1980 to 2023. Showing seasonal changes across CONUS for each month were positive values (red) represents downward motion (subsidence), while negative values indicate upward motion.

4.2.5 Temperature (T)

Figures 4.8 and 4.9 show the climatology from 1980 to 2023 of the mean temperature (°C) between 250 hPa and 200 hPa. The 43-year mean temperature climatology highlights seasonal changes over CONUS. The horizontal temperature gradients at upper levels in the atmosphere contribute to the jet stream's position every season. During winter, colder temperatures (less than -58°C) are reaching the northern U.S. at 250 hPa. Warmer temperatures (greater than -43°C) are reaching over the southern U.S. This pattern continues for spring, where colder temperatures persist along the mid-laitudes and warmer temperatures along the tropics. Hence, the subtropical jet stream is stronger during winter and spring due to the baroclinic structure of the atmosphere. More specifically, strong temperature gradient drives upper-level wind speeds that act as the boundary between cold polar and warm tropical air.

During summer, warmer temperatures greater than -40°C move over North America, and lower temperature values greater than -53°C move over Canada. The boundary between these two air masses aligns with the weakening of the jet stream for June-July-August. For September-October-November, warmer temperatures begin to move along the southern U.S. and colder polar masses of air across the northern U.S and Canada.

In general, changes in seasons are illustrated by the strong horizontal temperature gradient of cold polar air and warm tropical air. This climatology is consistent with the jet stream's position (Fig. 4.2 - 4.3), along the boundaries between cold and warm air or

along the baroclinic zones. This is further supported by Figure 4.9, which illustrates the mean temperature climatology at 200 hPa. The mean temperature decreases with height over CONUS for each calendar month.

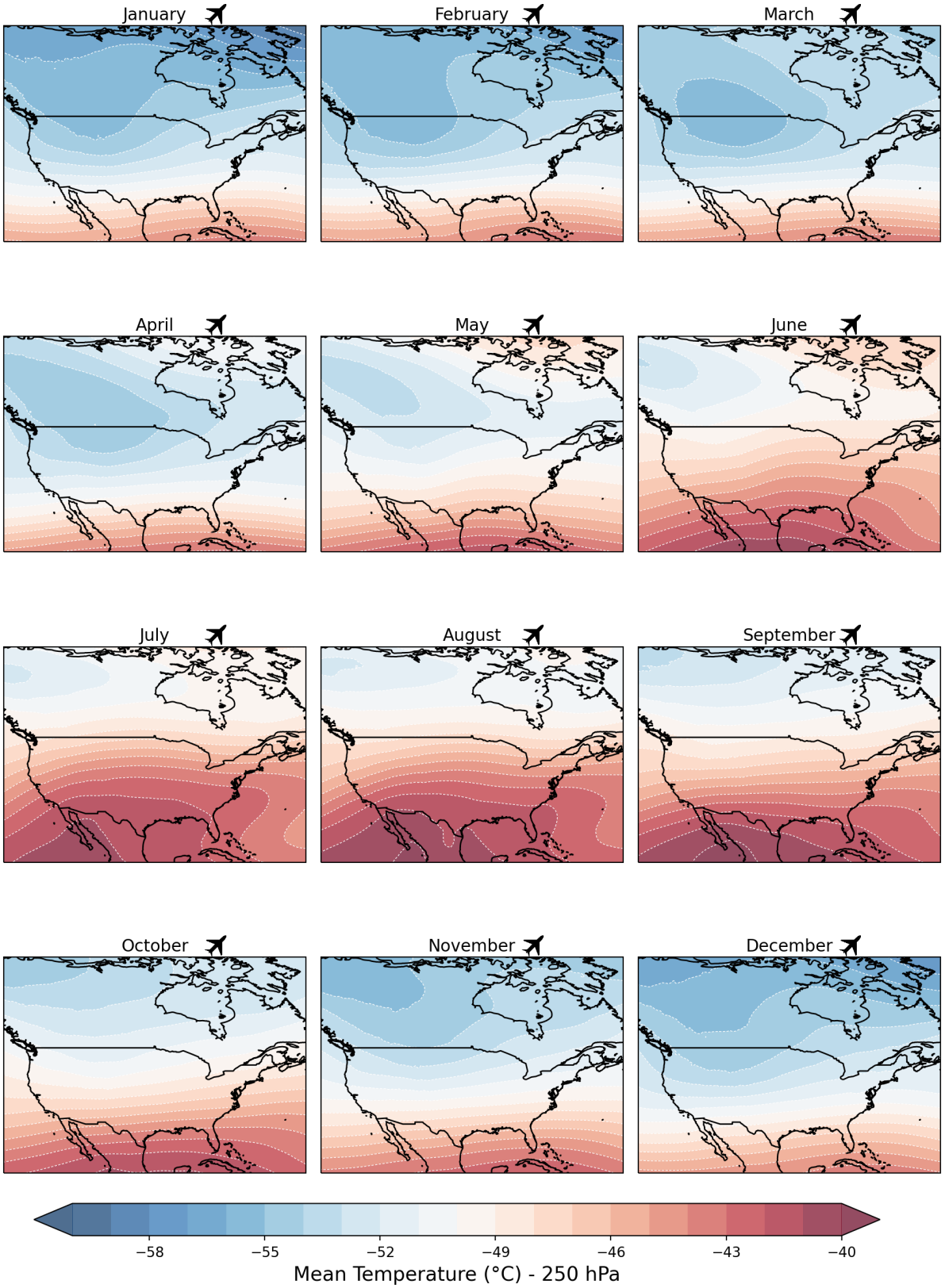

FIGURE 4.8: Mean climatology of the temperature at 250 hPa from 1980 to 2023. Showing seasonal changes across CONUS for each month were positive values (red) represent warmer temperatures, while negative values indicate colder temperatures.

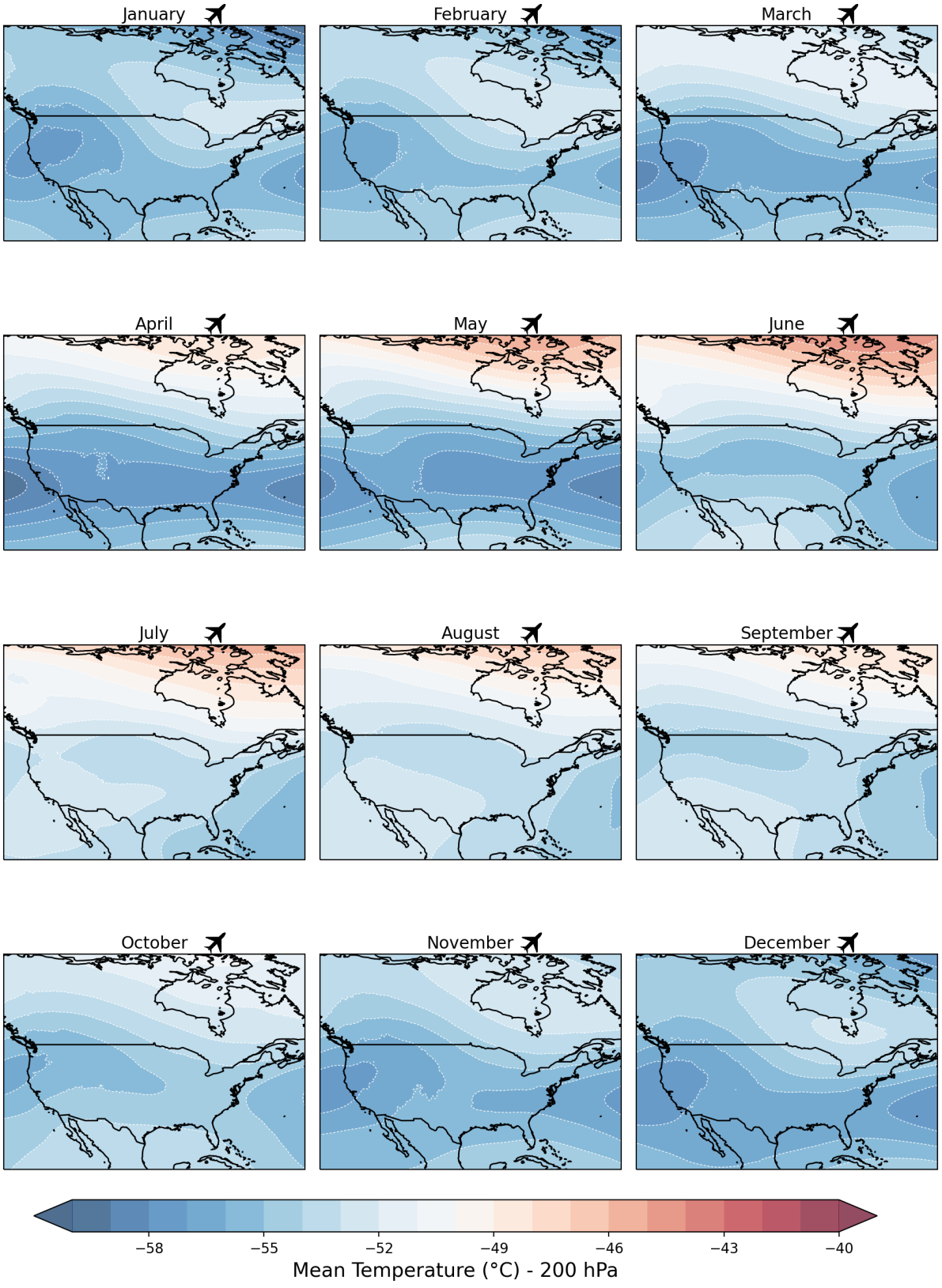

FIGURE 4.9: Mean climatology of the temperature at 200 hPa from 1980 to 2023. Showing seasonal changes across CONUS for each month were positive values (red) represent warmer temperatures, while negative values indicate colder temperatures.

4.2.6 Ertel's Potential Vorticity (EPV)

In this study, the PV is used to identify stratospheric and tropospheric mass exchange. The upward and downward motions are the principal components for the development or weakening of synoptic-scale weather systems. More specifically, the updraft and downdraft from these low-pressure systems play a crucial role in the formation of CAT.

Figures 4.10 and 4.11 illustrates the climatology of the PV in units of $10^{-6}m^2kg^{-1}s^{-1}$ or 1 PVU between 250 hPa to 200 hPa. Higher values of PV persist over north America and south of Canada, while lower values persist over the Mid-latitudes for each calendar month. However, when air masses are near the tropopause will have PV values of 2 PVU, and in the troposphere typically less than 2 PVU, but in the stratosphere typically greater than 2 PVU. The PV values between 1.5 or 2 PVU are considered the location of the dynamic tropopause. The dynamic tropopause changes its location depending on the season.

During winter and onset spring season, the dynamic tropopause is across southern U.S. However, as temperatures begin to warm, the dynamic tropopause moves poleward across the northern U.S for summer and at the beginning of Fall. Mid-fall season, the temperatures starts to get lower or colder, thus dynamic tropopause moves equatorward positioning along the Mid-latitude and southern U.S. The mean position of the dynamic tropopause is consistent with Akritidis et al. (2021). The location of the tropopause is useful in identifying tropopause folds. Tropopause folds are represented by intrusions of

stratospheric air (rich in ozone and dry) in the upper troposphere, capable of creating VWS, which can lead to CAT. More specifically, the close proximity of the jet stream (Figs. 4.2 and 4.3) is associated with regions of pronounced VWS (Fig. 4.4) and regions of horizontal temperature gradients (Figs. 4.8 and 4.9), providing sufficient ingredients to trigger CAT.

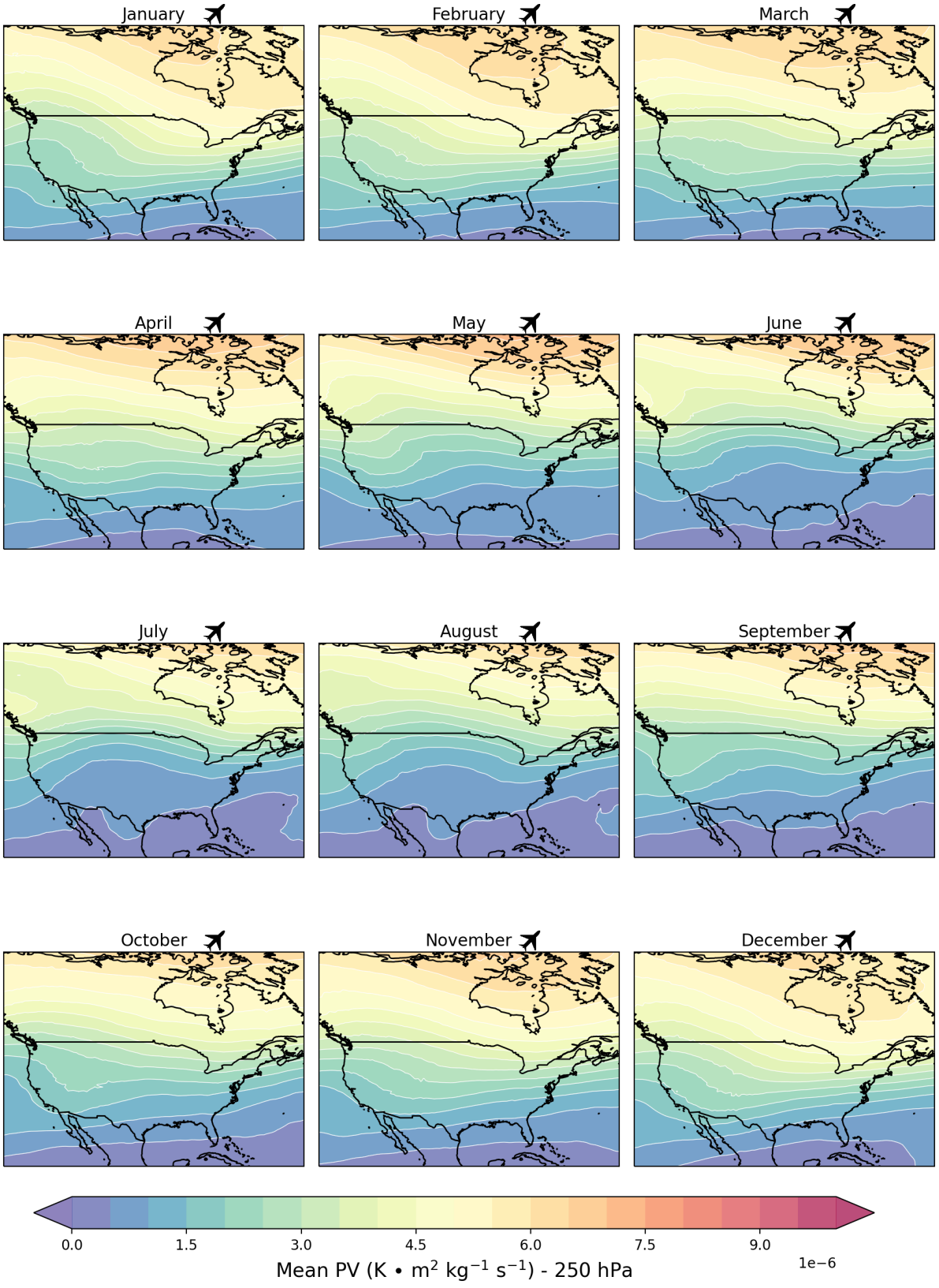

FIGURE 4.10: Mean climatology of the potential vorticity (PV) at 250 hPa from 1980 to 2023. Showing seasonal changes across CONUS for each month.

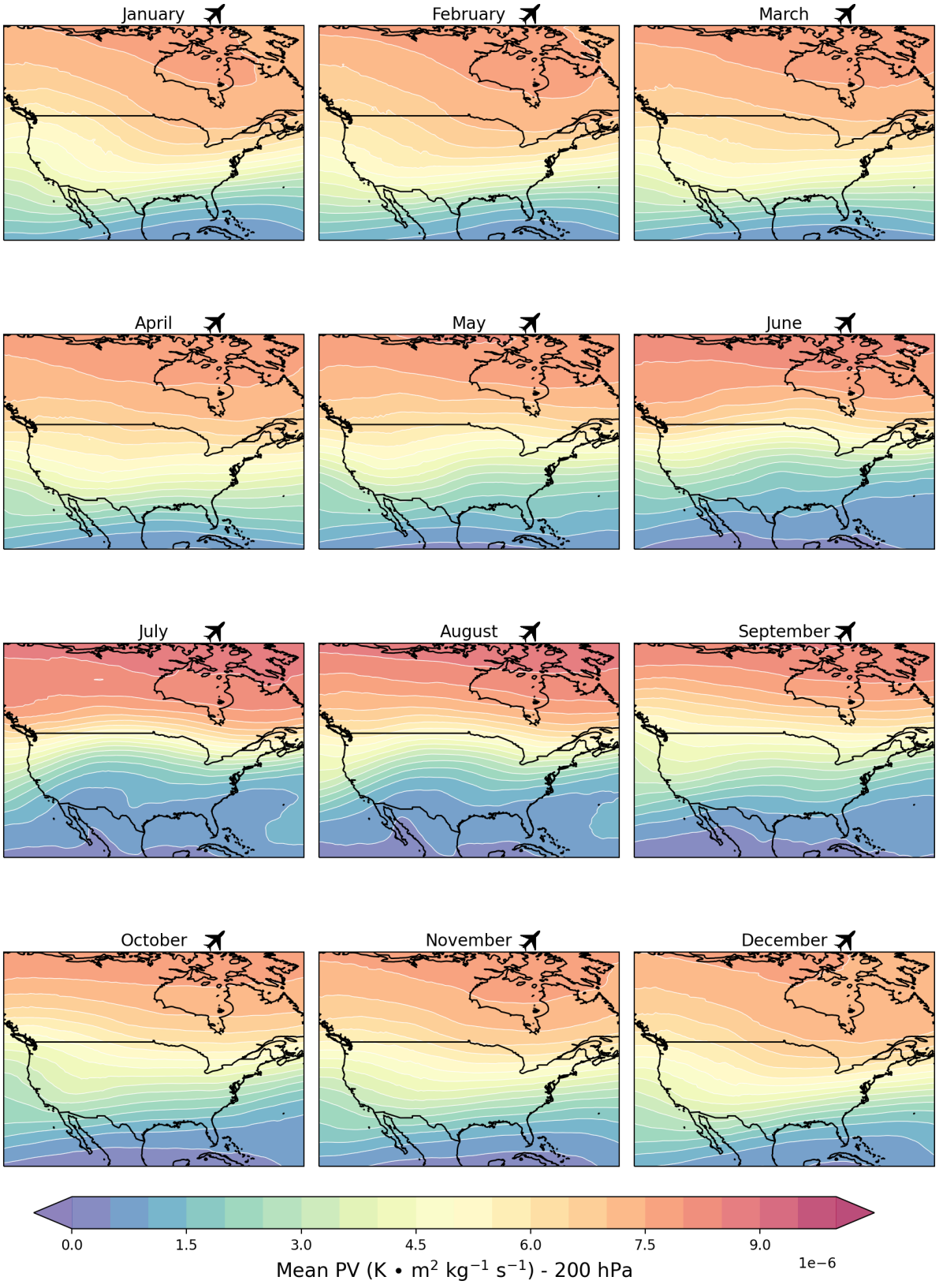

FIGURE 4.11: Mean climatology of the potential vorticity (PV) at 200 hPa from 1980 to 2023. Showing seasonal changes across CONUS for each month.

4.2.7 Specific Humidity (q)

Figures 4.12 and 4.13 illustrates the mean climatology for specific humidity at upper levels between 250 hPa and 200 hPa. Lower values of moisture (green to purple) range between 0 and 1.35 x 10^{-7} g/kg. While higher values of moisture (orange to red) range between 1.80 and 2.70 10^{-7} g/kg.

During winter, lower values of moisture extend across the U.S. and Canada. In this case, lower values of q imply advection of cold and dry air from the poles to the Mid-latitudes. This patron continues until the end of spring season. During summer, moisture increases as warm and moist air is advected from the Gulf of Mexico to the North of Mexico and the South of the U.S. During fall, moisture decreases again as dry air moves across the U.S. For September, higher values of moisture remain along the Gulf of Mexico. In general, dry regions are consistent with higher values of PV (greater than 1.5 PVU) as seen in Figures 4.10 and 4.11, which indicates stratospheric air intrusions. While, higher values of moisture are consistent with lower values of PV, which indicates tropospheric air.

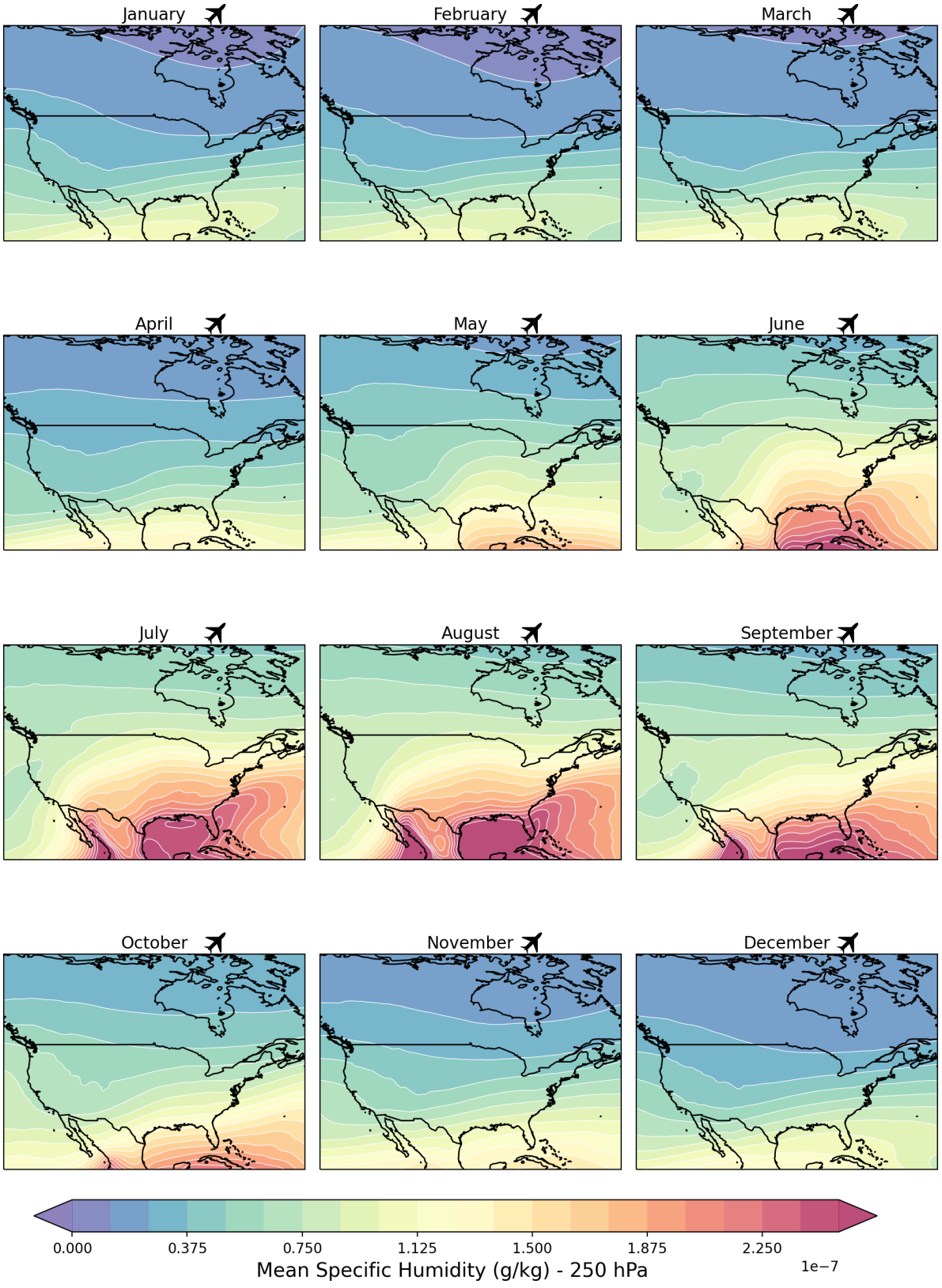

FIGURE 4.12: Mean Climatology of the specific humidity between 250 hPa and 250 hPa from 1980 to 2023. Showing seasonal variations across CONUS for each month.

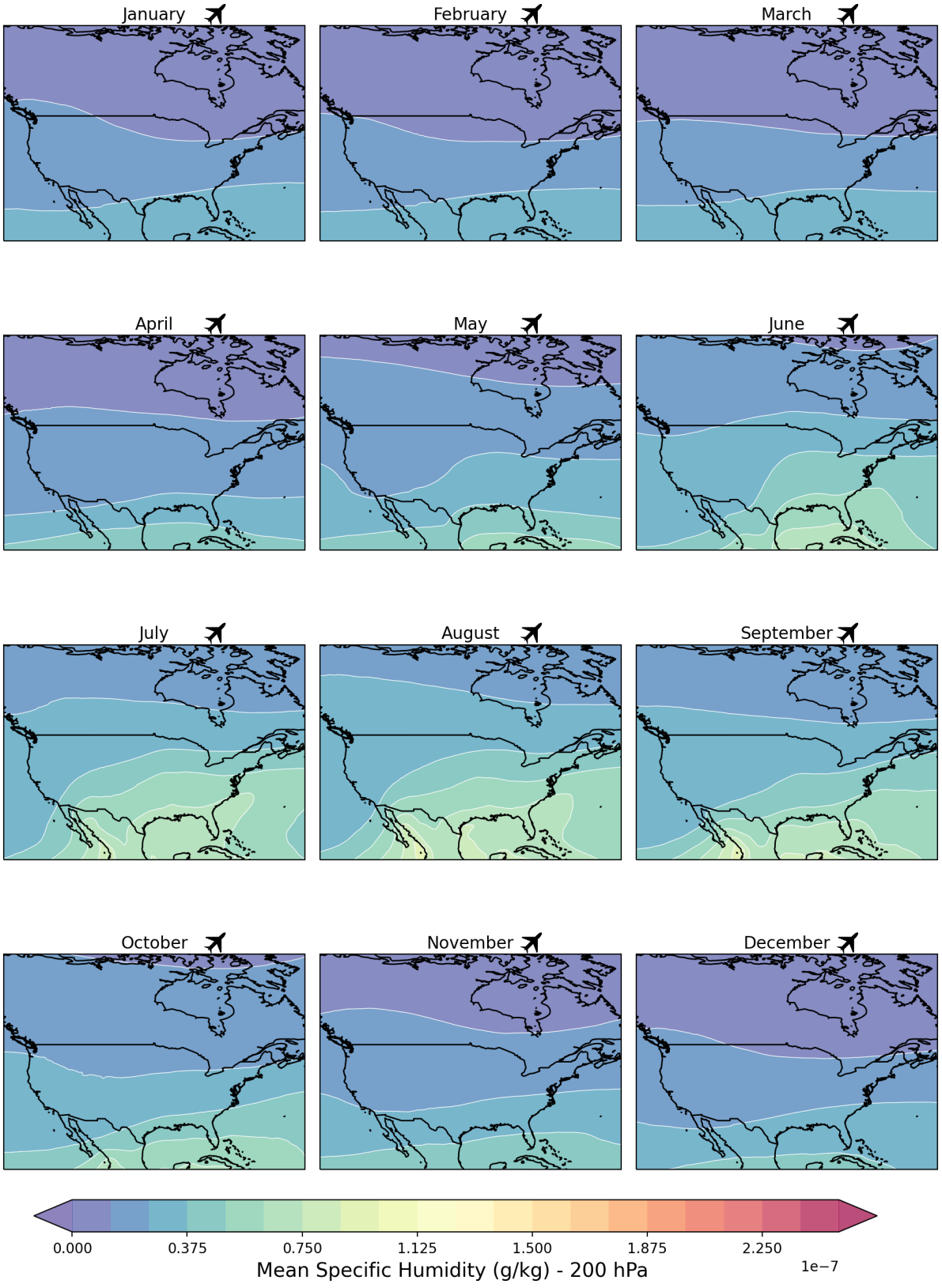

FIGURE 4.13: Mean Climatology of the specific humidity between 250 hPa and 200 hPa from 1980 to 2023. Showing seasonal variations across CONUS for each month.

4.3 Changes in turbulence-relevant parameters over the past decade

As introduced in Section 3.1, changes in parameters relevant to turbulence, such as VWS, EDR, ω, T, PV, and q were calculated by subtracting the difference between the reference years (1980-2013) and the comparison years (2014-2023).

4.3.1 Changes in Upper Level Wind Speeds and VWS

The upper-level wind speeds have evolved over the past decade compared to the 43-year climatology (Figs. 4.2 - 4.3). Figures 4.14 and 4.15, illustrate these deviations, where the areas shaded in red indicate an increase in wind speeds. While gray areas indicate a decrease in wind speeds between 250 hPa and 200 hPa.

At the beginning of the winter season, December shows a weakening of wind speeds (less than 2.4 m/s) across the Atlantic, north of Mexico, south and east coast of U.S. Strong wind speeds between 1.8 m/s and 4 m/s across the eastern Pacific, west and east of U.S. These changes in wind speeds persists until the end of April, suggesting a poleward shift of the jet stream. The most notable changes in February showed that wind speeds are increasing in the northern portions of CONUS by an average of 5 m/s. In general, wind speeds at upper levels are weakening (less than 7.2 m/s) over the southern and intensifying over the northern of U.S and southern Canada. These changes in wind speeds are not uniform across months because of changes in the baroclinicity of the atmosphere.

At the end of the spring season, May shows gradient in wind speeds where the northeast and southeast have wind speeds increasing between 1.8 m/s and 4.8 m/s, while across the northwest and southwest the wind speeds are decreasing between 1.6 m/s and 5.6 m/s This wind gradients are typically due to the transition between spring and summer. This transition between seasons coincides with the weakening of the jet stream as the temperature gradient between the mid-latitudes and the equator weakens.

During June, the winds are decreasing across central North America and over the west of Canada. During summer, there is a notable gradient in wind speed at upper levels in the atmosphere between July and August. Wind speeds increasing over the central North America and decreasing across the northern of U.S and southern Canada.

During the fall, especially between September and October, the wind speeds increase from the northwest to the east of Canada. However, the wind speeds decrease from the south to the east. During November, a strong increase in wind speeds continues across Canada, north-east and south of the U.S., indicating the transition between fall and winter.

These changes in mean wind speed, either increasing or decreasing, can represent changes in the jet stream position. The increase/decrease in mean wind speeds can change VWS at upper levels where turbulence risk areas are found. Figure 4.16 illustrates the changes in VWS between 700 hPa and 250 hPa. The regions of increased VWS coincide with regions of increased changes in wind speeds (Figs. 4.14 and 4.15). Additionally, regions of decreased VWS coincide with regions of decreased changes in wind speeds (Figs. 4.14 and 4.15).

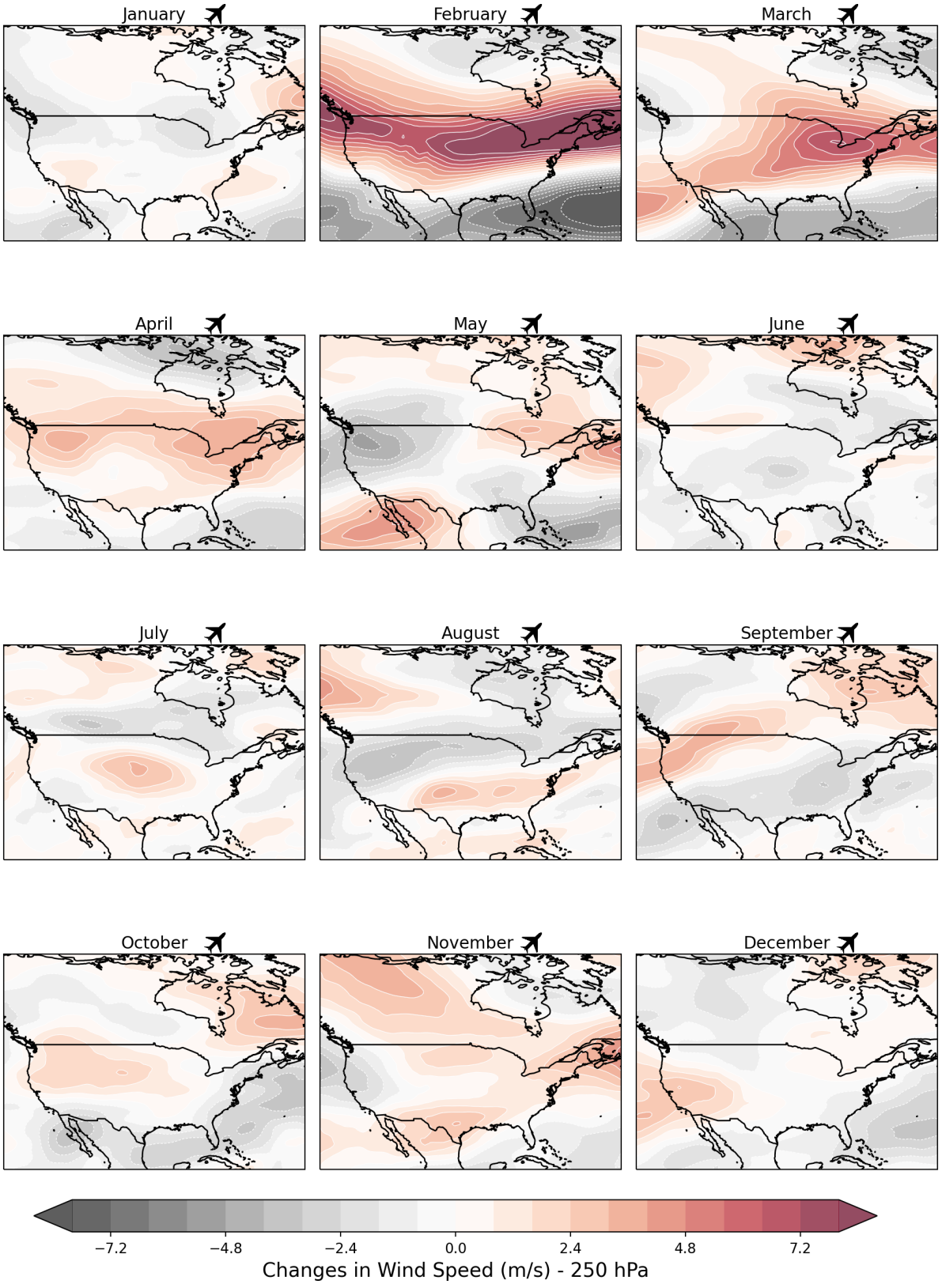

FIGURE 4.14: Changes in mean wind speed of the jet stream at 250 hPa between the comparison period (2014-2023) and reference period (1980-2013), illustrating seasonal variations across North America. Positive values (red) indicate an increase in wind speed over the last decade, while negative values (gray) indicate a decrease in wind speed over the last decade for each calendar month.

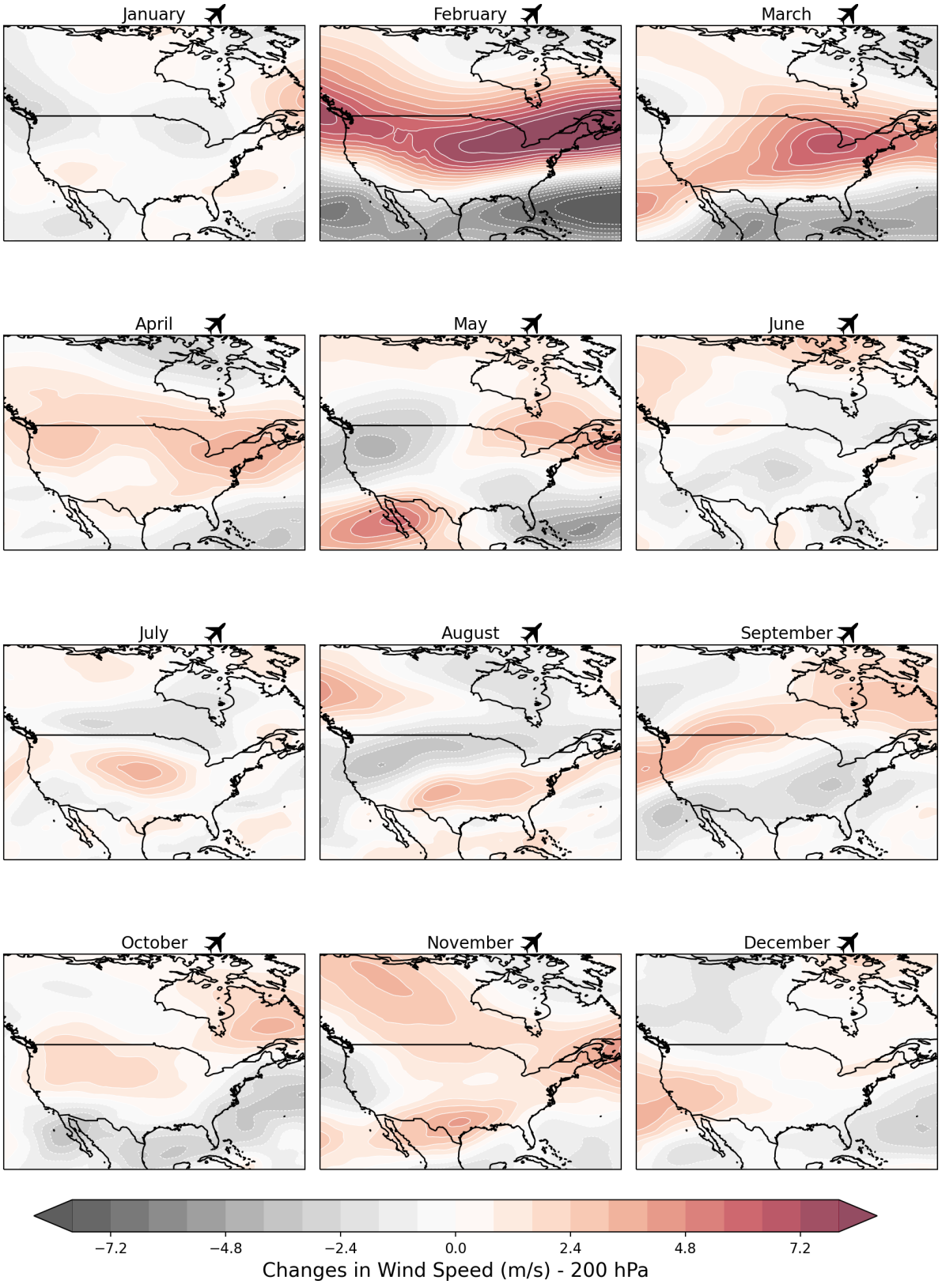

FIGURE 4.15: Changes in mean wind speed of the jet stream at 200 hPa between the comparison period (2014-2023) and reference period (1980-2013), illustrating seasonal variations across CONUS. Positive values (red) indicate an increase in wind speed over the last decade, while negative values (gray) indicate a decrease in wind speed over the last decade for each calendar month.

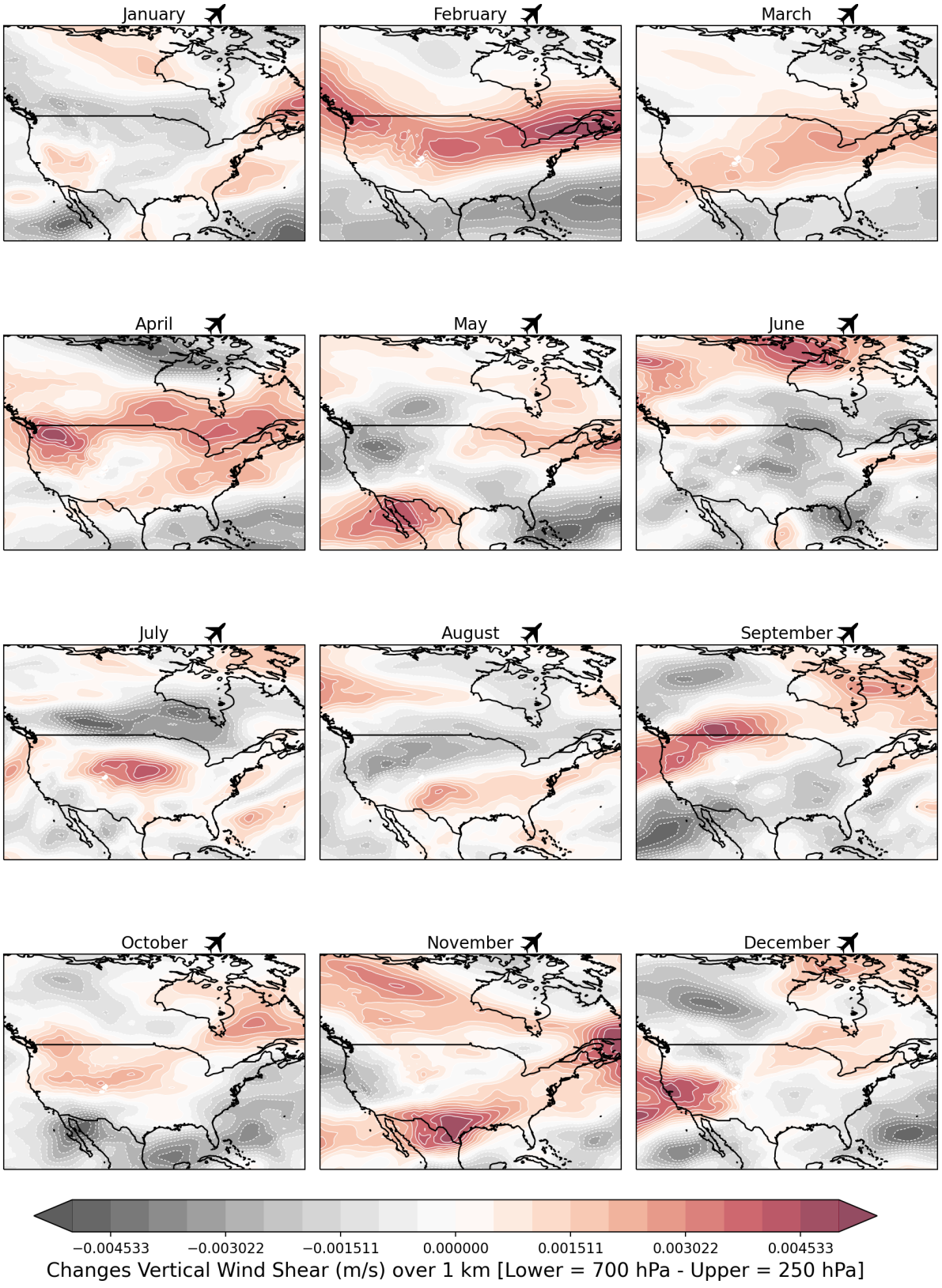

FIGURE 4.16: Mean changes of the VWS between the comparison period (2014-2023) and reference period (1980-2013) from 700 hPa and 250 hPa, showing seasonal deviations across CONUS for each month. The positive values (red) indicate increase VWS, while negative values (gray) show regions of VWS decrease for the last decade.

4.3.2 Changes in EDR

Figures 4.17 illustrate the changes in EDR, where the areas shaded in red indicate an increase in EDR, while the blue areas indicate a decrease in EDR between 700 hPa and 250 hPa.

During February, March and April, EDR values are higher, indicating an increase in turbulence intensity across the U.S. EDR values are lower in the Atlantic, Southeast coast of U.S., Eastern Pacific, the Gulf and North of Mexico, indicating a decrease in turbulence intensity. For May, turbulence intensity increases across the Eastern Pacific, North of Mexico, and Northeast of the U.S. During Summer, more specifically July and August, more intense turbulence occurs across the weakening of the jet stream. The weakening of the jet stream extends from Southern Canada and Northern U.S.

During September, turbulence intensity increases across southern Canada and Northwest of U.S. For October, EDR increases across the West, South, Central and Northern of U.S. Lastly, for November, turbulence intensity increases along the Eastern Pacific, Northeast, South of the U.S., and North of Mexico. The EDR increases across these regions are consistent with the strengthening of the subtropical jet stream before the start of the winter season. In general, regions of increased EDR can be associated with areas of increased VWS. Regions of increased VWS have more intense turbulence that are potentially hazardous to aircraft.

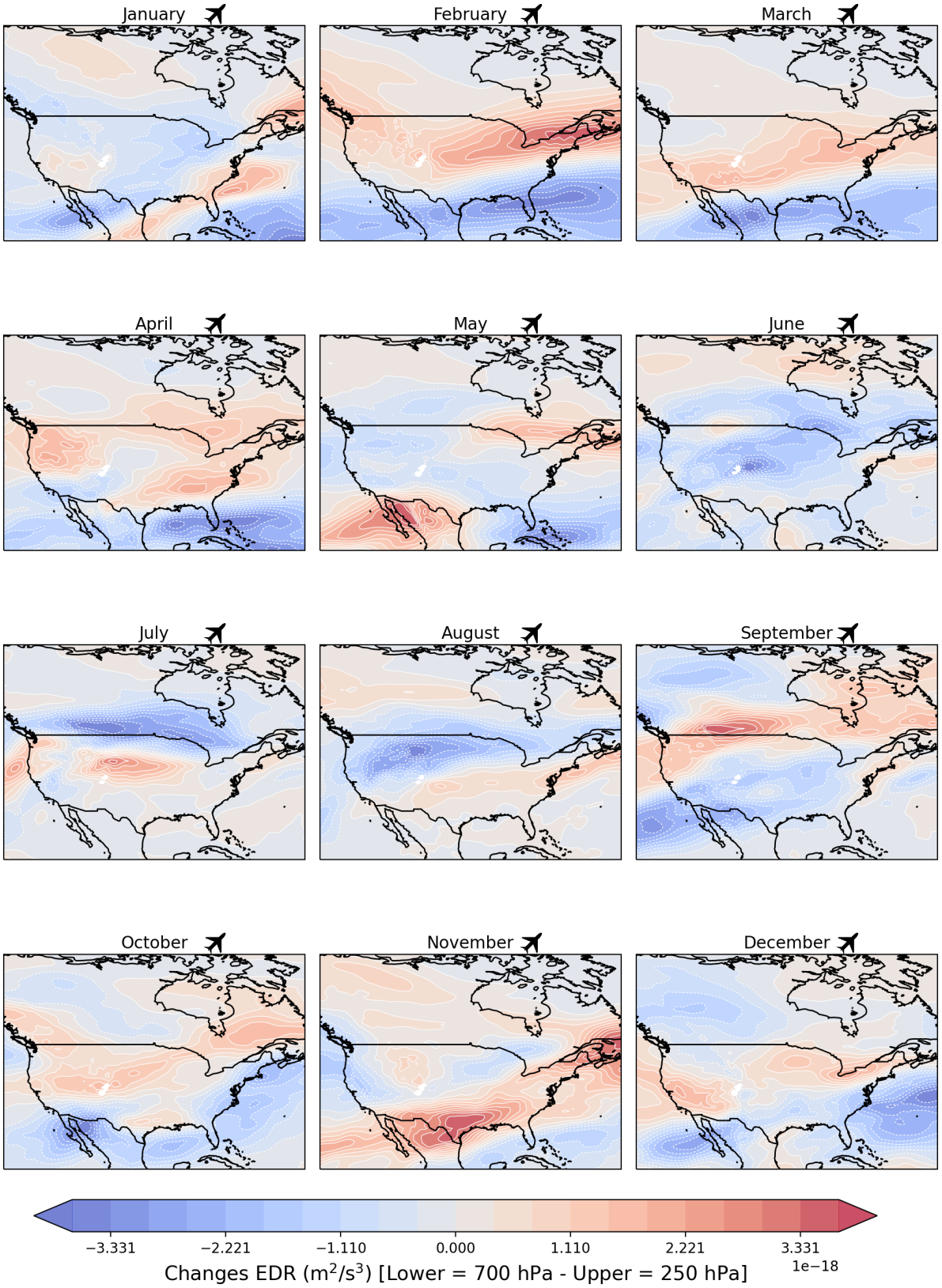

FIGURE 4.17: Changes in mean EDR values between the comparison period (2014-2023) and reference period (1980-2013) from 700 hPa and 250 hPa, showing seasonal deviations across CONUS for each month. Positive values (red) indicate an increase in turbulence intensity, while negative values (blue) represent a decrease in turbulence intensity for the last decade.

4.3.3 Changes in Synoptic-scale vertical motions or Omega (ω)

Figures 4.18 and 4.19 represent the changes in the mean absolute value of ω, denoted as $|\omega|$, showing both upward and downward motion over the last decade between 250 hPa and 200 hPa. These changes were calculated by the difference between reference years (1980-2013) and comparison years (2014-2023). The red areas indicate an increase in $|\omega|$, while the blue areas represent a decrease in $|\omega|$.

During winter, the magnitude of the $|\omega|$ increases across the Northeast, Midwest, and along the Rocky Mountains. Figures 4.20 and 4.21, illustrate monthly changes in ω at critical flight levels. Positive values (red) indicate stronger downward motion (subsidence, negative ω), while negative values (blue) represent stronger upward motion (ascent, positive ω). Hence, regions where the magnitude of the $|\omega|$ is increasing will result in stronger upward motion associated with mid-latitude weather systems. As shown in Figure 1.1, it is crucial to remember that one of the mechanisms that causes CAT is the ascent and descent from low-pressure systems. As a result, the Northeast and the Midwest were CAT hotspots are concentrated (Fig. 4.1) due to the ascent and descent from mid-latitude weather systems. Along the Rocky Mountains, an increase in the magnitude of $|\omega|$ (Figs. 4.18 and 4.19) is observed, indicating stronger and persistent subsidence and ascent motions (Figs. 4.20 and 4.21). This interaction can generate gravity waves that propagate vertically until they reach a critical amplitude, at which point the waves break. The breaking of these gravity waves produces wind shear and localized instability, which enhance the occurrence of CAT (Fig. 2.5).

During March, the magnitude of $|\omega|$ (Figs. 4.18 and 4.19) increases from the Southeast coast of the U.S. to the Atlantic. Also, the magnitude of $|\omega|$ increases over the Central, Northeast of the U.S, and Central, Northern Canada. Figures 4.20 and 4.21 illustrate strong upward motion indicative of widespread cloudiness along these regions. Between April and May, greater changes in the magnitude of $|\omega|$ are observed over the Central, Northeast and Southeast of the U.S. These changes correspond to stronger ascent (Figs. 4.20 and 4.21) along the Central (for May), Southeast, and Northeast (for April) of the U.S.

For summer, the magnitude of $|\omega|$ increases over the Southwest, central plains, and localized areas in the Southeastern U.S (Figs. 4.18 and 4.19). Figures 4.20 and 4.21 illustrate a gradient between ascent and descent motions in the North of Mexico. This upward and downward motion is consistent with the mountains in that region. Other localized areas, such as the Southwest (for July), Southeast (for June and August) show intense ascent, while strong subsidence occurs in the North (for July) and Central of the U.S. (for June and August).

For Fall, the magnitude of $|\omega|$ increases across CONUS (Figs. 4.18 and 4.19) between 250 hPa and 200 hPa. The increases in $|\omega|$ correspond to regions of strong ascent and descent (Figs. 4.20 and 4.21) over localized areas. Between September and October, strong ascent occurs across the Northeast and Northwest of the U.S., while subsidence intensifies across the Rocky Mountains and Southeast U.S. For November, subsidence intensifies across the Midwest and Northeast of U.S., while a combination of ascent and descent occurs across

the Rocky Mountains. In general, the increases in magnitude of $|\omega|$ occur across CONUS and indicate more pronounced regions of upward and downward air movement that may interact with the jet stream to produce CAT.

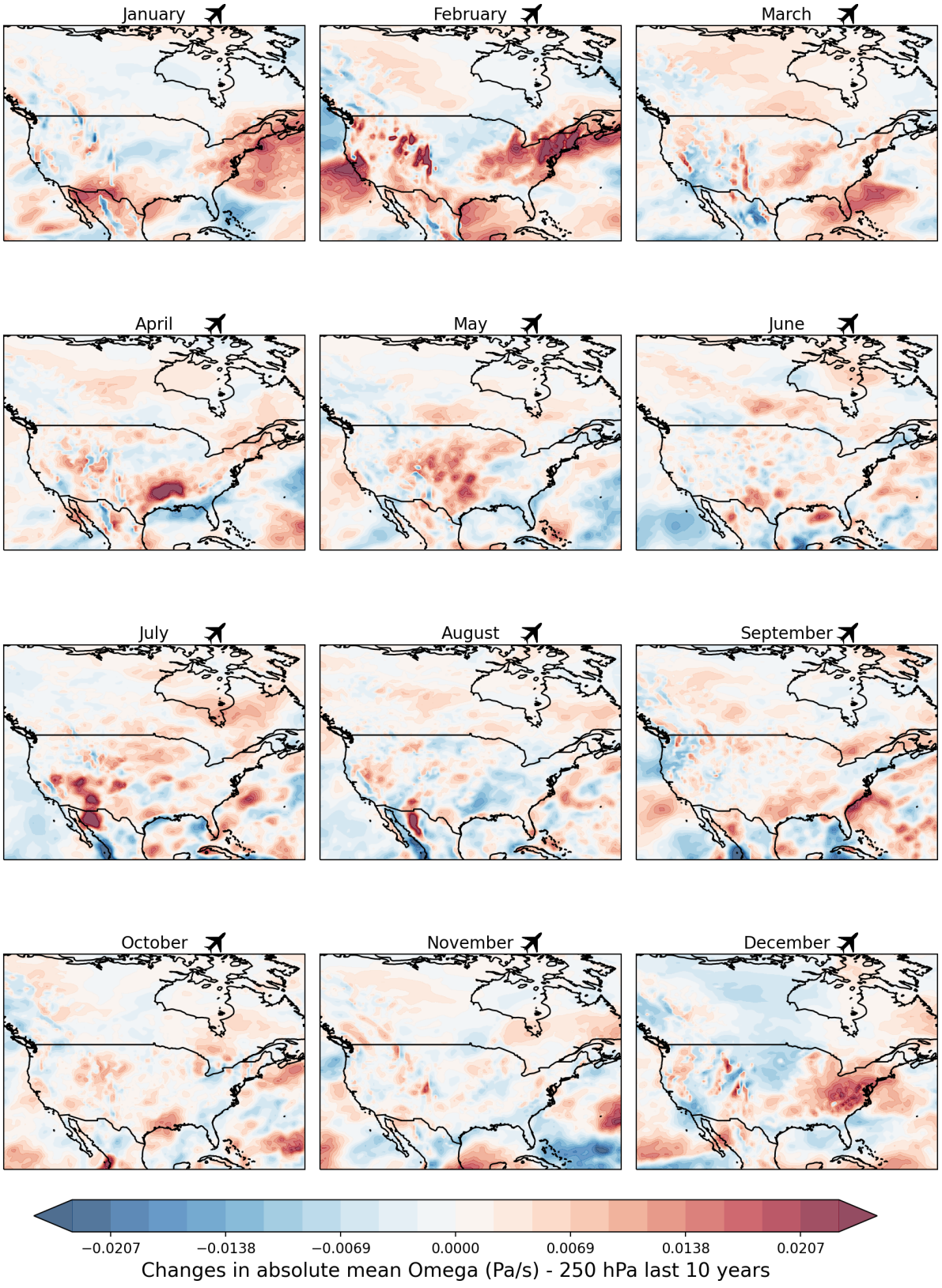

FIGURE 4.18: Changes in the mean magnitude of $|\omega|$ at 250 hPa between the comparison period (2014-2023) and reference period (1980-2013), showing seasonal deviations across CONUS for each month. Positive values (red) indicate an increase in the vertical motion, including both ascent and subsidence, while negative values (blue) indicate a decrease in the vertical motion for the last decade.

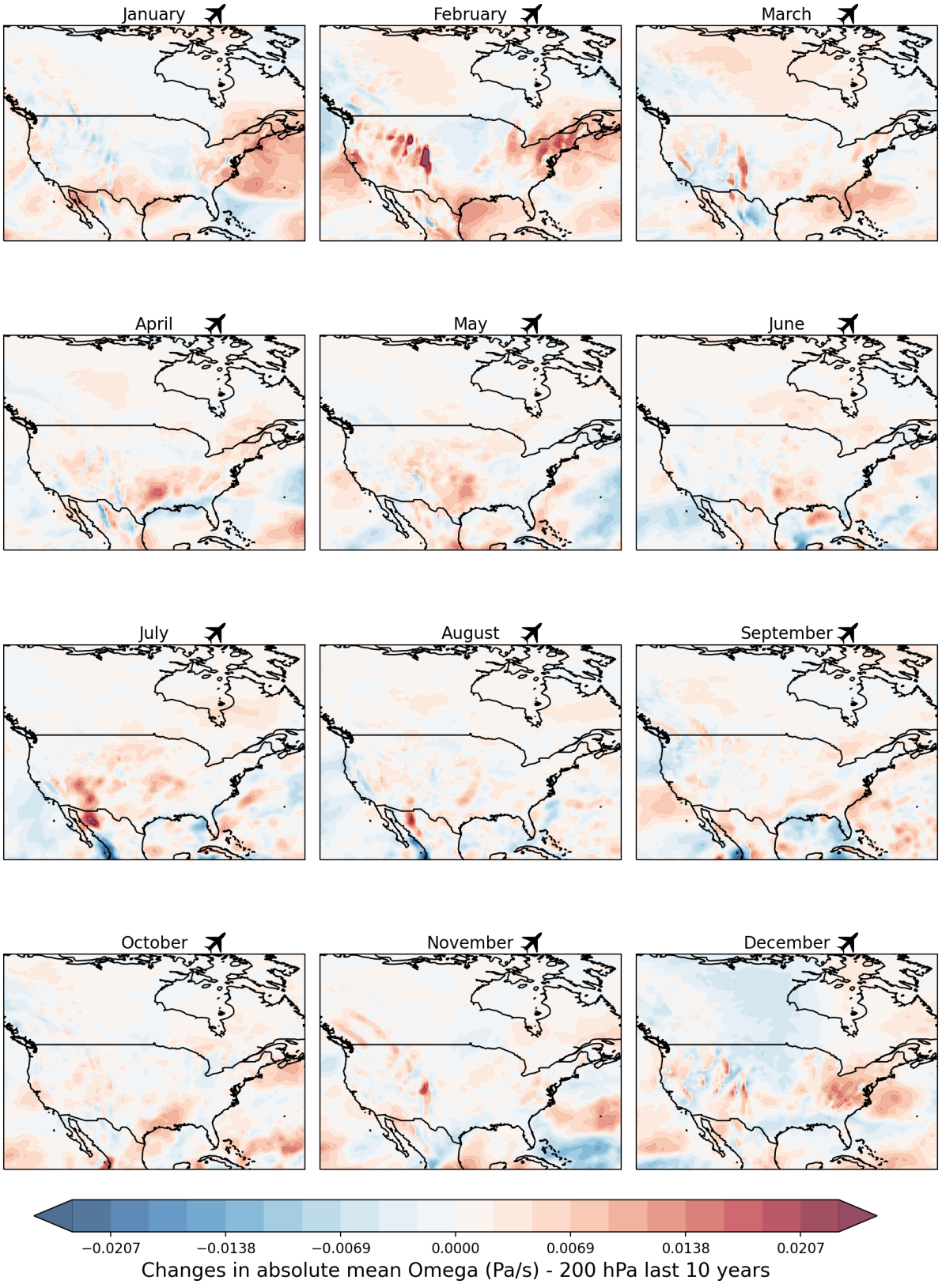

FIGURE 4.19: Changes in the mean magnitude of $|\omega|$ at 200 hPa between the comparison period (2014-2023) and reference period (1980-2013), showing seasonal deviations across CONUS for each month. Positive values (red) indicate an increase in the vertical motion, including both ascent and subsidence, while negative values (blue) indicate a decrease in the vertical motion for the last decade.

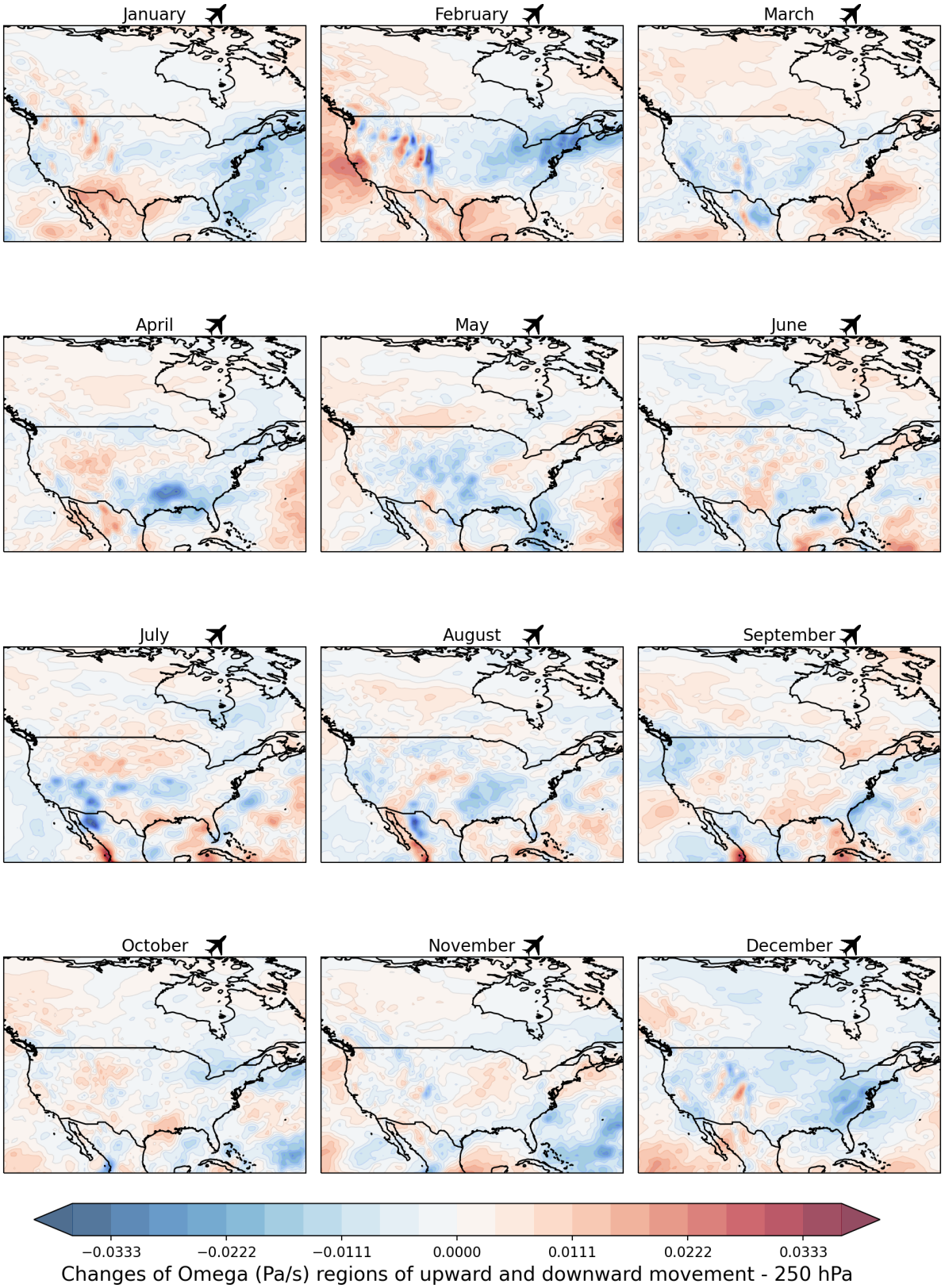

FIGURE 4.20: Changes in the mean ω at 250 hPa between the comparison period (2014-2023) and reference period (1980-2013), showing deviations in the upward and downward components of the vertical motion. Positive values (red) indicate an increase in ascent, while negative values (blue) indicate a decrease in subsidence for the last decade.

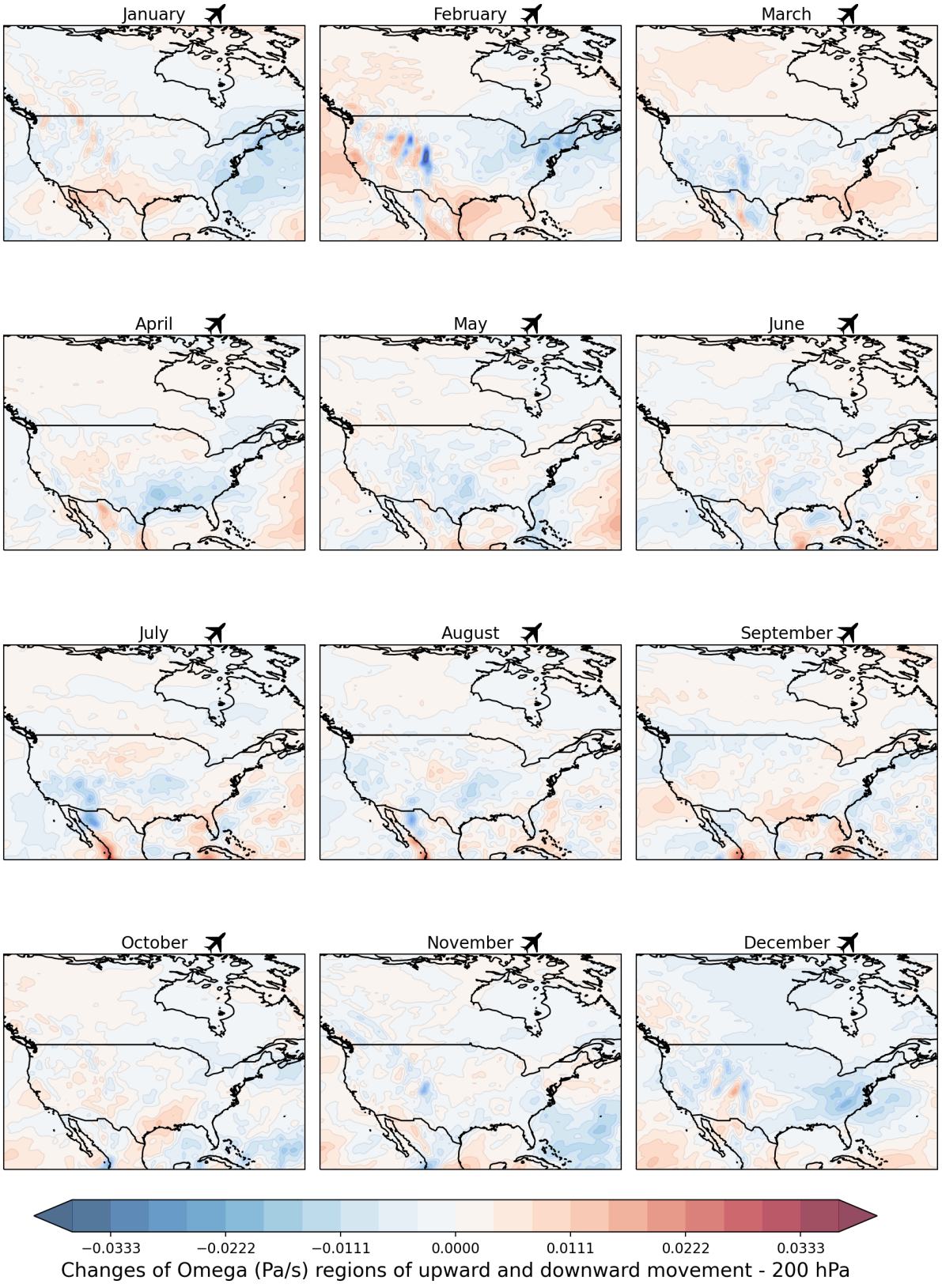

FIGURE 4.21: Changes in the mean ω at 200 hPa between the comparison period (2014-2023) and reference period (1980-2013), showing deviations in the upward and downward components of the vertical motion. Positive values (red) indicate an increase in ascent, while negative values (blue) indicate a decrease in subsidence for the last decade.

4.3.4 Changes in Temperature

The temperature shows changes at upper levels in the atmosphere, 250 hPa and 200 hPa, for the last decade (2014-2023) relative to the last three decades across CONUS. Figure 4.22 shows a strong warming trend for each calendar month, with increases exceeding 1.5°C in some regions. Particularly during February and October, there are notable changes in the atmosphere's baroclinicity. For instance, this warming trend at 250 hPa weakens the temperature gradient that drives the jet stream wind speeds; thus, jet stream dynamics have undergone some changes over the last decade. The warming trend is also spreading over localized regions at 200 hPa (Fig. 4.23).

During February, at 200 hPa, the atmosphere has warm anomalies across North America, South of Canada, and the Gulf of Mexico, while cold anomalies extend from the Atlantic to the Northeast of U.S., and North of Canada. This will result in a strong temperature gradient, enhancing the strength and a poleward shift of the jet stream over the Mid-latitudes. For March, the temperature gradient persists but is not as intense as in February.

At the beginning of summer, warmer anomalies cover the Mid-latitude , weakening the temperature gradient. Thus, the jet stream gets weaker as it propagates poleward. The position of the jet is highlighted by the gradient between warm and cold anomalies across CONUS. Many studies have shown that these warming trends are largely attributed to

the radiative effects of increasing greenhouse gases (Belmecheri et al. (2017) and Williams and Joshi (2016)).

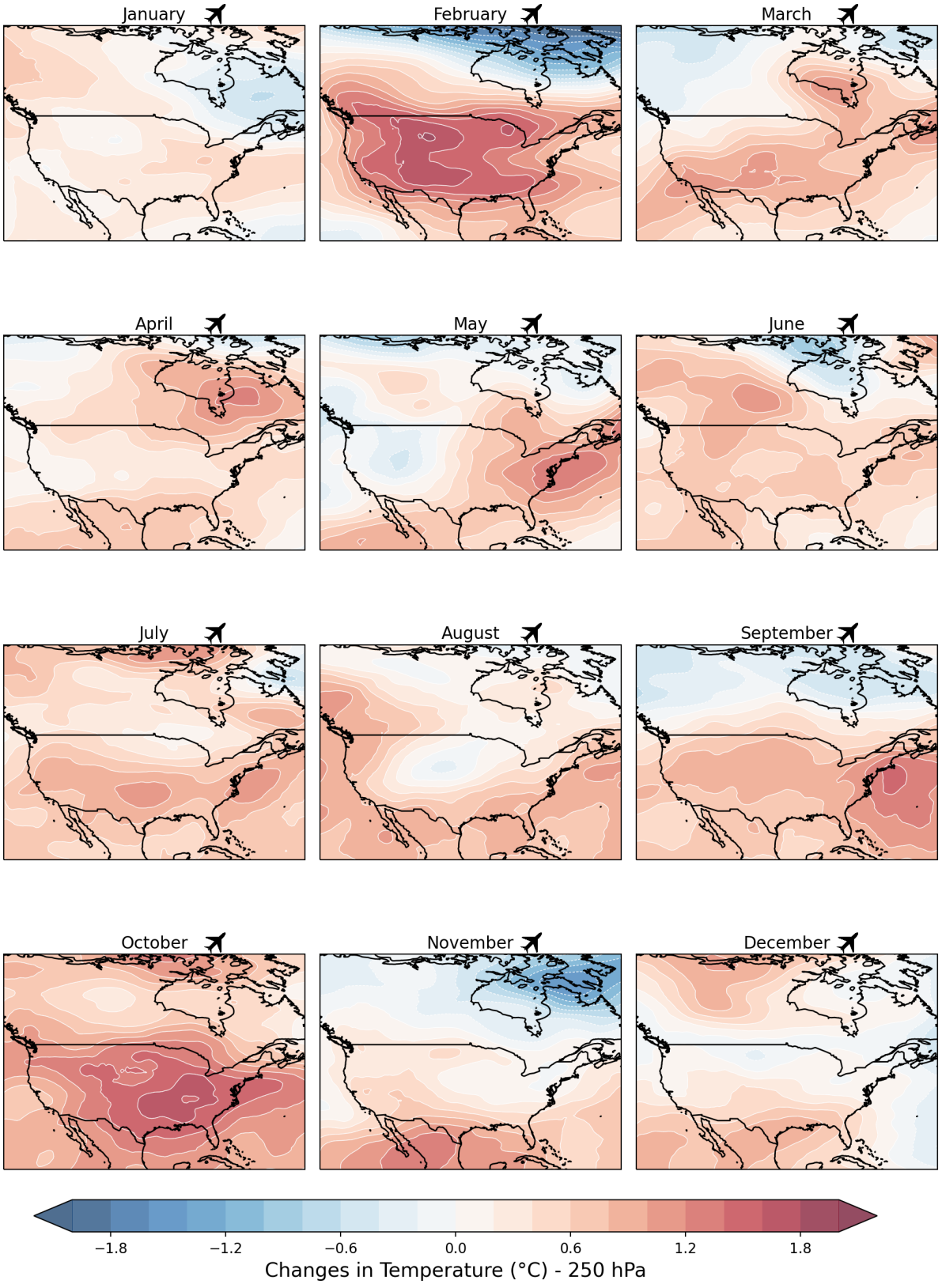

FIGURE 4.22: Mean changes of the temperature at 250 hPa for the last decade (2014-2023). Showing seasonal deviations across CONUS for each month were positive values (red) represent warmer temperatures, while negative values indicate colder temperatures.

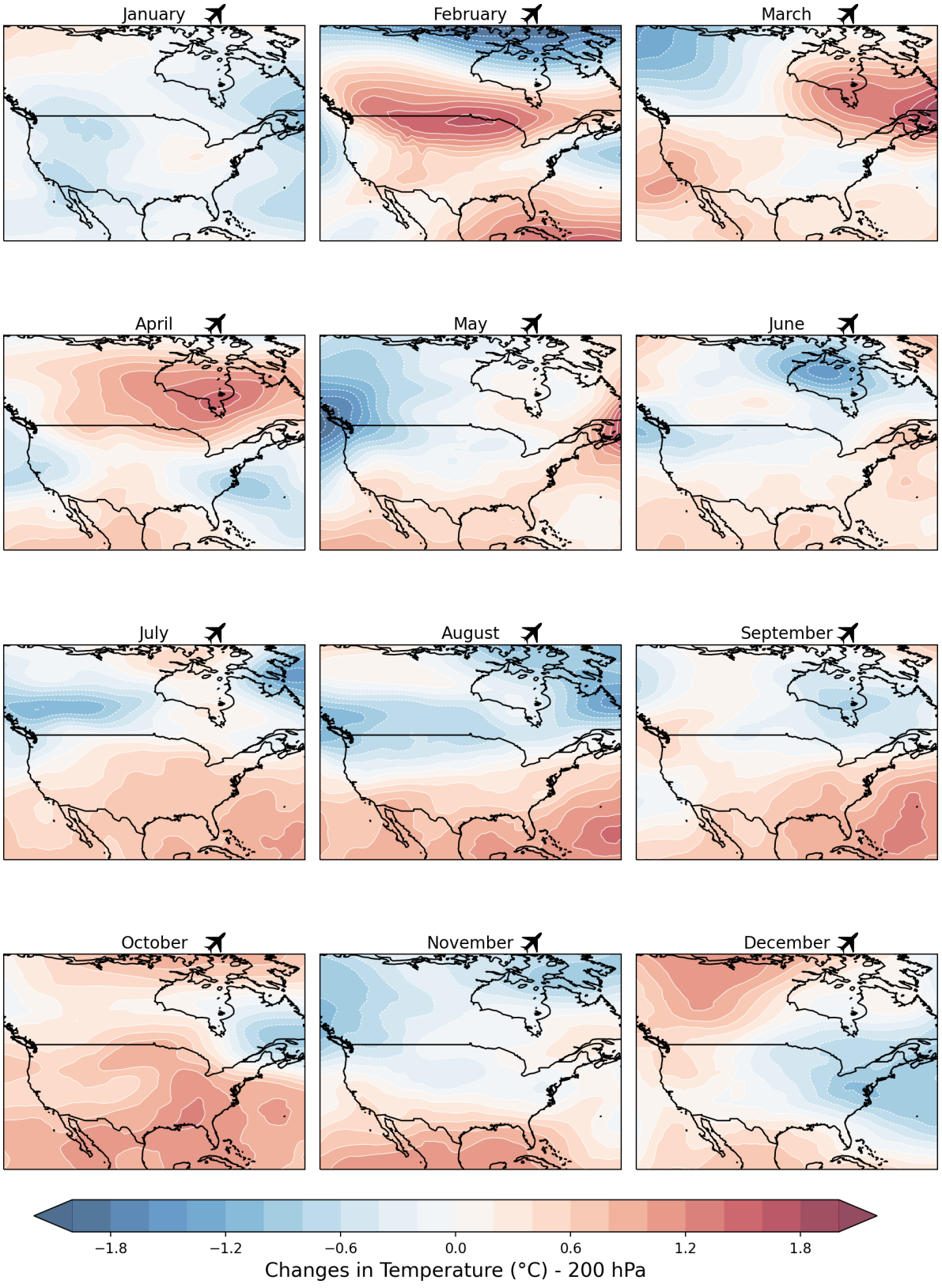

FIGURE 4.23: Mean changes of the temperature at 200 hPa for the last decade (2014-2023). Showing seasonal deviations across CONUS for each month were positive values (red) represent warmer temperatures, while negative values indicate colder temperatures.

4.3.5 Changes in PV

Figures 4.24 and 4.25 show changes in PV anomalies between 250 hPa and 200 hPa in the last decade. The areas shaded between orange and red indicate positive PV anomalies. The areas shaded between blue and purple indicate negative PV anomalies.

During the peak of winter, specifically February, positive PV anomaly is concentrated across the Northern U.S and Canada. Negative PV anomalies are extending from the Atlantic to the Northeast and Southeast of the U.S. This gradient in PV anomalies will result in enhanced wind speeds (Figs. 4.14 and 4.15) across northern latitudes. This configuration of positive PV anomalies on the poleward side of the jet stream and negative PV anomalies on its equatorward side will enhance jet streaks Bishop and Thorpe (1994). The regions of negative PV anomalies and strong VWS (Fig. 4.16) will enhance CAT risk. This is consistent with CAT PIREPs climatology over the last 20 years (Fig. 4.1), especially across the Northeast and Midwest.

From June to August, the gradient of PV anomalies is reverse, where negative PV anomalies are on the poleward side and the positive PV anomalies are on the equatorward side of the mean westerlies that define the mean position of the jet stream (Figs. 4.2 and 4.3). This is indicative of the weakening of the jet stream during summer.

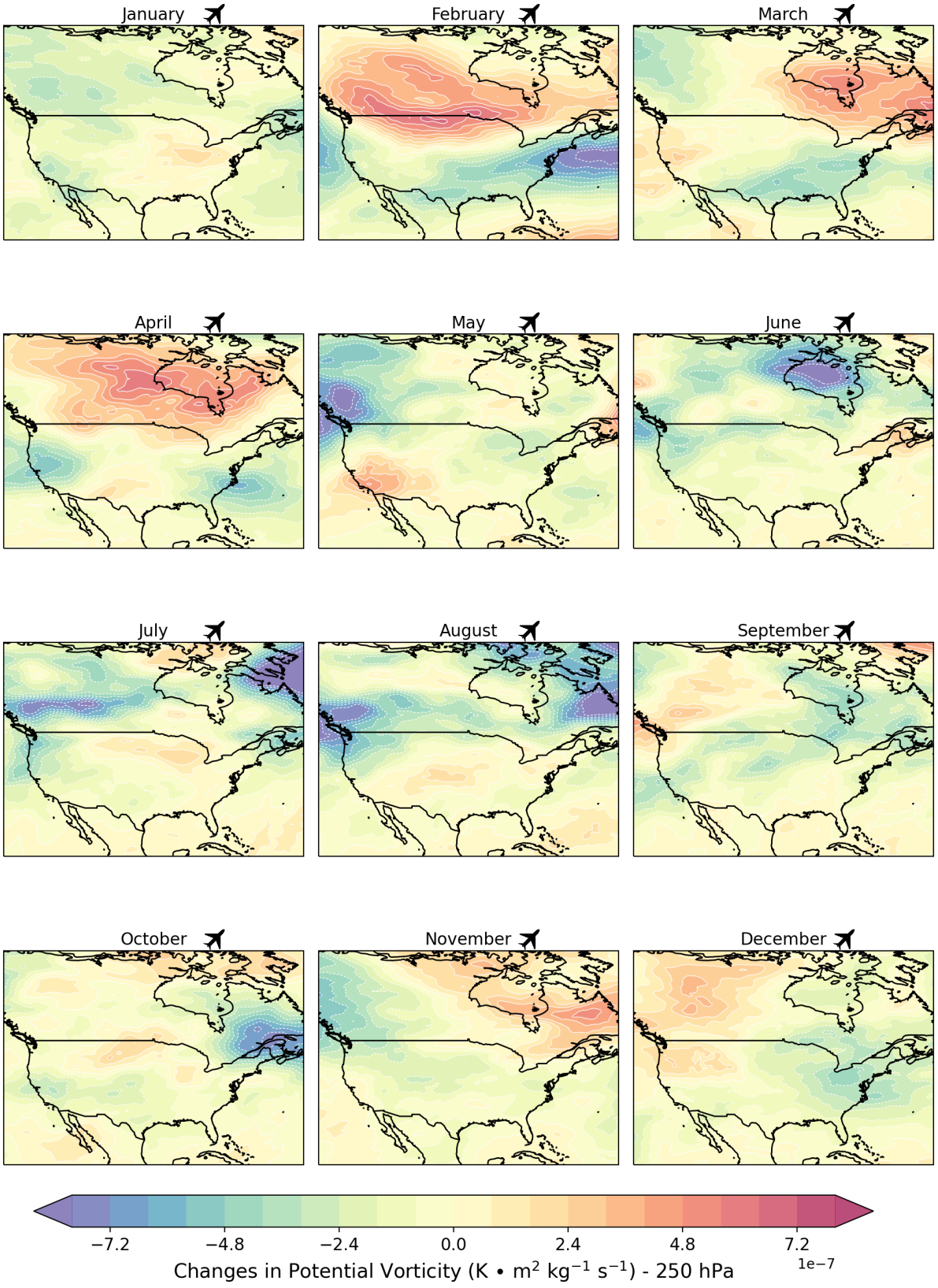

FIGURE 4.24: Changes in mean PV between the comparison period (2014-2023) and the reference period (1980-2013) at 250 hPa. Positive values (orange to red) indicate an increase in PV, while negative values (blue to purple) indicate a decrease in PV for each calendar month.

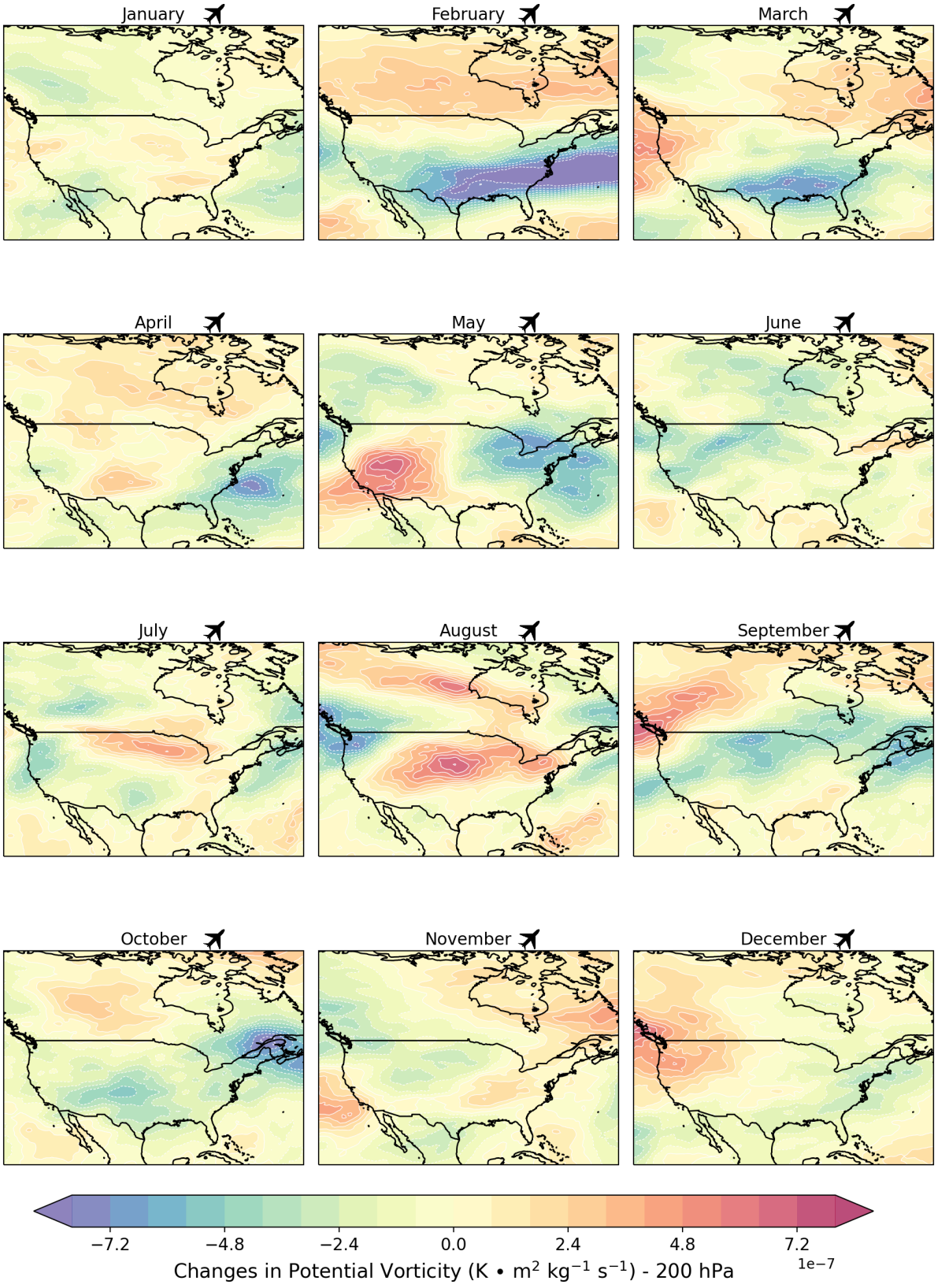

FIGURE 4.25: Changes in mean PV between the comparison period (2014-2023) and the reference period (1980-2013) at 200 hPa. Positive values (orange to red) indicate an increase in PV, while negative values (blue to purple) indicate a decrease in PV for each calendar month.

4.3.6 Changes in Specific Humidity

Figures 4.26 and 4.27 show the seasonal changes of specific humidity for the last decade across CONUS. For each calendar month, moisture has increased in the U.S. over the last decade. Water vapor is considered a greenhouse gas that traps heat in the atmosphere. Additionally, higher levels of moisture form cirrus clouds, which further retain regional warming (Figs. 4.22 and 4.23) at critical flight levels. This relationship is consistent with the Clausius-Clapeyron equation, which suggests that warmer air can hold more moisture. However, for February, March, and April, there are lower values of moisture associated with intrusions of stratospheric dry air over Canada. These intrusions of stratospheric air lead to increases in PV (Figs. 4.24 and 4.25), which in turn strengthen the jet streak for February over the Northeast of U.S.

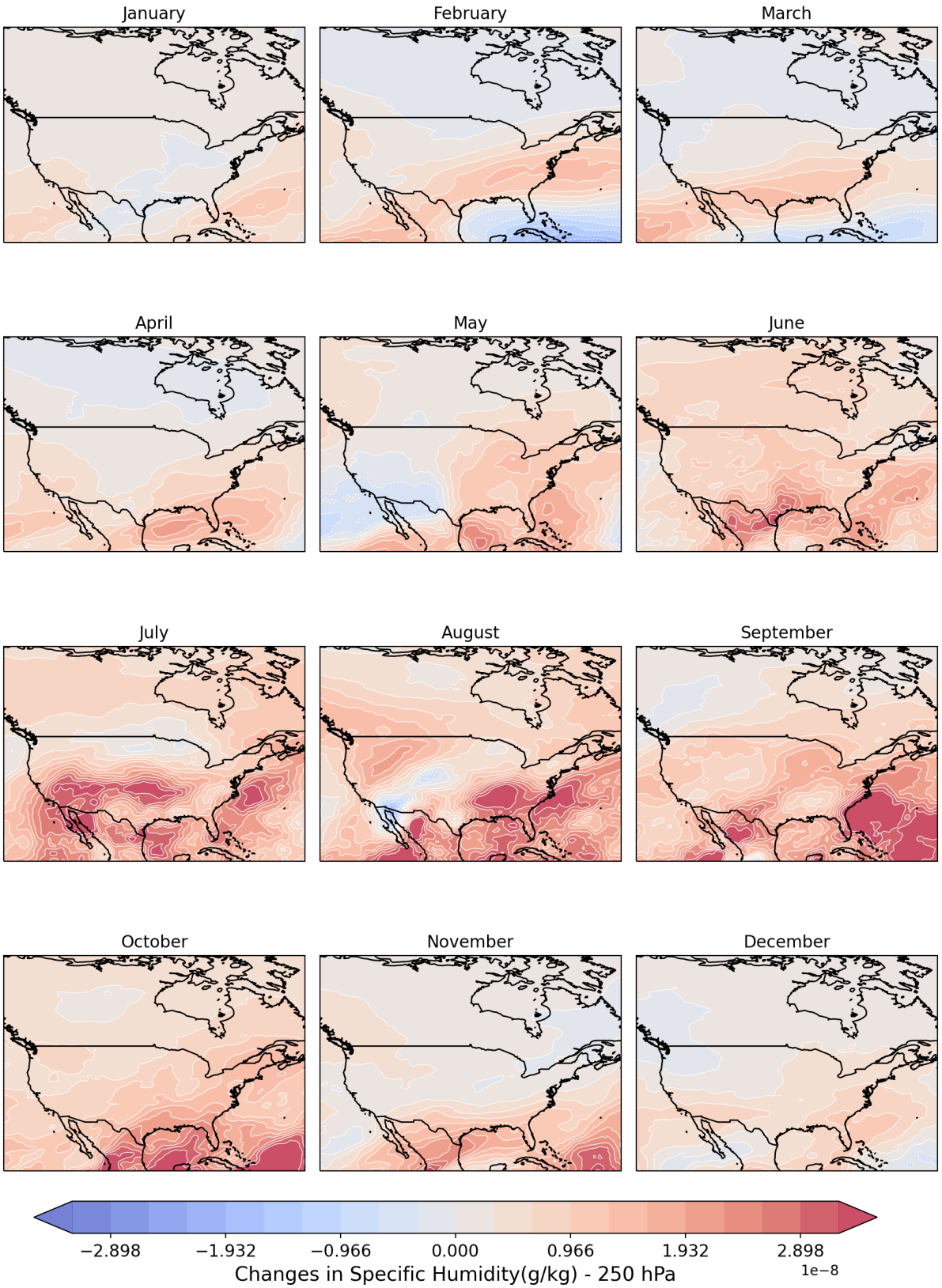

FIGURE 4.26: Changes in mean Specific Humidity (q) between the comparison period (2014-2023) and the reference period (1980-2013) at 250 hPa. Positive values (red) indicate increased moisture, while negative values (blue) indicate decreased moisture for each calendar month.

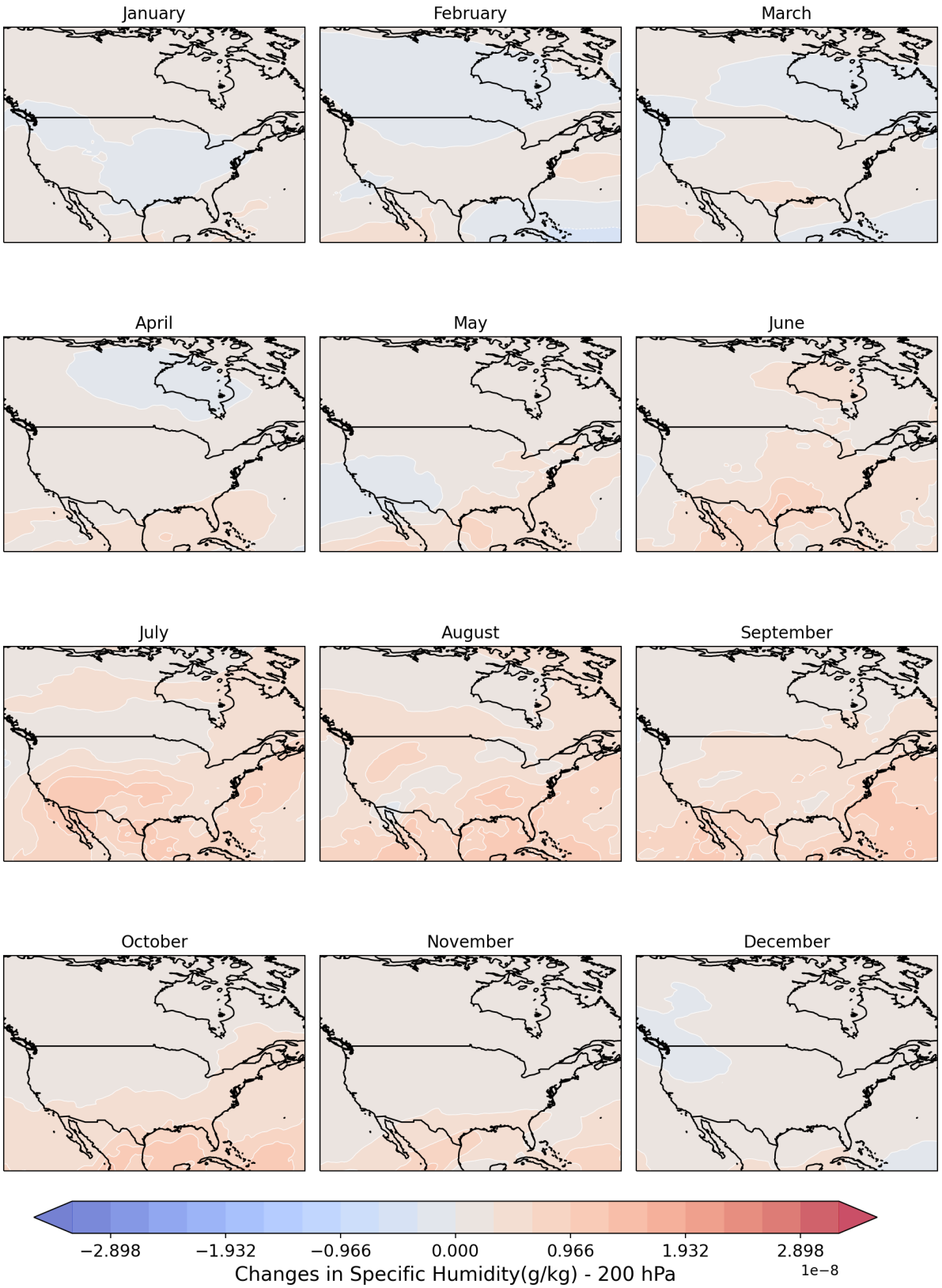

FIGURE 4.27: Changes in mean Specific Humidity (q) between the comparison period (2014-2023) and the reference period (1980-2013) at 200 hPa. Positive values (red) indicate increased moisture, while negative values (blue) indicate decreased moisture for each calendar month.

Chapter 5

Discussion

5.1 Environmental Trends driving increases in CAT

5.1.1 Horizontal Wind Speed, VWS, EDR and PV anomalies

The jet stream has undergone some changes over the past decade (2014-2023) relative to the last three decades due to changes in atmospheric variables. Particularly in winter, where wind speeds in the Northern U.S and Southern Canada have increased, while wind speeds have decreased along the South of U.S or the subtropics. These changes suggest a poleward shift of the jet stream (Figs. A.1 and A.2) during February, increasing turbulence risk areas at higher latitudes. These findings are consistent with CAT occurrence near jet streams (e.g., Lester (1994)). For instance, the 20-year climatology of PIREPs

(Fig. 4.1) demonstrates the occurrence of CAT in the vicinity of jet streams. More specifically, on the cyclonic side, above and below the jet stream core (Figs. 4.2 and 4.3). In fact, from February to April, these regions coincide with strong PV gradients, which are associated with the jet stream and contribute to the occurrence of CAT.

Changes in the jet stream are related to more frequent CAT in North America (Fig. 4.1). More specifically, regions with strong changes in wind speed (Figs. 4.14 and 4.15) can lead to an increase in VWS (Fig. 4.16) and reduced stability, which is typically where CAT occurs. Previous research have indicated that increases in VWS within the jet stream (e.g., Williams and Joshi (2013) and Lee et al. (2019)), especially during winter, however, these studies have not resolved the temporal resolution at a monthly scale. In contrast, the results presented in this work identify February as the month of peak intensification of the VWS.

5.1.2 Warming at upper levels

Upper-level temperatures had some implications in the dynamics of the jet streams in the last decade. For instance, upper-level warming (Fig. 4.8) is exceeding 1.5°C between the Subtropics and the Mid-latitude, strengthening the meridional temperature gradient. Hence, the horizontal upper-level winds must increase with height according to the thermal wind relationship. This is consistent with previous studies where climate change is increasing temperature gradients (Figs. 4.22 and 4.23) and VWS (Fig. 4.16) at upper levels (e.g., Lorenz and DeWeaver (2007), Change (2007), Delcambre et al. (2013), Xiang et al. (2014), Williams and Joshi (2016)).

5.2 CAT Hotspots and Mechanisms

In the last decade, PIREPs showed that CAT was found in the South, East, and Midwest of the U.S. However, CAT hotspots are only seen over the Northeast and Midwest. From December to April, changes in the regions of $|\omega|$ are increasing in the Northeast and coincide with the mean CAT climatological PIREPs. Trends in ω (Figs. 4.6 and 4.7) can be used to confirm the mechanism of CAT over the region. For instance, the positive ω will result in Mid-latitude weather systems between December and April. More specifically, the updrafts and downdrafts from these low-pressure systems cause CAT. This is reflected in PIREPs (Fig. 4.1), which show increased CAT reports in regions experiencing stronger vertical motions, confirming the operational impact of these turbulence-relevant parameters. Furthermore, EDR trends confirm the increase in turbulent-prone zones over localized areas between December and April.

However, a strong gradient between the ascent and descent movements in the North of Mexico and in the Rockies will increase the potential for mountain waves. This is consistent with PIREPs, which show increased CAT reports in regions experiencing stronger vertical motions (Figs. 4.18 and 4.19). These changing patterns demand more precise forecasting, as turbulence may now emerge in areas traditionally considered low-risk, complicating flight planning.

5.3 Implications for Commercial Airlines

The results of this analysis indicate that favorable atmospheric conditions for CAT are becoming more prevalent, particularly along major airline routes. Increases in VWS, EDR, mean $|\omega|$, strong temperature gradients, PV gradients, and moisture gradients in regional hotspots such as the Northeast and Midwest are dynamically associated with the occurrence of CAT.

CAT can lead to increased fuel consumption and delays as pilots are forced to circumvent affected areas, further affecting the efficiency of flight operations. Specifically, the poleward shift of the jet stream in February is increasing turbulence encountered at higher latitudes. Airlines must modify cruising altitudes and routes to reduce turbulence encounters and improve fuel efficiency. This study is important because the integration of reanalysis data and PIREPs will be critical for turbulence forecasting tools to provide accurate alternative routes and maintain passenger safety and comfort.

5.4 Turbulence Composite Risk

In Oyola and Rodriguez-Nazario (2025) a climatological composite of risk upper-level turbulence over CONUS was constructed using a principal component approach. Additionally, monthly mean MERRA-2 reanalysis data, such as $|\omega|$, wind speed, temperature gradients, and EDR were spatially standardized and interpolated to a common grid. The monthly mean MERRA-2 was aggregated across the UTLS flight levels between FL180 ($\sim$ 500 hPa) and FL450 ($\sim$ 150 hPa) from 2001 to 2024. At each flight level, the four indices

were stacked and subjected to principal component analysis (PCA), with the first principal component (PC1) retained to represent the dominant spatial structure of turbulent environments. The relative contribution of each atmospheric variable to PC1 was used to weight the standardized inputs and generate a composite risk for each atmospheric level. These atmospheric levels composites were vertically integrated to produce a risk map of turbulence (Fig. 5.1). For qualitative validation, the PIREPs were interpolated and overlaid.

Over the 2001 and 2024 period, composite values are high in the Northeastern of the U.S., particularly near New York (JFK) and Boston (BOS) airports where upper-level jet streaks and VWS are frequent and present. Regions near Denver (DEN), Southern California (LAX) airports, and areas of the Central U.S. showed moderate composite turbulence risk. Lower composite risk is observed over the Gulf Coast, Southwest of the U.S., and the Pacific Northwest. These patterns in upper-level turbulence coincide with PIREPs (Fig. 5.1, white contours), which highlight frequent reporting corridors. It is important to mention, that this analysis does not incorporate flight levels below FL180, turbulence associated with mountain waves and other terrain-induced processes may be underrepresented. This limitation is currently being addressed in ongoing work and is discussed further in the upcoming companion publication.

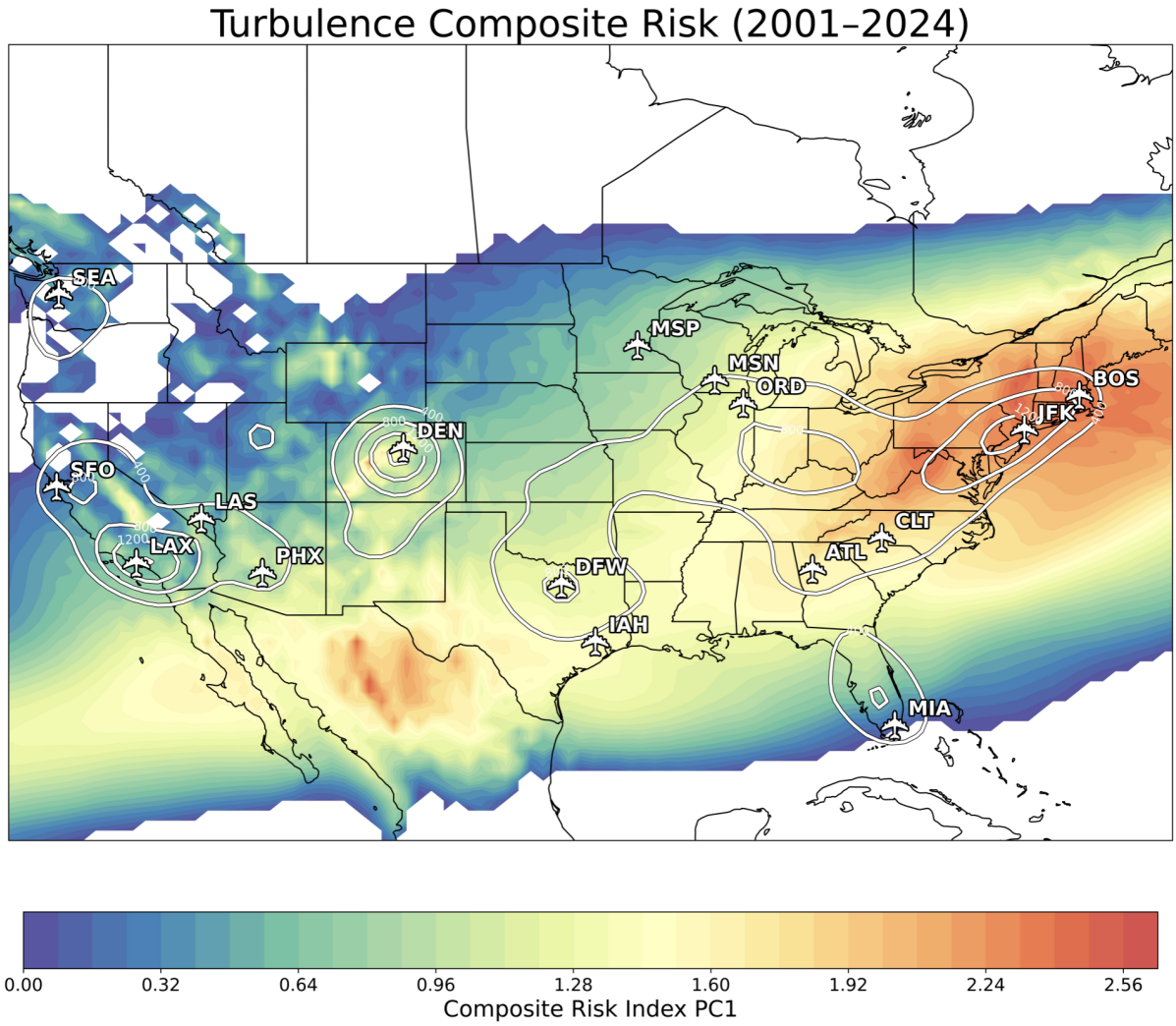

FIGURE 5.1: Composite turbulence risk index (PC1) for the 2001–2024 period, derived from reanalysis data: $|\omega|$, wind speed, temperature gradients, and EDR between FL180 ($\sim$ 500 hPa) and FL450 ($\sim$ 150 hPa). The red-orange colors indicate higher composite turbulence risk. Overlaid white contours represent spatially interpolated frequencies of PIREPs, highlighting observed areas of persistent turbulence activity (Oyola and Rodriguez-Nazario (2025)).

Chapter 6

Conclusion and Future Work

6.1 Addressing Research Questions

This study aimed to understand how long-term deviations in atmospheric conditions have changed, with a particular focus on the jet stream. Previous research has linked CAT occurrences to large-scale jet stream dynamics, where abrupt shifts in wind speed often enhance wind shear within the jet. Using MERRA-2 reanalysis data, this work examined changes in the jet stream at critical flight levels between 250 hPa and 200 hPa. These pressure levels correspond only to standard atmospheric variables. However, VWS and EDR were examined at pressure levels from 700 hPa to 250 hPa. This work evaluated changes in these variables over a 43-year period, with a specific focus on deviations from climatological norms in the last decade (2014-2023). Despite the coarse resolution of MERRA-2, atmospheric mechanisms that contributed to the occurrence of CAT were

identified. In addition, operational PIREPs were implemented to validate the robustness of the turbulence analysis and to identify regional CAT hotspots at flight levels above FL150 (∼570 hPa) over 20 years (2003-2023). Therefore, three primary research questions were explored. This section highlights each research question and summarizes key findings.

1. How have the turbulence parameters associated with the jet stream evolved over the past decade?

   Wind Speed and VWS: The jet stream has shifted poleward, with increased zonal wind speeds and enhanced VWS near the jet core during February and November. This shift in the jet may increase turbulence risks at higher altitudes (250 hPa or FL340), where stronger wind shear gradients are likely to develop. Additionally, increases in VWS contribute to more frequent and severe CAT conditions. During February, the encounter with turbulence may lead to increased fuel consumption in commercial aircraft due to adjustments to changes in altitude and flight paths across the northern regions of U.S. and southern Canada. While decreased VWS reduces turbulence risk in the subtropics. For November, the flight path that may increase fuel consumption is over the east-northeast, south of the U.S. and northern Mexico.

   EDR: Regions of increased EDR coincide with regions of increased VWS. EDR has increased in the U.S. and Canada, indicating an increase in turbulence intensity between February and March. While turbulence intensity has decreased along

the subtropics. For May, turbulence intensity increases in the northeast of U.S., southeast of Canada, and the mountain region of the northwest of Mexico. For June, turbulence intensity has increased over the Rockies and Midwest. While, turbulence intensity has decreased in southern Canada and northern U.S. during summer. For November, EDR has increased in the east-northeast, south of the U.S., and northern Mexico, coinciding with VWS changes. These patterns strengthen the existing seasonal turbulence risk and emphasize the requirement for sudden changes in the flightpath of a commercial aircraft to ensure passenger safety.

ω: Increases in $|\omega|$ over the Northeast and Midwest resulted in stronger upward motion associated with midlatitude weather systems during winter. The ascent and descent from these low-pressure systems can generate CAT. This strengthened vertical motions near the jet core align with areas of heightened turbulence, reinforcing the role of VWS in CAT formation.

T: Upper-level warming exceeding 1.5 °C has changed the meridional temperature gradient, contributing to seasonal changes in the position of the jet stream. During February and November, the temperature gradient strengthens and shifts northward, contributing to baroclinic instability and increasing the horizontal wind speeds of the jet stream.

q and PV: Moisture has increased at upper-levels trapping more heat, contributing to warmer temperatures and more frequent CAT due to sharper moisture gradients. Lower moisture over Canada is consistent with with stratospheric

air intrusions highlighted by regional positive PV anomalies during February. While, negative PV anomalies below the jet core is consistent with tropospheric air intrusions. This gradients in PV anomalies contributes to more frequent CAT over the northeast of U.S. for February.

2. What are the regional hotspots for CAT over CONUS, and what atmospheric trends contribute to its occurrence?

   Regional Hotspots: Identified 20-year-PIREPs climatology of regional CAT hotspots over CONUS. Regional hotspots in the Northeast, Midwest, and South of the U.S., emphasize the regions of increased aviation risk and the need to improve model resolutions.

   Atmospheric trends: Regions of strong shear, EDR, vertical motions of the air, temperature gradients, moisture gradients, and PV gradient anomalies.

3. How well do MERRA-2 reanalysis data and PIREPs represent turbulence-relevant parameters over CONUS, and what factors contribute to their subjectivity?

   Despite the coarse resolution of MERRA-2 reanalysis and the reporting frequency and quality of PIREPs, both represented the turbulence-relevant parameters over CONUS. For instance, the position of the jet stream aligns with the climatology of CAT PIREPs over the Northeast of the U.S. Particularly, regions of $|\omega|$ coincide with CAT PIREPs over the Northeast and Midwest during winter. Trends in ω indicated the mechanism of CAT, which corresponds to the updraft and downdraft of low-pressure systems. EDR trends supported

the increased turbulence over the Northeast, Midwest, and South of the U.S. Additionally, PV anomalies coincided with VWS and EDR regions over turbulent regions. Is important to mention that there is a decrease in the volume of PIREPs for several reasons. Pilots tend to avoid turbulent conditions, making the verification of the forecast difficult (Sharman (2016)). Occasionally, pilots of commercial aircraft only provide the PIREPs to their own company's carriers, making some of these reports not included in the actual PIREPs archive (Casner (2010)). A recommendation, suggested by Casner (2010), to increase the volume of PIREPs with weather information is to improve the pilot's understanding and identification of the different weather phenomena.

6.2 Current Work

As described in Chapter 2, there are several forecasting and reporting methods for CAT. However, there is a great need to understand, detect, and forecast CAT to improve passenger safety and comfort. Currently, ongoing work is being done based on the results obtained in this thesis. For instance, the Model for Prediction Across Scales (MPAS) is being used to capture localized turbulence events, such as those associated with jet stream instabilities and mountain wave interactions, while maintaining a global atmospheric context. In Chapter 4, PIREP identified regional hotspots for CAT in the Northeast and Midwest. Hence, using PIREPs for a specific CAT case, particularly from one of the regional hotspots, can be useful to validate model output. For future work, it will

consider determining the factors that might be driving the dynamic turbulence in the Northeast of the U.S., such as shear vorticity or curvature vorticity, in February.

Another ongoing work is using machine learning (ML) techniques, such as feature selection, Convolutional Neural Network (CNN), LongShort-Term Memory (LSTM), and more to integrate turbulence predictors from MERRA-2 reanalysis data, such as ω, wind speed, and EDR. By using these ML techniques, future work will correctly weight these aviation parameters to identify high-resolution turbulence risk areas in the U.S. Additionally, risk maps can be validated with PIREPs and EDR calculations.

Collaboration between researchers, operational meteorologists, and pilots is needed to improve the understanding, detection, and forecasting of CAT. Hence, risk maps will be shared with operational meteorologists, airlines, and aviation stakeholders. Another way to increase collaboration between the different disciplines is by sharing turbulence products from model data or ML for performance comparison with operational turbulence forecasts. In addition, interview pilots about the specific needs in their turbulence products. From a personal perspective, participate in outreach activities and major conferences to connect and share with aviation stakeholders and the general community. Participate in future EAA AirVenture Oshkosh to talk about the basics of turbulence and to create awareness of the severity of encountering turbulence when passengers are not wearing a seatbelt. Create an online workshop for aviation enthusiasts to talk about the different types of turbulence and the areas of risk that you may encounter severe turbulence. In doing so, we are getting a step closer to collaborate with pilots, researchers,

and operational meteorologists to ensure passenger safety and comfort.

Appendix A

Climatology of the last decade (2014 - 2023)

Figures A.1 and A.2 represent the climatology of horizontal upper-level wind speeds (200 hPa and 250 hPa) in the last decade.

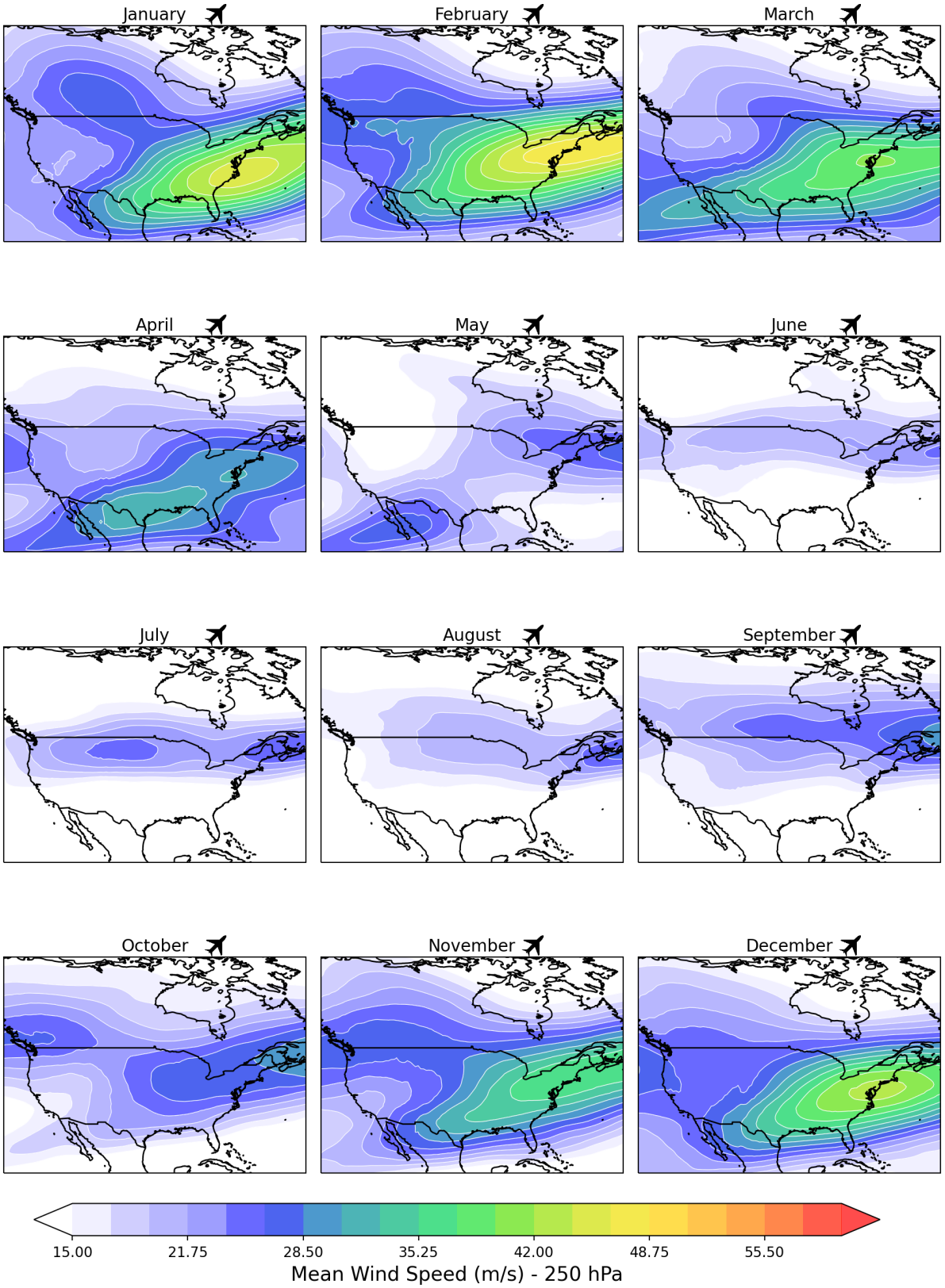

FIGURE A.1: Mean climatology of the jet stream at 250 hPa from 2014 to 2023. Showing the seasonal changes in wind speed across CONUS for each month. Most importantly, highlighting the poleward shift of the jet stream during February.

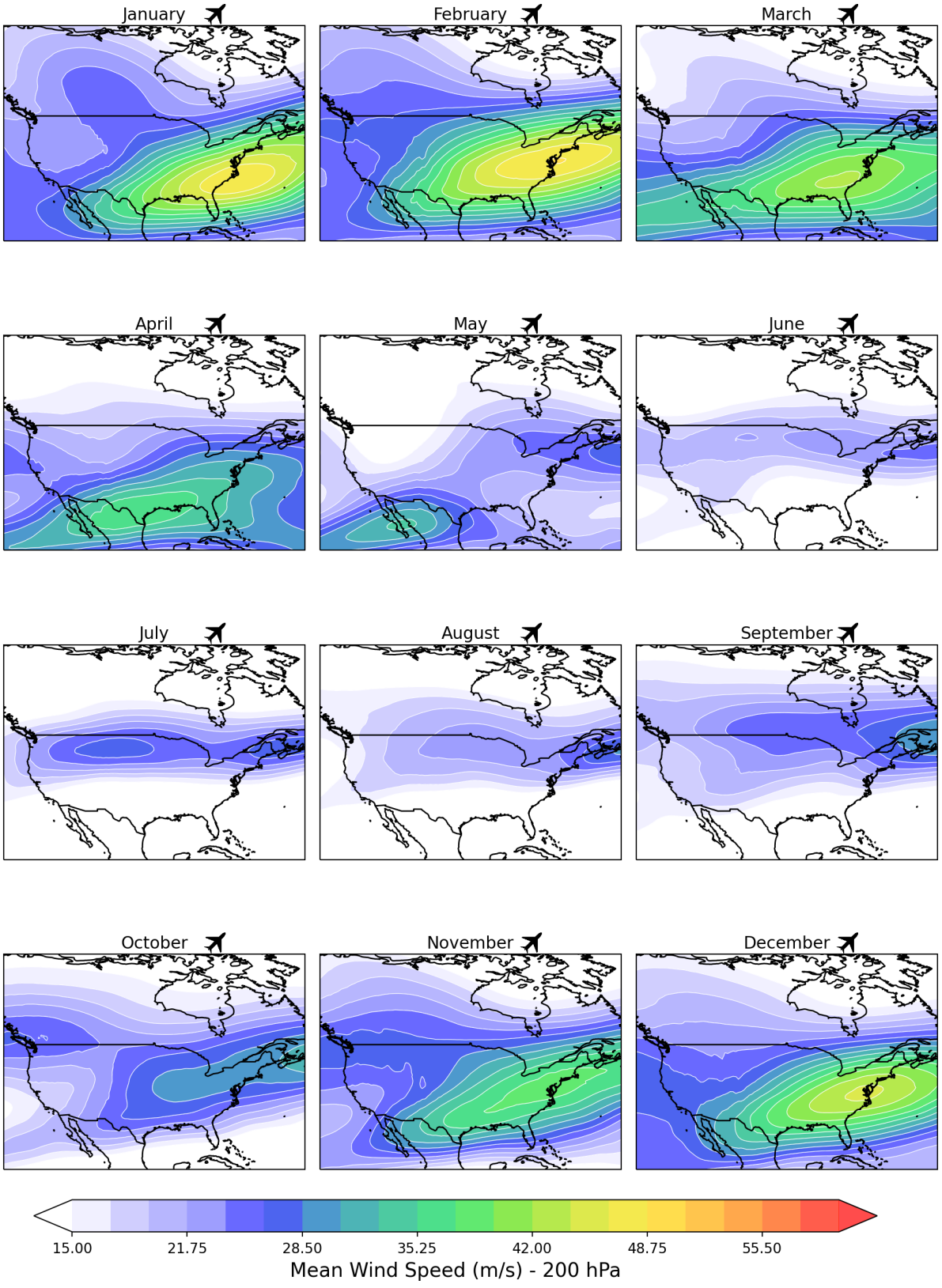

FIGURE A.2: Mean climatology of the jet stream at 200 hPa from 2014 to 2023. Showing the seasonal changes in wind speed across CONUS for each month. Most importantly, highlighting the poleward shift of the jet stream during February.

Bibliography

Akritidis, D., A. Pozzer, J. Flemming, A. Inness, and P. Zanis, 2021: A global climatology of tropopause folds in cams and merra-2 reanalyses. *Journal of Geophysical Research: Atmospheres*, **126**, e2020JD034115.

Bannon, J., 1951: *Weather systems associated with some occasions of severe turbulence at high altitude*. Air Ministry.

Bechtold, B. M. D. A. L. M. . I. L., P., 2021: Forecasting clear-air turbulence. *EDMWF Newsletter*, **168**.

URL `https://www.ecmwf.int/en/newsletter/168/meteorology/forecasting-clear-air-turbulence`

Belmecheri, S., F. Babst, A. R. Hudson, J. Betancourt, and V. Trouet, 2017: Northern hemisphere jet stream position indices as diagnostic tools for climate and ecosystem dynamics. *Earth Interactions*, **21**, 1–23.

Bishop, C. H. and A. J. Thorpe, 1994: Potential vorticity and the electrostatics analogy: Quasi-geostrophic theory. *Quarterly Journal of the Royal Meteorological Society*, **120**,

713–731.

Casner, S. M., 2010: Why don't pilots submit more pilot weather reports (pireps)? *The International Journal of Aviation Psychology*, **20**, 347–374.

Castorrini, A., S. Gentile, E. Geraldi, and A. Bonfiglioli, 2021: Increasing spatial resolution of wind resource prediction using NWP and RANS simulation. *Journal of Wind Engineering and Industrial Aerodynamics*, **210**, 104499, doi:10.1016/j.jweia.2020.104499.

URL `https://linkinghub.elsevier.com/retrieve/pii/S0167610520304098`

Change, I. P. O. C., 2007: Climate change 2007: The physical science basis. *Agenda*, **6**, 333.

Chen, S.-H., 2014: Jet stream. Lecture14$_{J}et_{S}tream$.

URL

Delcambre, S. C., D. J. Lorenz, D. J. Vimont, and J. E. Martin, 2013: Diagnosing northern hemisphere jet portrayal in 17 cmip3 global climate models: Twenty-first-century projections. *Journal of Climate*, **26**, 4930–4946.

Dutton, J. A. and H. A. Panofsky, 1970: Clear air turbulence: A mystery may be unfolding: High altitude turbulence poses serious problems for aviation and atmospheric science. *Science*, **167**, 937–944.

Ellrod, G. P., 1989: A decision tree approach to clear air turbulence analysis using satellite and upper air data.

https://repository.library.noaa.gov/view/noaa/19299

— 2003: *Clear Air Turbulence*. 393–403 pp.

http://dx.doi.org/10.1016/B0-12-227090-8/00104-4

Ellrod, G. P. and D. I. Knapp, 1992: An Objective Clear-Air Turbulence Forecasting Technique: Verification and Operational Use. *Weather and Forecasting*, **7**, 150–165, doi:10.1175/1520-0434(1992)007<0150:AOCATF>2.0.CO;2.

http://journals.ametsoc.org/doi/10.1175/1520-0434(1992)007<0150:AOCATF>2.0.CO;2

Ellrod, G. P. and J. A. Knox, 2010: Improvements to an Operational Clear-Air Turbulence Diagnostic Index by Addition of a Divergence Trend Term. *Weather and Forecasting*, **25**, 789–798, doi:10.1175/2009WAF2222290.1.

https://journals.ametsoc.org/doi/10.1175/2009WAF2222290.1

Endlich, R. M., 1964: The Mesoscale Structure of Some Regions of Clear-Air Turbulence. *Journal of Applied Meteorology (1962-1982)*, **3**, 261–276, publisher: American Meteorological Society.

http://www.jstor.org/stable/26169412

FAA, 1968: Clear air turbulence avoidance a bibliography.

https://www.fire.tc.faa.gov/pdf/na68-17.pdf

— 2016: Clear air turbulence avoidance.

https://www.faa.gov/documentlibrary/media/advisory_circular/ac_00-30c.pdf

— 2017: Faasteam notice.

https://www.faasafety.gov/spans/noticeView.aspx?nid=7155

Gelaro, R., W. McCarty, M. J. Suárez, R. Todling, A. Molod, L. Takacs, C. A. Randles, A. Darmenov, M. G. Bosilovich, R. Reichle, K. Wargan, L. Coy, R. Cullather, C. Draper, S. Akella, V. Buchard, A. Conaty, A. M. Da Silva, W. Gu, G.-K. Kim, R. Koster, R. Lucchesi, D. Merkova, J. E. Nielsen, G. Partyka, S. Pawson, W. Putman, M. Rienecker, S. D. Schubert, M. Sienkiewicz, and B. Zhao, 2017: The Modern-Era Retrospective Analysis for Research and Applications, Version 2 (MERRA-2). *Journal of Climate*, **30**, 5419–5454, doi:10.1175/JCLI-D-16-0758.1.

https://journals.ametsoc.org/doi/10.1175/JCLI-D-16-0758.1

Georgiev, C. G., P. Santurette, and K. Maynard, 2016: Potential vorticity thinking. *Weather Analysis and Forecasting*, C. G. Georgiev, P. Santurette, and K. Maynard, eds., Academic Press, Boston, 2nd edition, 3–19.

https://www.sciencedirect.com/science/article/pii/B9780128001943000017

Gálvez, J., 2023: Turbulence and Icing.

https://www.icao.int/NACC/Documents/Meetings/2023/SIGMET/06%20Turbulence%20and%20Icing.pdf

Hord, C., 2018: Proposed revision to eddy dissipation rate (edr) values in annex 3.

https://www.icao.int/airnavigation/METP/Seventh%20Meeting%20of%20the%20MOG/METPWGMOG-7_Attachment_SN_35_METP_4_WP.xxxx.Revised_EDR_values_Amd_79_vs_1.0_22mar2018.docx

ICAO, 2023: Turbulence and icing.

https://www.icao.int/NACC/Documents/Meetings/2023/SIGMET/06%20Turbulence%20and%20Icing.pdf

Kim, J.-H., W. N. Chan, B. Sridhar, and R. D. Sharman, 2015: Combined winds and turbulence prediction system for automated air-traffic management applications. *Journal of Applied Meteorology and Climatology*, **54**, 766–784.

https://doi.org/10.1175/JAMC-D-14-0216.1

Kim, J.-H., H.-Y. Chun, R. D. Sharman, and T. L. Keller, 2011: Evaluations of upper-level turbulence diagnostics performance using the graphical turbulence guidance (gtg) system and pilot reports (pireps) over east asia. *Journal of applied meteorology and climatology*, **50**, 1936–1951.

https://doi.org/10.1175/JAMC-D-10-05017.1

Kim, J.-H., R. D. Sharman, S. G. Benjamin, J. M. Brown, S.-H. Park, and J. B. Klemp, 2019: Improvement of Mountain-Wave Turbulence Forecasts in NOAA's Rapid Refresh (RAP) Model with the Hybrid Vertical Coordinate System. *Weather and Forecasting*, **34**, 773–780, doi:10.1175/WAF-D-18-0187.1.

https://journals.ametsoc.org/doi/10.1175/WAF-D-18-0187.1

Knox, J. A., 1997: Possible Mechanisms of Clear-Air Turbulence in Strongly Anticyclonic Flows. *Monthly Weather Review*, **125**, 1251–1259, doi:10.1175/1520-0493(1997)125<1251:PMOCAT>2

http://journals.ametsoc.org/doi/10.1175/1520-0493(1997)125<1251:PMOCAT>2.0.CO;2

Ko, H.-C., H.-Y. Chun, M. A. Geller, and B. Ingleby, 2024: Global Distributions of Atmospheric Turbulence Estimated Using Operational High Vertical-Resolution Radiosonde Data. *Bulletin of the American Meteorological Society*, **105**, E2551–E2566, doi:10.1175/BAMS-D-23-0193.1.

https://journals.ametsoc.org/view/journals/bams/105/12/BAMS-D-23-0193.1.xml

Koch, S. E., B. D. Jamison, C. Lu, T. L. Smith, E. I. Tollerud, C. Girz, N. Wang, T. P. Lane, M. A. Shapiro, D. D. Parrish, et al., 2005: Turbulence and gravity waves within an upper-level front. *Journal of the atmospheric sciences*, **62**, 3885–3908.

Lane, T. P., J. D. Doyle, R. Plougonven, M. A. Shapiro, and R. D. Sharman, 2004: Observations and numerical simulations of inertia–gravity waves and shearing instabilities

in the vicinity of a jet stream. *Journal of the atmospheric sciences*, **61**, 2692–2706.

Lee, D.-B. and H.-Y. Chun, 2018: A numerical study of aviation turbulence encountered on 13 february 2013 over the yellow sea between china and the korean peninsula. *Journal of Applied Meteorology and Climatology*, **57**, 1043–1060.
https://doi.org/10.1175/JAMC-D-17-0247.1

Lee, S. H., P. D. Williams, and T. H. Frame, 2019: Increased shear in the north atlantic upper-level jet stream over the past four decades. *Nature*, **572**, 639–642.
https://doi.org/10.1038/s41586-019-1465-z

Lester, P. F., 1994: *Turbulence: a new perspective for pilots*. Jeppesen Sanderson Training Systems, Englewood, CO, oCLC: 33979606.

Lorenz, D. J. and E. T. DeWeaver, 2007: Tropopause height and zonal wind response to global warming in the ipcc scenario integrations. *Journal of Geophysical Research: Atmospheres*, **112**.

Machta, L., 1955: Turbulence in clear air and its relation to the jet stream. *Journal of Meteorology*, **12**, 329–341, doi:10.1175/JAS-D-04-0123.1.

Martin, J. E., 2006: *Applications of the Equations of Motion*. John Wiley & Sons.

McCann, D. W., J. A. Knox, and P. D. Williams, 2012: An improvement in clear-air turbulence forecasting based on spontaneous imbalance theory: the ulturb algorithm.

Meteorological Applications, **19**, 71–78.

https://doi.org/10.1002/met.260

McCann, Donald W, 2001: Gravity waves, unbalanced flow, and aircraft clear air turbulence. *National Weather Digest*, **25**, 3–14.

https://www.researchgate.net/profile/Donald-Mccann-2/publication/266499495_GRAVITY_WAVES_UNBALANCED_FLOW_AND_AIRCRAFT_CLEAR_AIR_TURBULENCE/links/552599cd0cf295bGRAVITY-WAVES-UNBALANCED-FLOW-AND-AIRCRAFT-CLEAR-AIR-TURBULENCE.pdf

Mélanie, G.-D., D. Georges, R. Emmanuel, and A. Nadir, 2021: Balloon-borne and airborne measurements. *Advances in Spectroscopic Monitoring of the Atmosphere*, Elsevier, 521–601.

https://doi.org/10.1016/B978-0-12-815014-6.00006-3

Mesonet, I. E., 2024: Archived Pilot Reports (PIREPs).

https://mesonet.agron.iastate.edu/request/gis/pireps.php

NOAA, 2021: Experimental goes turbulence product from cimss.

https://vlab.noaa.gov/web/towr-s/cimss-turbulence

NTSB, 2021: Preventing Turbulence-Related Injuries in Air Carrier Operations Conducted Under Title 14 Code of Federal Regulations Part 121. *Safety Research Report NTSB/SS-21/01*.

https://www.ntsb.gov/safety/safety-studies/Documents/SS2101.pdf

NTSB, 2023a: Accident report for delta air lines flight 175 turbulence incident. Technical Report DCA23MA165, National Transportation Safety Board, available online at https://data.ntsb.gov/carol-repgen/api/Aviation/ReportMain/GenerateNewestReport/192959/pdf.

— 2023b: Aviation incident final report: Envoy air flight 3788. Technical Report CHI23LA300, National Transportation Safety Board, available online at https://data.ntsb.gov/carol-repgen/api/Aviation/ReportMain/GenerateNewestReport/192864/pdf.

NTSB, 2024: Aviation investigation report: Delta flight 2763. Technical report, National Transportation Safety Board.
https://data.ntsb.gov/carol-repgen/api/Aviation/ReportMain/GenerateNewestReport/194029/pdf#:~:text=April%203rd%2C%202024%2C%20Delta%20flight,it%20on%20his%20previous%20flight.

Overeem, A., 2002: Verification of clear-air turbulence forecasts.
https://cdn.knmi.nl/knmi/pdf/bibliotheek/knmipubTR/TR244.pdf

Oyola, M. and I. Rodriguez-Nazario, 2025: The captain has turned on the seatbelt sign: A climatological analysis of convective and clear-air turbulence indicators for aviation over conus. *Weather and Climate Dynamics (WCD)*.

Schwartz, B., 1996: The quantitative use of pireps in developing aviation weather guidance products. *Weather and Forecasting*, **11**, 372–384.

Sharman, R., 2016: *Aviation Turbulence: Processes, Detection, Prediction*. Springer International Publishing AG, Cham.

Sharman, R., C. Tebaldi, G. Wiener, and J. Wolff, 2006: An integrated approach to mid-and upper-level turbulence forecasting. *Weather and forecasting*, **21**, 268–287. https://doi.org/10.1175/WAF924.1

Sharman, R., S. Trier, T. Lane, and J. Doyle, 2012: Sources and dynamics of turbulence in the upper troposphere and lower stratosphere: A review. *Geophysical Research Letters*, **39**.

Stendel, M., J. Francis, R. White, P. D. Williams, and T. Woollings, 2021: The jet stream and climate change. *Climate Change*, Elsevier, 327–357. https://linkinghub.elsevier.com/retrieve/pii/B9780128215753000153

Stull, R. B., 2017: *Jet Streams*. University of British Columbia. https://geo.libretexts.org/Bookshelves/Meteorology_and_Climate_Science/Practical_Meteorology_(Stull)/11%3A_General_Circulation/11.8%3A_Jet_Streams

Williams, P. D. and M. M. Joshi, 2013: Intensification of winter transatlantic aviation turbulence in response to climate change. *Nature Climate Change*, **3**, 644–648, doi:10.1038/nclimate1866. https://www.nature.com/articles/nclimate1866

— 2016: Clear-air turbulence in a changing climate. *Aviation Turbulence: processes, detection, prediction*, 465–480.

Wimmers, A. and W. Feltz, 2007: A prediction scheme for aircraft turbulence at tropopause folds using satellite imagery and EDR data.
https://www-cdn.eumetsat.int/files/2020-04/pdf_conf_p50_s3_21_wimmers_p.pdf

Winters, A. C., D. Keyser, and L. F. Bosart, 2020: Composite vertical-motion patterns near north american polar–subtropical jet superposition events. *Monthly Weather Review*, **148**, 4565–4585.

Xiang, B., B. Wang, A. Lauer, J.-Y. Lee, and Q. Ding, 2014: Upper tropospheric warming intensifies sea surface warming. *Climate dynamics*, **43**, 259–270.